Integrated Spatiotemporal Characterization of Dust Sources and Outbreaks in Central and East Asia

A Thesis
Presented to
The Academic Faculty

by

Kremena T. Darmenova

In Partial Fulfillment
of the Requirements for the Degree
Doctor of Philosophy

School of Earth and Atmospheric Sciences
Georgia Institute of Technology
May 2006

Integrated Spatiotemporal Characterization of Dust Sources and Outbreaks in Central and East Asia

Approved by:

Professor Irina Sokolik, Advisor
School of Earth and Atmospheric Sciences
Georgia Institute of Technology

Professor Derek Cunnold
School of Earth and Atmospheric Sciences
Georgia Institute of Technology

Professor Judith Curry
School of Earth and Atmospheric Sciences
Georgia Institute of Technology

Dr. Irina Petropavlovskikh
NOAA/ESRL/GMD

Professor Robert Dickinson
School of Earth and Atmospheric Sciences
Georgia Institute of Technology

Date Approved: March 17, 2006

ACKNOWLEDGEMENTS

First, I would like to acknowledge Prof. Irina Sokolik for advising this thesis and mentoring me throughout my two years at the University of Colorado and three years at Georgia Tech. She deserves my deepest gratitude for her guidance, support and patience.

The majority of this work was based on simulations with the mesoscale model MM5. I would like to thank Ginger Caldwell for extending my NCAR project expiration twice making it possible to finish all runs on time. I am very grateful to all MM5 users whose helpful technical suggestions and ideas saved me many sleepless nights. I would like to thank the NCAR SCD's User Support Section for their prompt service and professionalism.

Many thanks to my friends and family. To my parents, I cherish your love and constant support. Thank you, for teaching me the discipline and diligence that helped me a lot during the years in Graduate school. To my husband Anton, thank you for all your help, fruitful discussions and understanding. I would like to thank my friend Bryan Karpowicz for proofreading this manuscript. To my friends here in Atlanta, Petia Bobadova-Parvanova, Venceslav Parvanov, Violeta Yoveva, Nina and Toni Ouzounovi, Tatiana Toteva, Rossi and Jason Davis, Bryan Karpowicz, Paula Agudelo and Carlos Hoyos, thank you for your support and friendship. And finally, thanks to my cat Elmo, whose purring and cuddling relaxed me during the stressful times.

I would like to think that this work is a small drop in the collective human knowledge that will be used always for good merits.

This research in this dissertation was funded in part by the NSF and ONR grants.

TABLE OF CONTENTS

LIST OF TABLES

LIST OF FIGURES

SUMMARY

The potential of atmospheric dust aerosols to modify the Earth's environment and climate has been recognized for some time. However, predicting the diverse impact of dust has several significant challenges. One is to quantify the complex spatial and temporal variability of dust burden in the atmosphere. Another is to quantify the fraction of dust originating from human-made sources.

This thesis focuses on the spatiotemporal characterization of sources and dust outbreaks in Central and East Asia by integrating ground-based data, satellite multi-sensor observations, and modeling. A new regional dust modeling system capable of operating over a span of scales was developed. The modeling system consists of a dust module DuMo, which incorporates several dust emission schemes of different complexity, and the PSU/NCAR mesoscale model MM5, which offers a variety of physical parameterizations and flexible nesting capability.

The modeling system was used to perform for the first time a comprehensive study of the timing, duration, and intensity of individual dust events in Central and East Asia. Determining the uncertainties caused by the choice of model physics, especially the boundary layer parameterization, and the dust production scheme was the focus of our study. Implications to assessments of the anthropogenic dust fraction in these regions were also addressed.

Focusing on Spring 2001, an analysis of routine surface meteorological observations and satellite multi-sensor data was carried out in conjunction with modeling to determine the extent to which to this integrated data set can be used to characterize the spatiotemporal distribution of dust plumes at a range of temporal scales, addressing the active dust sources in China and Mongolia, mid-range transport and trans-Pacific, long-range transport of dust

outbreaks on a case-by-case basis.

This work demonstrates that adequate and consistent characterization of individual dust events is central to establishing a reliable climatology, ultimately leading to improved assessments of dust impacts on the environment and climate. This will also help to identify the appropriate temporal and spatial scales for adequate intercomparison between model results and observational data as well as for developing an integrated analysis methodology for dust studies.

CHAPTER I

INTRODUCTION

Mineral dust aerosols generated by wind erosion are among the most abundant and important aerosol species in the atmosphere. Each year, several billion tons of soil dust is entrained from natural arid and semiarid regions as well as newly formed anthropogenic (human-made) dust sources. Once lifted into the atmosphere, dust particles play an important role in the Earth's system [*Tegen and Fung*, 1994; *Sokolik et al.*, 2001; *Prospero et al.*, 2002]. Because of their ability to scatter and absorb ultraviolet, visible, and infrared radiation, dust aerosols can affect the Earth's radiative balance directly, leading to either heating or cooling of the climate system [*Sokolik and Toon*, 1996; *IPCC*, 2001]. In addition, radiative heating or cooling occurring within the dust layer itself affects the temperature profile and, hence, thermodynamics and dynamics of the atmosphere [*Golitsyn et al.*, 2002; *Jung et al.*, 2005]. Airborne dust influences the surface-air exchange processes and causes changes in the sensible and latent heat fluxes, thus leading to changes in the Planetary Boundary Layer (PBL) physics. Furthermore, dust particles can interact with other atmospheric aerosols and clouds affecting cloud properties [*Sassen et al.*, 2003] and atmospheric chemistry [*Iziomon and Lohmann*, 2003]. Mineral dust is directly linked to iron fertilization as a part of the biogeochemical cycle in the oceans [*Mahowald et al.*, 2005] Dust also affects the agriculture and terrestrial ecosystems [*UNCCD*, 2001] and poses a major health threat when coated with other pollutants over industrial regions [*He et al.*, 2003].

Despite the many important roles of mineral dust, its effects on the climate system remain poorly quantified [*Sokolik et al.*, 2001; *IPCC*, 2001; *Zender et al.*, 2004]. Up to date,

we don't have reliable estimates of the global dust burden [*Tegen*, 2003]. Part of the problem stems from the diverse geographical distribution of dust sources and the existing large uncertainty in the current assessment of the natural and anthropogenic dust fraction [*Tegen et al.*, 2004; *Mahowald et al.*, 2004]. Over the last few decades, regional climate change and anthropogenic disturbance of land surfaces have been suggested to have a significant contribution to the modern dust load in the atmosphere [*IPCC*, 2001]. In particular, Central and East Asia, which are the focus of this thesis, has experienced the most significant land use changes, leading to severe land degradation and creation of new anthropogenic deserts [*Gong et al.*, 2003; *Zhang et al.*, 2003b; *Singer et al.*, 2003].

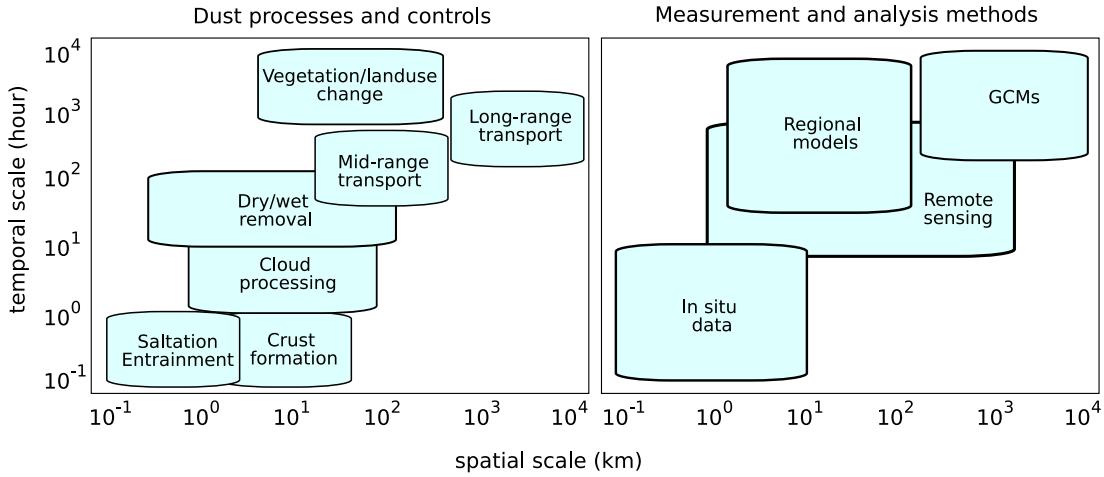

Figure 1: a) Dust processes and their controlling factors; b) Methods used to study dust-cycle processes.

Another fundamental problem that renders quantification of mineral dust impacts problematic is the limited data on dust life cycle processes at relevant spatial and temporal scales [*Kohfeld et al.*, 2005]. The complexity of the problem stems from the fact that dust processes span over five orders of magnitude in space and time (Figure 1). To correctly describe and quantify the dust cycle, one needs to understand equally well local-scale processes such as saltation and entrainment of individual dust particles as well as large-scale

phenomena such as long-range transport of dust plumes. Some other dust processes operate at intermediate scales, which also must be adequately characterized. For instance, interactions of clouds with dust particles, referred to as cloud processing, eventually lead to wet removal of dust during precipitation events. Airborne dust particles also experience dry removal controlled by gravitational settling. Both wet and dry removal processes occur on a variety of spatiotemporal scales depending on the meteorological conditions and spatiotemporal distribution of the dust plume itself. In addition, mineral dust ages by interacting with other chemical species in the atmosphere during its mid- and long-range transport.

All dust processes discussed above occur at some characteristic spatial and temporal scales, and they have to be measured and modeled at similar scales. However, dust modeling is often performed using the General Circulation Models (GCMs), despite their coarse spatial resolution (1.5 – 5°). The current difficulties in describing dust processes in global models make it impossible to quantify the magnitude of dust impacts with high level of confidence [*IPCC,* 2001]. Even the magnitude of total dust emission remains uncertain. Recent assessments with GCMs give a wide range of total dust emission between 430 and 9000 Mt/year [*Tegen,* 2003]. Conflicting results were reported with respect to the fraction of anthropogenic dust predicted with GCMs [*Mahowald et al.*, 2004; *Tegen et al.*, 2004]. In many instances the area of dust sources is comparable to or smaller than the GCM grid size. In addition, dust processes are sporadic, spatiotemporally intermittent and show strong regional dependence. The traditional metrics based on daily or monthly means which are commonly used for model evaluations against observations fails to capture the true physical nature of dust processes and their characteristic scales. Thus, other approaches that can capture the timing and duration of individual dust events are needed.

Regional mesoscale circulation models are better suited for simulations of individual dust outbreaks. Their finer spatiotemporal resolution allows for more realistic representation of the topography, soil conditions and mesoscale circulations, and enables better

validation against observations. Thus, a regional dust modeling system able of predicting the timing, duration and intensity of a dust event at fine spatiotemporal scales will be a powerful tool for the improved prediction of the atmospheric dust loading. Developing such a modeling system is one of the goals of this thesis.

Despite some apparent advantages, regional models, similarly to global models, rely on a dust emission scheme to predict dust fluxes. Dust schemes range from simple type schemes, in which the vertical dust flux depends on a prescribed erodible fraction and fixed threshold friction velocity (or threshold surface wind), to advanced schemes, in which a threshold value of friction velocity is predicted as a function of surface soil characteristics [*Marticorena and Bergametti*, 1995; *Lu and Shao*, 2001]. The choice of a particular dust emission scheme will affect the predicted dust mass. None of the existing dust modeling studies either with regional or global models have addressed this issue in detail. Furthermore, dust emission strongly depends on wind forcing [*Bagnold*, 1941; *Chepil*, 1945]. Therefore any uncertainty in the model predicted winds will be reflected in the emitted dust mass. A reasonable question arises regarding what is the appropriate PBL parameterization that correctly represents the boundary layer dynamics in arid and semi-arid regions. Many studies focused on the comparison of the model predicted winds calculated with different PBL parameterizations mainly for the purpose of improving weather forecasting [*Zhang and Zheng*, 2003; *Liu et al.*, 2004]. None of these studies have addressed the implications for dust emission. This work explores this issue by investigating how the selection of a dust production scheme and PBL parameterization will affect the emitted dust mass and the intensity of individual dust outbreaks.

Another problem stems from the simplification of land surface processes in dust emission models. Dust emission shows complex hysteresis behavior as a function of soil properties [*Raupach and Lu*, 2004]. There is a threshold wind velocity, below which dust emission does not occur, and it strongly depends on the soil moisture, aerodynamic roughness length, and size distributions in the parent soils [*Gillette et al.*, 1980]. Due to limited data

of these critical parameters, global and regional models often prescribe constant threshold wind velocity over the entire simulation domain. It has been acknowledged [*Marticorena et al.*, 1997; *Shao*, 2001; *Zender et al.*, 2003] that fixed threshold velocities simplify the spatiotemporal dynamics of wind erosion within the model domain. A recent study by [*Zhao et al.*, 2006] estimates the discrepancies in dust emission as a result of the use of two different advanced emission schemes for the East Asian region. However, detailed comparison between dust fluxes produced with simple and advanced emission schemes has never been performed for Central and East Asian dust sources. Given the lack of input data, can one always justify the use of an advanced dust emission scheme instead of a simple one? This work addresses these issues by investigating the discrepancies in the model predicted dust mass as a result of using fixed versus variable threshold wind velocity over the regions of interest.

Several regional modeling systems have been developed over the recent years for dust studies [*Lu and Shao*, 2001; *Liu and Westphal*, 2001; *Uno et al.*, 2001; *Gong et al.*, 2003]. However, each of them relies on a particular PBL parameterization and a dust production scheme, which results in biases in the estimated dust loads. The modeling systems have been applied predominantly to East Asia, while dust sources and outbreaks in Central Asia have never been explored in detail by any of them. In addition, the existing regional models rarely take into account the spatial dynamics of dust sources as a result of human induced land cover changes. This work addresses the above limitations by developing a modeling system that is able to: (1) estimate the range of uncertainties in the model predicted dust loads associated with the use of different PBL parameterizations and dust emission schemes, and (2) assess the anthropogenic dust fraction as a result of the land cover changes in both Central and East Asia.

Both ground-based and satellite observations can be employed in dust studies to constrain model results and minimize the existing discrepancies in the simulated dust events. Meteorological surface measurements, in particular, have been carried out systematically

from numerous stations over the world. Meteorological parameters such as surface winds and visibility have been commonly used in past studies of dust outbreaks [*Shao and Wang*, 2003; *Sun et al.*, 2001]. However, the climatology derived from ground-based observations varies significantly between these studies [*Chen and Chen*, 1987; *Goudie and Middleton*, 1992]. To date, there is no consistent definition of a dust event. It remains to be shown the extent to which surface measurements can be used to characterize dust events in the source region and for validation of their mid- and long-range transport. Can surface visibility measurements be used as a reliable proxy for detection and tracing of atmospheric dust outbreaks and/or for constraining the dust emission models? This work attempts to answer all these questions.

During the last decade, remote sensing has proved to be a valuable tool for characterization of dust sources and outbreaks [*Husar*, 2001; *Prospero et al.*, 2002; *Chung et al.*, 2003]. A number of geostationary and polar orbiting satellites are currently available to provide observations of dust outbreaks on regional and global scales. Many challenges still remain to be addressed in the satellite products such as the accuracy of aerosol retrievals, cloud contamination, and data acquisition times [*Darmenov and Sokolik*, 2005; *Brennan et al.*, 2005]. Some central questions are: What spatiotemporal resolutions of dust coverage can be achieved from existing spaceborne instruments? Do dust spatial distributions inferred from different satellite products agree enough to provide a reliable constraint for dust transport models? This work addresses these questions by analyzing several satellite aerosol products in conjunction with ground- based observations.

The results of the thesis are presented in three chapters reflecting its threefold goal:

1. Develop a regional dust modeling system capable of operating at a span of scales and assess its capability in predicting the timing, duration and intensity of individual dust events.

2. Focusing on Spring 2001, examine the extent to which the routine surface meteorological observations (including visibility) and satellite data can be used to characterize the spatiotemporal distribution of dust plumes at a range of temporal scales, addressing the active dust source regions in China and Mongolia, mid-range transport and trans-Pacific, long- range transport of dust outbreaks on a case-by-case basis.

3. Using the developed regional dust modeling system, investigate an anthropogenic dust signal due to land-use/land-cover changes in Central and East Asia and associated uncertainties.

Chapter II describes a newly developed dust modeling system consisting of a dust module DuMo and the mesoscale model MM5. It investigates the effect of model physics, spatial resolution and dust emission scheme on the predicted timing, duration and intensity of individual dust outbreaks, addressing the specifics of dust sources in Central and East Asia.

Chapter III focuses on analysis of the collective capabilities of ground-based and satellite data to identify active dust source regions, duration, mid- and long-range transport of dust outbreaks on a case-by-case basis. We also examine the potential of meteorological time series for constraining the dust emission schemes used in aerosol transport models.

Chapter IV presents the results of the assessment of anthropogenic dust fraction in Central and East Asia within the scope of the findings in Chapters II and III. It also discusses the challenges in discriminating natural from anthropogenic sources and estimates the uncertainties in dust loads associated with different desertification scenarios in East Asia. The effects of newly formed anthropogenic deserts at the regional level are explored to gain a better understanding about the effect of dust on the climate system.

The findings of the thesis are summarized in Chapter V.

CHAPTER II

INVESTIGATION OF THE TIMING, DURATION AND INTENSITY OF INDIVIDUAL DUST EVENTS WITH A NEW REGIONAL DUST MODELING SYSTEM

2.1 Introduction

Global and regional transport models are widely used to quantify the diverse impacts of dust on the climate system [*Tegen and Fung*, 1994; *Ginoux et al.*, 2001; *Uno et al.*, 2001; *Zender et al.*, 2004]. However, modeling mineral dust is a demanding task since processes controlling dust cycle are threshold-dependant, hysteretic and highly intermittent in both space and time [*Raupach and Lu*, 2004]. Considerable knowledge of these processes was acquired by theoretical research, local scale studies and numerical simulations [*Shao*, 2001; *Tegen*, 2003]. Nevertheless, incorporating the existing information on local scales into numerical models is hampered by the existence of many unknown parameters and subgrid spatiotemporal heterogeneities that often have to be described separately.

Dust modeling is often performed using General Circulation Models (GCMs). Coarse spatiotemporal resolution of global models, their limited representation of physical processes and the lack of observational data on global scales make integrative mineral dust modeling on larger scales a challenging issue. The traditional climatology based on daily or monthly means, which is commonly used in global model evaluations against observations, fails to capture the true physical nature of dust processes and their characteristic scales. Thus, other approaches being able to represent the timing and duration of individual dust events are needed.

Regional forecast models are better suited for simulations of individual dust outbreaks.

Their finer spatiotemporal scales promote a detailed representation of atmospheric circulation patterns, and enable better validation against observations. Thus, a regional dust modeling system able of predicting the timing, duration and intensity of a dust event at fine spatiotemporal scales will be a necessary tool for improved prediction of the atmospheric dust loadings. This chapter discusses the development of such system consisting of the dust module DuMo and the PSU/NCAR Mesoscale Model MM5. DuMo is specifically developed to incorporate several dust emission schemes of different complexity and to provide the capability for advanced treatment of land surface properties for determining the threshold friction velocity. MM5 offers multiple choices of physical parameterizations, flexible nesting capability, variable resolution land surface datasets and real-data inputs. The MM5 terrestrial data preprocessor was modified in this study to allow for user-defined changes in the land-use and water mask within a domain of interest. This enables us to reproduce anthropogenic land cover changes (see Chapter IV). The developed modeling system is capable of simulating the timing, duration and intensity of individual dust events at a range of spatial and temporal resolutions.

Regional models have apparent advantages in terms of spatiotemporal resolution compared to global models. However, they also rely on different initializations and physical parameterizations, and it can be expected that dust loads will differ from model to model. *Liu and Westphal* [2001], considering a dust episode in China, showed that even within the same numerical model (Navy's COAMS) there is a significant difference in the predicted wind fields, instantaneous dust fluxes and daily dust integrals, depending on the model resolution. In addition, *Liu and Westphal* [2001] pointed out that surface winds are modified by the local topography, surface characteristics and thermal circulations. They also stated that numerical simulations of these processes are known to be dependent on the model grid resolution. However, their study addressed only a limited number of cases and did not perform a detailed investigation of these issues. To this end, a number of questions arise: What is the impact of the model spatial resolution (spanning from a fine grid of 10 km

up to a coarse grid of 200 km) on the model-predicted dust events? Is it possible to take into account the grid variability of surface winds and soil properties (and threshold friction velocity) to treat them consistently across the scales? Is it feasible to introduce a subgrid parameterization of dust emission for the global models in order to decrease the existing uncertainties? This work addresses these questions by applying the new modeling system for a range of grid cell spatial resolutions to dust sources in Central and East Asia.

However in addition to the spatiotemporal resolution, modeling of dust entrainment strongly depends on the selection of a dust emission scheme. A number of different dust emission schemes have been developed and used in the framework of the global and regional atmospheric dynamical models [*Marticorena and Bergametti*, 1995; *Tegen and Fung*, 1994; *Ginoux et al.*, 2001; *Gong et al.*, 2003; *Zender et al.*, 2003]. Dust emission schemes can be divided broadly into those formulated in terms of surface wind speed taken at 10 m, U_{10}, (U_{10} - driven schemes hereafter) and those expressed in terms of the surface friction velocity, u_*, (u_* - driven schemes hereafter). Although for a neutrally stable PBL, u_* and U_{10} can be related via a logarithmic wind profile and surface roughness, in general the relation between u_* and U_{10} and, hence, predicted dust fluxes depend on the choice of the PBL parameterizations as well as on the land model. Furthermore, several u_* - driven schemes exist in the literature that were derived under somewhat different physical assumptions [*Shao*, 2001]. Thus, to better quantify the model-predicted dust outbreaks, it is important to understand the uncertainty in dust emission caused by model-dependent physics and use of different dust emission schemes. In this chapter we address the following questions: How does the choice of the PBL parameterization affect the predictions of dust fluxes? For a given PBL, what are the differences between U_{10} - driven and u_* - driven dust fluxes? Are there any noticeable differences in dust fluxes calculated with different u_* - driven schemes?

This chapter also describes a new advanced dust emission scheme which was developed in our study for dust sources in Central and East Asia following the approach of

Draxler et al. [2001]. This enables us to investigate differences in dust emission predicted with simple dust production schemes (which are commonly used in GCMs) versus that simulated with an advanced scheme which takes into account land surface properties. We attempt to answer the following question: what are the differences between vertical dust fluxes calculated with a fixed threshold speed (simple dust schemes) and those that account for changes in surface roughness and threshold velocity over the simulation domain (advanced dust schemes)? The implications of these differences to the assessment of the anthropogenic dust fraction will be discussed in Chapter IV.

2.2 Methods

This study utilized our newly developed dust modeling system consisting of the dust module DuMo and the mesoscale model MM5. MM5 was run in a single nest and 1-way nested configurations to simulate the meteorology of representative dust outbreaks in Central and East Asia occurring in the spring seasons of 2001, 2003 and 2004.

First, MM5 was run with two PBL parameterizations to simulate the meteorological fields. Then, emitted dust fluxes were computed by feeding meteorological fields into the dust module DuMo consisting of several dust emission schemes of different complexity. The MM5 model physics (with a focus on PBL parameterizations) and dust model DuMo used in this work are described next.

2.2.1 MM5 model physics

The MM5 model offers a variety of advanced physical parameterizations of precipitation, atmospheric radiation, land surface and planetary boundary layer.

Precipitation schemes in the MM5 are divided into two groups: explicit and implicit. Explicit schemes handle resolved (grid scale) precipitation physics, while implicit schemes deal with non-resolved (sub-grid scale) precipitation physics. Each of these processes can occur in the same grid box throughout the model run and at the same time. In our runs

we used the “simple ice” explicit scheme that adds ice phase processes to the warm rain scheme. The explicit treatment of cloud water, rainwater, snow and ice allows for ice-phase processes below 0 °C, where the cloud water is treated as cloud ice and rain is treated as snow. In addition, we chose the Grell implicit cumulus parameterization scheme. This scheme is based on the rate of destabilization of a single cloud with updraft and downdraft fluxes and compensating motion determining the heating and moistening profile.

Atmospheric radiation options in MM5 range from schemes that consider no mean tendency being applied to the atmospheric temperature to schemes, which incorporate multiple spectral bands in shortwave and longwave. For our simulations we selected the “simple radiation” option, where atmospheric cooling rates depend just on the temperature.

The MM5 has several options for a land surface model, LSM. Here we used an improved “slab model” with a five-layer soil model having the thicknesses of each layer from the top to bottom of 1, 2, 4, 8, and 16 cm [*Dudhia*, 1996]. We chose this particular scheme because it supports both Medium-Range Forecast (MRF hereafter) and Blakadar (BLK hereafter) parameterizations considered in this study, though it is not the most advanced LSM incorporated into MM5. The choice of LSM does affect the meteorological characteristics predicted with a mesoscale model, especially in the boundary layer. For instance, the parameterization of soil moisture can affect the sensible and latent heat fluxes and hence the boundary layer dynamics. In the five-layer soil model, soil moisture is not predicted but is provided by a look-up table depending on the vegetation category and the season.

The MM5 offers several PBL schemes. Based on test runs, we selected the Medium-Range Forecast, MRF, and Blakadar, BLK, parameterizations for further analysis because they produced the lowest and highest winds, respectively, for the considered dust episodes. This finding is in agreement with prior studies. A sensitivity study performing a high- resolution simulation of the hurricane Bob revealed that the results obtained with the MRF PBL differed significantly from the rest of the MM5 PBL schemes [*Braun and Tao*, 2000]. In particular, MRF predicted stronger vertical mixing and weaker surface winds. *Liu et al.*

[2004] further pointed out that MRF overestimates the friction velocity resulting in excessively weak surface winds. This is in agreement with a study by *Zhang and Zheng* [2003] confirming that the majority of PBL schemes incorporated in MM5 underestimate the observed winds at 10 m during the daytime, and MRF, in particular, showed overall the lowest values for the case of summertime weak-gradient flows. In contrast, the BLK PBL scheme produced the highest values of surface winds. Therefore, considering MRF and BLK schemes, which give the lower and higher winds, enables us to assess the range of uncertainties in dust emission due to model-dependent meteorological fields. Since these PBL schemes are described in detail elsewhere [*Zhang and Anthes*, 1982; *Hong and Pan*, 1996], we provide only a brief description here.

The BLK scheme contains two modules, which represent turbulent mixing: nocturnal (in which stratification is usually stable) and free-convection. The nocturnal module is based on K-theory, where K is defined by the local Richardson number, and is further subdivided into three categories - stable, damped mechanical turbulence, and forced convection. In the free convection module, the vertical fluxes of heat, momentum, and moisture are calculated using a nonlocal mixing model in which vertical exchanges occur between the lowest layer and each level in the mixed layer. The magnitude of z_h/L, where z_h is the height of the mixed layer and L is the Monin- Obuhov length, determines which module is to be used. The physical meaning of L is the height above which convectively driven turbulence overwhelms mechanically driven turbulence. For instance, in the case of a stable layer, the vertical heat flux is small; therefore, L is large and the magnitude of z_h/L is small.

The MRF PBL has been widely used in the MM5 model for various applications. It has been believed that this scheme provides a realistic representation of the well-mixed layer [*Hong et al.*, 2003]. The MRF scheme uses a first-order vertical diffusion scheme [*Hong and Pan*, 1996]. The PBL height is diagnostically determined in this scheme. The Bulk-Richardson approach is used to iteratively estimate a PBL height starting from the

ground upward. To achieve this, the turbulent diffusion coefficients are calculated from a prescribed profile shape as a function of PBL height and scale parameters derived from the similarity theory [*Medium Range Forecast Model Description, 1988*].

Recently, *Liu et al.* [2004] proposed several improvements to the MRF PBL by adopting the *Beljaars* [1994] formulation of surface fluxes. They also introduced a new approach for calculations of the PBL height that uses the local Richardson number instead of the deep-layer Richardson number. These modifications were implemented in the latest version of the MM5 used in our study.

Within the BLK PBL, the friction velocity u_*, which is a key parameter in dust emission schemes, is a function of wind speed at the lowest model layer, convective velocity, roughness length, and the surface scaling parameters. The latter scaling parameters depend on the stability regime, which is determined by the sign and magnitude of the bulk Richardson number as well as by the Obukhov length. In turn, the MRF PBL scheme handles u_* as a function of the mixed layer velocity, and the wind profile function is evaluated at the top of the surface layer for different stability regimes.

2.2.2 Dust emission module DuMo

The dust emission module DuMo consists of several dust production schemes of different levels of complexity. To a large extent the nature of complexity of a dust emission scheme comes from the treatment of land surface properties for determining the threshold friction velocity [*Gillette et al.*, 1998; *Alfaro and Gomes*, 2001; *Shao et al.*, 2003]. Dust schemes range from simple type schemes, in which the vertical dust flux depends on a prescribed erodible fraction and fixed threshold friction velocity (or threshold surface wind), to advanced schemes, in which a threshold value of friction velocity is predicted as a function of surface soil characteristics [e.g. *Marticorena and Bergametti*, 1995]. Due to the lack of data needed for the advanced schemes, the global and regional models often rely on simple schemes [e.g. *Uno et al.*, 2001; *Liu and Westphal*, 2001; *Tegen and Miller*, 1998]. Here we

compare several dust emission schemes listed in Table 1, including four different formulations of the u_* - driven scheme and one U_{10} - driven scheme. All these schemes were used in past studies dealing with regional or global dust emission modeling. Some examples of these studies are cited in Table 1.

Compared u_* - driven schemes depend either on the third or forth power of the friction velocity, hereafter called u_*^3 - driven and u_*^4 - driven schemes, respectively. Although the W79 scheme is a result of a typographical error in *White* [1979], we also included it in our comparison because several studies employed this incorrect expression in dust emission modeling. Furthermore, *Namikas and Sherman* [1997] demonstrated that despite the incorrect formulation the W79 scheme gives reasonable results compared to other emission models as well as observational data.

The vertical dust flux predicted with simple dust emission schemes is a function of threshold wind speed U_{10th} (or threshold friction velocity u_{*th}), dust erodible fraction f representing the efficiency of the model grid cell to produce dust, and dimensional constant C.

The dust module also has abilities for advanced treatment of land surface properties by calculating the threshold velocity for each grid cell using the information on roughness length and threshold velocity over a smooth surface [*Draxler et al.*, 2001; *Marticorena and Bergametti*, 1995]. Dust fluxes calculated with variable threshold velocity were compared against ones obtained with fixed threshold velocity over the entire domain.

Dust production also depends on the soil moisture and DuMo has the capability to take into account this parameter. The 5-layer slab model used in our simulations (see Section 2.2.1) has limited abilities to account for the changes in soil moisture because it relies on seasonal moisture availability prescribed for each land-use category. However, given the low soil moisture availability and patchy precipitation in the Central and East Asian domains for the considered time period, we expect that changes in soil moisture, if any, have a negligible effect on total lifted dust mass that is of interest here.

Table 1: Dust emission schemes compared in this study.

Study	Dust production scheme	
	u_* - driven schemes	
Kawamura [1964] *White* [1979][a] *Marticorena and Bergametti* [1995][b] *Gong et al.* [2003][b] *Zender et al.* [2003][b]	$F = C_{MB95} u_*^3 \left(1 + \frac{u_{*th}}{u_*}\right)\left(1 - \frac{u_{*th}^2}{u_*^2}\right)$	MB64
Owen [1964][b] *Shao et al.* [2002] *Draxler et al.* [2001] *Okin and Gillette* [2004][b]	$F = C_{O64} u_*^3 \left(1 - \frac{u_{*th}^2}{u_*^2}\right)$	O64
Gillette and Passi [1988] *Liu and Westphal* [2001][c] *Nickling and Gillies* [2004][c]	$F = C_{GP88} u_*^4 \left(1 - \frac{u_{*th}}{u_*}\right)$	GP88
White [1979][d] *Sarre* [1988] *Pankine and Ingersol* [2002]	$F = C_{W79} u_*^3 \left(1 - \frac{u_{*th}}{u_*}\right)\left(1 + \frac{u_{*th}^2}{u_*^2}\right)$	W79
	U_{10} - driven schemes	
Tegen and Fung [1994][e] *Liu and Westphal* [2001][f] *Uno et al.* [2001][e] *Ginoux et al.* [2004][f] *Mukai et al.* [2004][e] *Cakmur et al.* [2004][e] *Barnum et al.* [2004][e]	$F = C_{U_{10}} U_{10}^3 \left(1 - \frac{U_{10th}}{U_{10}}\right)$	U10

[a] Correct formulation of saltation flux.
[b] Used horizontal saltation flux G to calculate vertical flux F assuming proportionality between F and G.
[c] Used $F = C u_*^4$ for $u_* > u_{*th}$.
[d] Formulation with a typographical error.
[e] Used surface winds.
[f] Used U_{10} winds.

2.3 The effect of spatial resolution on model-predicted dust events

2.3.1 Modeling setup and approach

Dust emission schemes show power law dependence between dust flux and wind speed and a linear dependence between fluxes and threshold wind speed (see Table 1). It is obvious that small changes in surface winds would result in large changes in dust fluxes. Both wind speed at 10 m and friction velocity u_* used to drive dust emission schemes depend on the model-predicted wind at the lowest model level. Therefore accurate prediction of winds in the PBL is critical for reliable estimation of dust emission. The selection of either U_{10} or u_* for calculation of vertical dust fluxes is dictated by the particular need that the modeler is trying to achieve or by the capability of the numerical model. Some models do not allow parameterization of u_* and only the choice of U_{10} is available. On the other hand U_{10} can be directly compared with operational observations from meteorological stations. Observations of surface friction velocity are scarce and not systematically available as U_{10}. Therefore for the purpose of validating dust emission models U_{10} seems like a logical variable easily compared with observational data. Thus, to investigate the effect of model grid spatial variability we selected the U_{10} - driven scheme listed in Table 1:

$$F = Cf(U_{10} - U_{10th})U_{10}^2 \tag{1}$$

where C is the dimensional constant ($kg\,s^2m^{-5}$), f is the dust erodible fraction, and U_{10th} is the threshold speed for dust lifting. Unlike U_{10}, the threshold speed U_{10th} and the erodible fraction f mainly depend on surface properties. Both the erodible fraction and surface wind speed are likely to be affected by the model spatial resolution. Our erodible fraction is based on the USGS land-use category classification incorporated into MM5. For each land type within the model grid, we assigned a number between 0 and 1 representing its ability to produce dust. For instance, the erodible fraction for herbaceous wetland is 0.1 while for barren or sparsely vegetated land it is 0.9. An overlapping parabolic interpolation

procedure, incorporated in MM5 preprocessing modules, was used to re- calculate the land-use categories at different spatial resolution. The erodible fraction in *Liu and Westphal* [2001] and *Liu et al.* [2003] was calculated in a similar fashion.

Two study domains were selected covering the active dust sources in Central and East Asia. The domain in East Asia includes the Gobi Desert, located on a high plateau, and the Taklamakan region, characterized by the complex topography (see Figure 2 for the location of the domains). The second domain covers the Aral Sea region, located almost at the sea level. The latter includes a large anthropogenic dust source formed as a result of the drying up of the Aral Sea over the past 50 years.

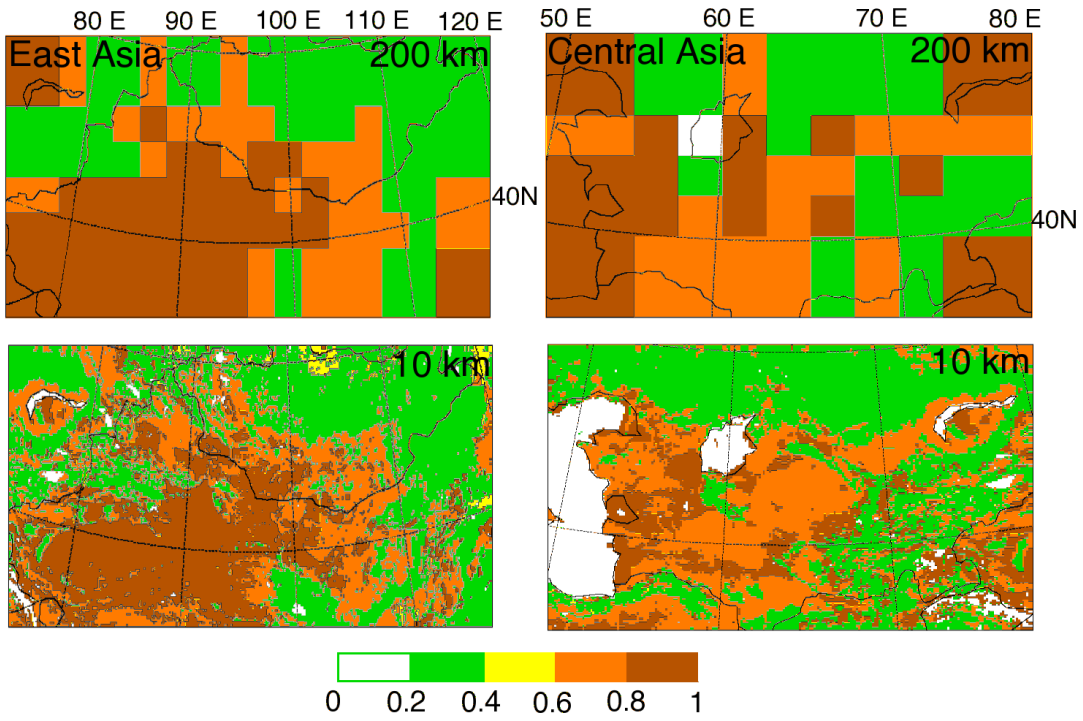

Figure 2: Erodible fraction for Gobi-Taklamakan and Aral Sea source regions at 200 km and 10 km.

To examine dust events of different intensity, several time periods with different meteorological conditions over the study domains were considered. For the Central Asia domain, the MM5 model was run for 6–10 April 2001 and 15–16 April 2003, whereas for East Asia

considered time periods are 6–10 April 2001 and 26–27 March 2004. The simulations were performed for each domain and the model outputs were saved every 20 minutes for runs at 10, 40, 100 and 200 km model resolution.

2.3.2 The effect of model grid size

The erodible fraction depends on the land-use/vegetation categorization and it changes with the model resolution. Figure 2 shows the East and Central Asian domains with the erodible fraction at 200 km, which is a typical GCM resolution, and the 10 km resolution, representative for fine scale regional runs. Clearly, the coarse resolution results in unrealistic values of the erodible fraction because the water body is misinterpreted as a highly erodible area in the Aral Sea region. Comparing simulations for the 10 km and 200 km resolution, one can point out various differences in the predicted erodible fraction that will eventually lead to various biases in dust emission.

To illustrate the effect of the erodible fraction on modeled dust fluxes, we performed two different simulations. Figure 3 shows the area- integrated flux [kg/s] for 120 hours simulation (April 6–10, 2001) for both domains, corresponding to a moderate-to-strong dust event in Central Asia and a severe dust episode in East Asia, based on visibility records and true color satellite images inspection. Figure 3a shows dust fluxes for East Asia at 200, 100 and 40 km normalized by the 10 km flux (the horizontal line at 100%) for $C = 1$, erodible fraction $f = 1$ for all cells in the domain and $U_{10th} = 5.4\,\mathrm{m/s}$. Figure 3b shows the same fluxes calculated with the erodible fraction based on the USGS 25 category vegetation/land- use classification and $C = 1$. Figures 3(c,d) show vertical dust fluxes for the Central Asian source region. It can be seen that the erodible fraction affects dust fluxes at 200 km and the effect is more pronounced for the Aral Sea region, since the coarse model grid introduces the area with an erodible fraction of 0.6 to 0.8 over the water body. Since dust emission is linearly proportional to the erodible fraction, an increase of the latter will lead to an overall increase of dust mass emitted in the region. However the effect is less

pronounced over the East Asian domain. The likely reason is that this domain includes vast arid and semi-arid lands and thus the erodible fraction remains high regardless of the model grid. In contrast, the Central Asian domain consists of variety of vegetation types as well as the Caspian and Aral Seas. As a result the changes in model grids strongly affect the erodible fraction and thus simulated dust fluxes.

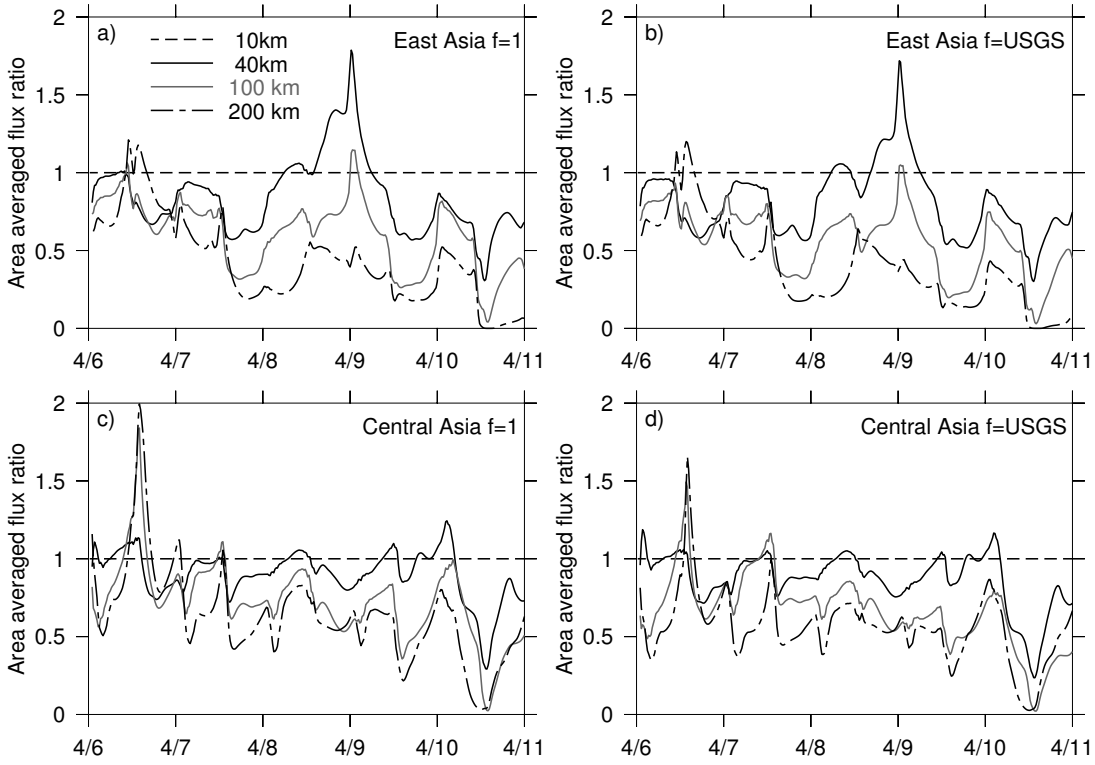

Figure 3: a) Vertical dust fluxes at 40, 100 and 200 km normalized by 10 km flux, $C = 1$, $f = 1$; b) Same with $C = 1$ and f based on 25 category USGS landuse/vegetation classification; c) Same as a) but for Central Asia; d) Same as b) but for Central Asia.

As expected, even for the same erodible fraction, dust fluxes are quite different (see Figure 3). This behavior can be only due to differences in the surface winds. A diurnal variation of surface winds can be observed that follows closely the diurnal evolution of the boundary layer. Also increasing the model resolution leads to an overall decrease in the area-integrated vertical flux. This implies that using coarse model resolution will result in lower dust loads and will affect the estimates for the intensity of the dust event. This result

is somewhat different from the findings of *Liu and Westphal* [2001]. They showed that, for the two-week period in April 1998, vertical dust fluxes at the finer resolution were smaller than those at the coarse resolution during half of the simulated time period for both U_{10} - and u_* - driven fluxes. For our 5-day simulations (see Figure 3) the fluxes at the coarse resolution are overall smaller than fluxes at fine resolution during most of the times.

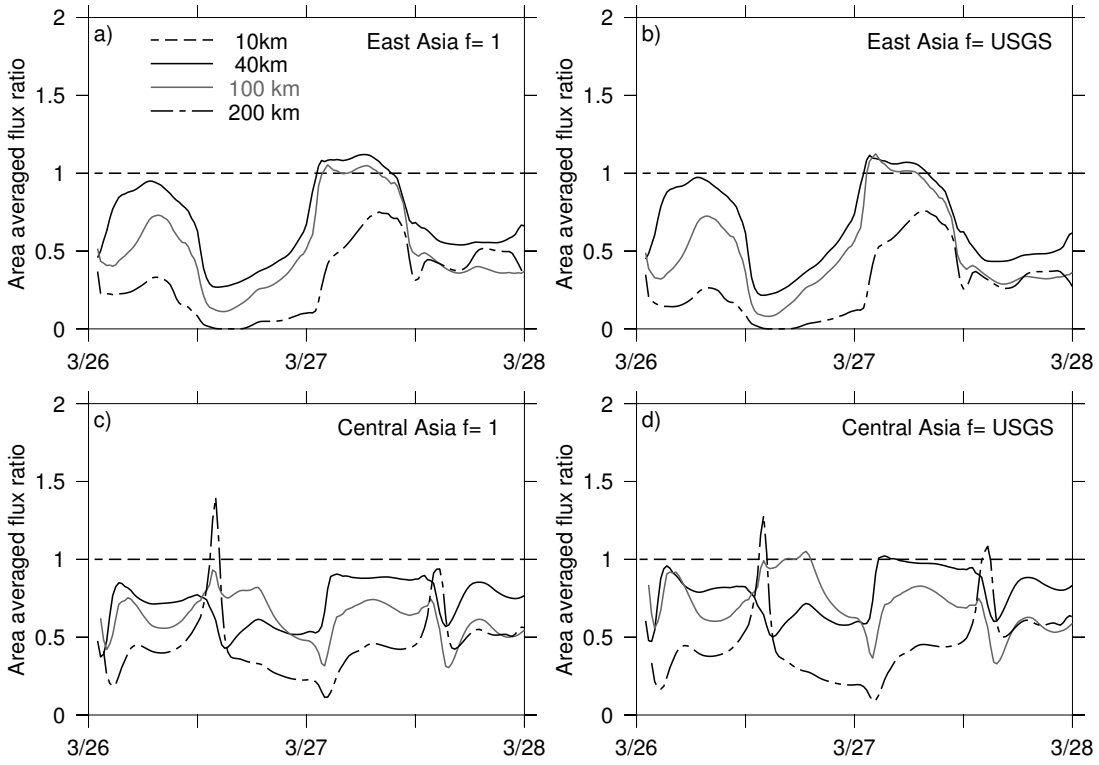

Figure 4: Same as Figure 2 but for 2003 and 2004.

Figure 4 shows dust fluxes predicted for a moderate dust storm occurred in the Gobi-Taklamakan region on March 26–27, 2004, and a moderate- to-weak dust storm started on April 15–16, 2003 in the Aral Sea region. Both cases show a similar behavior of decreasing winds with an increase of model spatial resolution. An interesting fact is observed for the 200 km resolution for the East Asian domain - for about 18 hours during the 48-hour simulation the winds over the entire domain were practically zero suppressing dust emission. For the 2001 dust event case over the same domain, there is a similar pattern of 4 hours out

of 120-hour simulations, where winds are close to zero for the entire domain resulting in a lack of dust emission. However at finer resolution this effect is missing. This leads us to a conclusion that coarse resolutions tend to underestimate surface winds and thus dust emission. This conclusion is in agreement with the results presented by *Cakmur et al.* [2004]. Our finding has an important implication for the estimated duration of model-predicted dust events at coarser resolution - it is evident that global models will underestimate the duration of individual dust outbreaks.

Table 2: Total emitted soil mass normalized to 10 km resolution for the entire period of simulation calculated with f based on USGS 25 category landuse and $U_{th} = 5.4\,\mathrm{m/s}$.

	East Asia		Central Asia	
Resolution	Total mass %	C_r	Total mass %	C_r
	Apr 6-10, 2001		Apr 6-10, 2001	
10	100	1.0	100	1.0
40	91	1.1	94	1.1
100	66	1.5	79	1.3
200	44	2.3	58	1.7
	Apr 26-27, 2004		Mar 15-16, 2003	
10	100	1.0	100	1.0
40	87	1.1	87	1.1
100	70	1.4	73	1.4
200	39	2.5	43	2.3

Table 2 compares the total dust mass simulated at 40, 100 and 200 km resolution, normalized to that calculated at 10 km resolution for both dust source regions. These calculations were done with f based on the USGS 25 land-use/vegetation categories and $U_{10th} = 5.4\,\mathrm{m/s}$. The dimensional constant C is set to be 1 for the 10 km resolution and C_r is defined as the ratio between C at the 200, 100 and 40 km resolution and C at the 10 km resolution. C_r illustrates how much we have to tune C to match the fluxes when changing the resolution. Table 2 indicates that regardless of the source region and for a fixed threshold wind speed, C_r is almost a constant number as a function of the spatial resolution for the selected cases of moderate and severe dust storms. For instance, C at

40 km resolution has to be increased 1.1 times to match C at 10 km resolution. Likewise C at 200 km is on average 2.2 times smaller than C at 10 km. In addition, we calculated the ratios for threshold speed of 6 and 6.5 m/s (not shown). We found that these ratios remain almost constant despite the change in the threshold speed in the case of strong dust events and do not change significantly during moderate dust events. Since our simulations are performed for two different source regions and under different meteorological conditions, we are confident in the consistency of the results.

Vertical dust fluxes were calculated also for U_{10th} = 0, 2, 4, 6 and 6.5 m/s. Although the shape of the curves remained the same, the total lifted mass decreased with increasing of the threshold wind speed as expected due to the higher threshold required for lifting dust. In addition, increasing the threshold speed resulted in an increased period with zero emission from the entire domain for the coarse resolution runs. For instance, for 2001 simulations over East Asia at the 200 km resolution for the threshold speed of 6 m/s and 6.5 m/s, dust emission from the entire domain was zero for 6 and 8 hours, respectively.

Figure 5 shows the combined effect that the threshold wind speed and model grid resolution have on the total lifted dust mass for the 2001 simulation over the East China domain. One can see that by varying the threshold speed the same dust flux can be emitted at different model grid resolutions. Thus, it seems to be possible to adjust the flux at the coarse resolution by decreasing the threshold wind speed.

2.3.3 Spatial downscaling: the effect of subgrid wind variability

A number of studies pointed out that the coarse resolution of GCMs hampers the representation of subgrid strong wind events [e.g. *Tegen*, 2003; *Cakmur et al.*, 2004]. To account for subgrid variability, it has been suggested to parameterize the surface wind fields by introducing a Probability Density Function (PDF). The approach for using PDFs to describe natural surface winds is not new and has been used extensively in wind energy applications

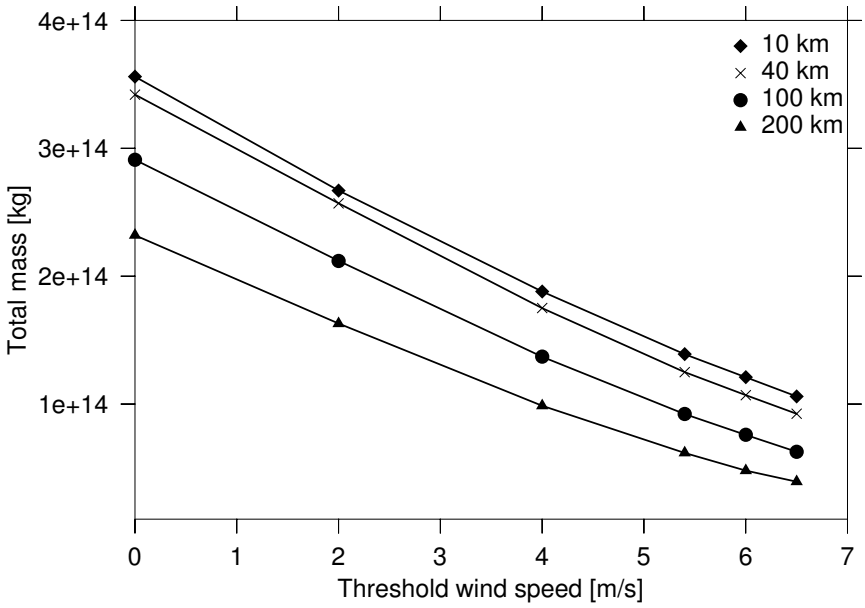

Figure 5: Total lifted mass for the East Asian domain as a function of the threshold wind speed.

[*Justus et al.*, 1978]. As a meteorological variable, the surface wind speed exhibits subscale variations in both space and time [*Westphal et al.*, 1988]. For instance, *Justus et al.* [1978] and *Gillette and Passi* [1988] used Weibull PDF to describe the subtime variation of surface winds while *Cakmur et al.* [2004] and *Grini and Zender* [2004] implemented PDFs to estimate the subgrid variability of winds forecasted by global models. Strictly speaking, wind speed and wind threshold speed vary on both spatial and temporal scales so the expected value of the vertical dust fluxes mathematically can be determined by integrating the multivariate distribution of wind speed over space and time. In their study, *Westphal et al.* [1988] accounted for both the spatial and temporal variability of the surface threshold friction velocity, however they assumed uniform probability over space for a certain range of threshold friction speeds. The lack of simultaneous measurements in arid regions poses a real challenge for implementing statistical methods to estimate the parameters of the PDFs for the case of subgrid variability. For instance, to estimate the variance of subgrid fluctuations, which is a necessary parameter for the bivariate normal PDF, *Cakmur et al.* [2004]

used velocity scales depending on the model variables. However, this approach is model dependent, so changing the model, or even changing the spatiotemporal resolution within the model will lead to a change in the estimated variance.

In this work we focused on the subgrid variability of surface winds and tested the PDF approach for the 200 km resolution domains for Central and East Asia. Since the model output was on every 20 minutes, we assumed that the subtime variations in surface wind speed are relatively small compared to the subgrid variations in a 200 km grid cell. We tested two PDFs - Bivariate normal [*Cakmur et al.*, 2004] and Weibull [*Grini and Zender*, 2004] Dust emission was computed using Equation 1 according to the fraction of the PDF that exceeds the threshold value:

$$F = Cf \int_{U_{th}}^{\infty} U^2 (U - U_{th}) p(U) dU \tag{2}$$

where $p(U)$ is the probability density function. We followed the approach of *Cakmur et al.* [2004] for developing, simplifying and calculating the bivariate normal PDF [see *Cakmur et al.*, 2004, eq. 5–7] The vertical dust flux F (equation 7 in Cakmur et al.) is written as:

$$\begin{aligned} F(\overline{U}, U_{th}, \sigma) &= Cf \int_{U_{th}}^{\infty} U^3 \frac{(U - U_{th})}{\sigma^2} I_0 \left(\frac{U\overline{U}}{\sigma^2} \right) \\ &\quad \times \exp \left[-\frac{1}{2\sigma^2} (U^2 + \overline{U}^2) \right] dU \end{aligned} \tag{3}$$

where U_{th} is the threshold wind speed, $\overline{U}$ is the model predicted wind speed in the center of the cell, I_0 is the modified Bessel function of order zero and σ is the standard deviation of the subgrid fluctuations. We applied the following substitution to make the dust flux integral dimensionless:

$$k = \frac{U}{U_{th}},\ t = \frac{\overline{U}}{U_{th}},\ s = \frac{\sigma}{U_{th}} \tag{4}$$

so we obtained:

$$\begin{aligned} F(U_{th}, t, s) &= CfU_{th}^3 \int_{1}^{\infty} \frac{k^3 (k-1)}{s^2} I_0 \left(\frac{kt}{s^2} \right) \\ &\quad \times \exp \left[-\frac{1}{2s^2} (k^2 + t^2) \right] dk \end{aligned} \tag{5}$$

We integrated over k and varied t parameter from 1 to 10 in increment of 0.1. The values of σ were 0.5, 1.0, 2.0 5.0 and 10.0 m/s and U_{th} were 2, 4, 5.4, 6 and 6.5 m/s. Thus we tabulated the PDF integral so for each t for a given wind speed from the model and a fixed U_{th} , we have pre-calculated the value of the PDF. For cases when t does not have the exact value in the table, a bilinear interpolation was applied to find the corresponding value.

Historically, the Weibull distribution has been used to represent wind speed distributions for application in wind energy studies and size distributions of volcanic ash and mineral dust [*Zobeck et al.,* 1999]. The distribution is written as [*Justus et al.,* 1978]:

$$p(U) = \frac{k}{c}\left(\frac{U}{c}\right)^{k-1} \exp\left[-\left(\frac{U}{c}\right)^{k}\right] \tag{6}$$

where the shape factor k and the scale factor c may be determined directly from the wind data [*Gillette and Passi*, 1988]. In our study we followed the parameterization used in *Grini and Zender* [2004]:

$$k = A\sqrt{\overline{U}},\ c = \overline{U}\left[\Gamma\left(1+\frac{1}{k}\right)\right]^{-1},\ A = 0.94 \tag{7}$$

where Γ is the gamma function. By substituting the shape and scale factors in the PDF, we obtain:

$$\begin{aligned} p(U) &= \frac{A^2}{k}\Gamma\left(1+\frac{1}{k}\right)\left[\frac{UA^2}{k^2}\Gamma\left(1+\frac{1}{k}\right)\right]^{k-1} \\ &\quad \times \exp\left[-\frac{UA^2}{k^2}\Gamma\left(1+\frac{1}{k}\right)\right]^{k} \end{aligned} \tag{8}$$

We used the substitution $U = tU_{th}$ and plugged the PDF in the vertical dust flux equation (2), so we obtained:

$$\begin{aligned} F &= Cf\int_1^\infty U_{th}^4 t^2(t-1)\left(\frac{A^2}{k}\right) \\ &\quad \times\Gamma\left(1+\frac{1}{k}\right)\left[\frac{tU_{th}A^2}{k^2}\Gamma\left(1+\frac{1}{k}\right)\right]^{k-1} \\ &\quad \times \exp\left[-\frac{tU_{th}A^2}{k^2}\Gamma\left(1+\frac{1}{k}\right)\right]^{k} dt \end{aligned} \tag{9}$$

We integrated over t and calculated the integral for the discrete values of k from 1 to 10 with increment of 0.1 and for $U_{th} = 2, 4, 5.4, 6$ and 6.5 m/s. Thus we created a similar look-up table as described in the Bivariate PDF approach.

Figure 6 demonstrates that applying PDFs results in an increase of the modeled wind speed within the model grid box and hence an increase of the predicted vertical dust flux. We calculated total dust mass with the lognormal distribution with several σ (0.5, 1, 2 and 5). As expected, larger subgrid fluctuations lead to higher wind speeds. In our experiment we concluded that $\sigma = 2$ produces dust fluxes closest to the 10 km resolution flux. The Weibull PDF produced slightly higher dust flux due to the fixed scale and shape parameters based on experimental wind data statistics. It has to be pointed out that the relation between k and $\overline{U}$ in Equation 7 is based on the assumption that there is a trend between the k parameter of the Weibull PDF and the mean wind speed [*Justus et al.*, 1978]. This trend is derived from observations of the subtime variability in surface wind speed and is not necessarily the same for subgrid variations.

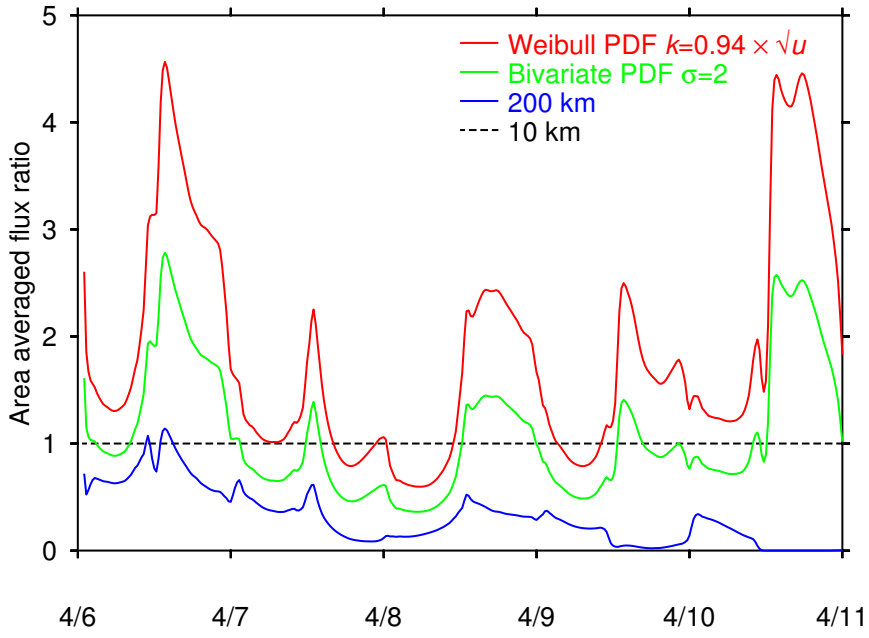

Figure 6: Vertical dust flux for the East Asian domain for spring 2001 at 200 km with no PDF (blue curve) and with bivariate and Weibull PDFs normalized by the 10 km flux.

A reasonable question arises: Can we justify the use of one PDF instead of another? Is it possible to estimate which PDF gives better representation of the natural wind fields? *Cakmur et al.* [2004] argued that the choice of the normal distribution of the PDF neglects higher-order parameters such as skew and kurtosis and the only parameter to be provided is the variance of subgrid fluctuations. The Weibull PDF requires two variables as an input-scale and shape parameters. There are several statistical methods for estimation of these parameters such as the least- squares fit to observed distribution, mean wind speed and standard deviation, or median and quartile wind speed method [*Justus et al.*, 1978] that are based directly on wind data. Lack of systematic wind statistics on various spatiotemporal scales in arid regions makes constraining the PDF parameters particularly challenging. PDF parameters can be explicitly defined in the frame of the global/mesoscale model used for numerical simulations, however adjustments need to be made in the parameters from one model to another or when changing the resolution. As *Cakmur et al.* further pointed out the Weibull PDF can be derived from the normal distribution when resolved speed approaches zero, hence the Weibull PDF can be used in combination with the normal distribution as an empirical fit.

2.4 The effect of the boundary layer physics and dust emission parameterizations on model-predicted dust events

2.4.1 Modeling setup and approach

To investigate the effect of the PBL parameterizations and dust emission schemes on model-predicted dust events we ran the regional dust modeling system with a one-way nesting configuration of MM5. A mother domain (A) and a nested domain (B) for Central and East Asian regions are depicted in Figure 7 and 8, respectively. In domain A, MM5 was driven by NCEP reanalysis data (2.5×2.5 degree resolution at six-hour intervals) to simulate meteorological fields at 50 km horizontal resolution. Modeled outputs were saved every hour. The MM5 model had 23 terrain-following sigma-coordinate vertical levels. Seven levels

were located in the PBL. The meteorological fields, simulated over the coarser domain A, were horizontally interpolated to feed the nested domain B with a grid size of 10 km. An integration time step for the nest was 30 seconds, and the output was saved every 20 minutes. MM5 simulations over the nested domain were initialized with the finer terrain and vegetation/land-use data. The latter was from the U.S. Geological Survey's (USGS) 1-km Advanced Very High Resolution Radiometer derived dataset that is incorporated into the MM5 model. The global USGS 25 category vegetation/land-use data classification was used.

The vertical dust flux predicted with simple dust emission schemes is a function of threshold wind speed U_{10th} (or threshold friction velocity u_{*th}), erodible fraction f, and dimensional constant C (see Table 1). In general, the relationship between the friction velocity and the wind speed at any reference level z depends on the stability of the boundary layer. For the neutral boundary layer, the change of the wind speed with height can be expressed as a logarithmic function [*Stull*, 1988]:

$$U(z) = \frac{u_* \ln(z/z_0)}{k} \tag{10}$$

where k is the von Karman constant, z is the height above the surface, and z_0 is the surface roughness length. The Central and East Asian domains have an average roughness of about 0.1 m for the erodible areas. Therefore, the relationship between U_{10th} and u_{*th} from Eq.(10) is

$$U_{10th} = 11.6 u_{*th} \tag{11}$$

We followed the approach of *Liu and Westphal* [2001] and selected $u_{*th} = 0.6\,\mathrm{m/s}$ that corresponds to $U_{10th} = 7.0\,\mathrm{m/s}$ according to Eq.(11). It is noteworthy to point out that both relating U_{10th} and u_{*th} via Eq.(11) and assuming that they are constant over the considered domain are important simplifications. However, both assumptions are common in studies based on the simple dust schemes [e.g. *Liu and Westphal*, 2001; *Uno et al.*, 2001].

Some studies computed dust fluxes using the U_{10} - driven scheme, but surface winds

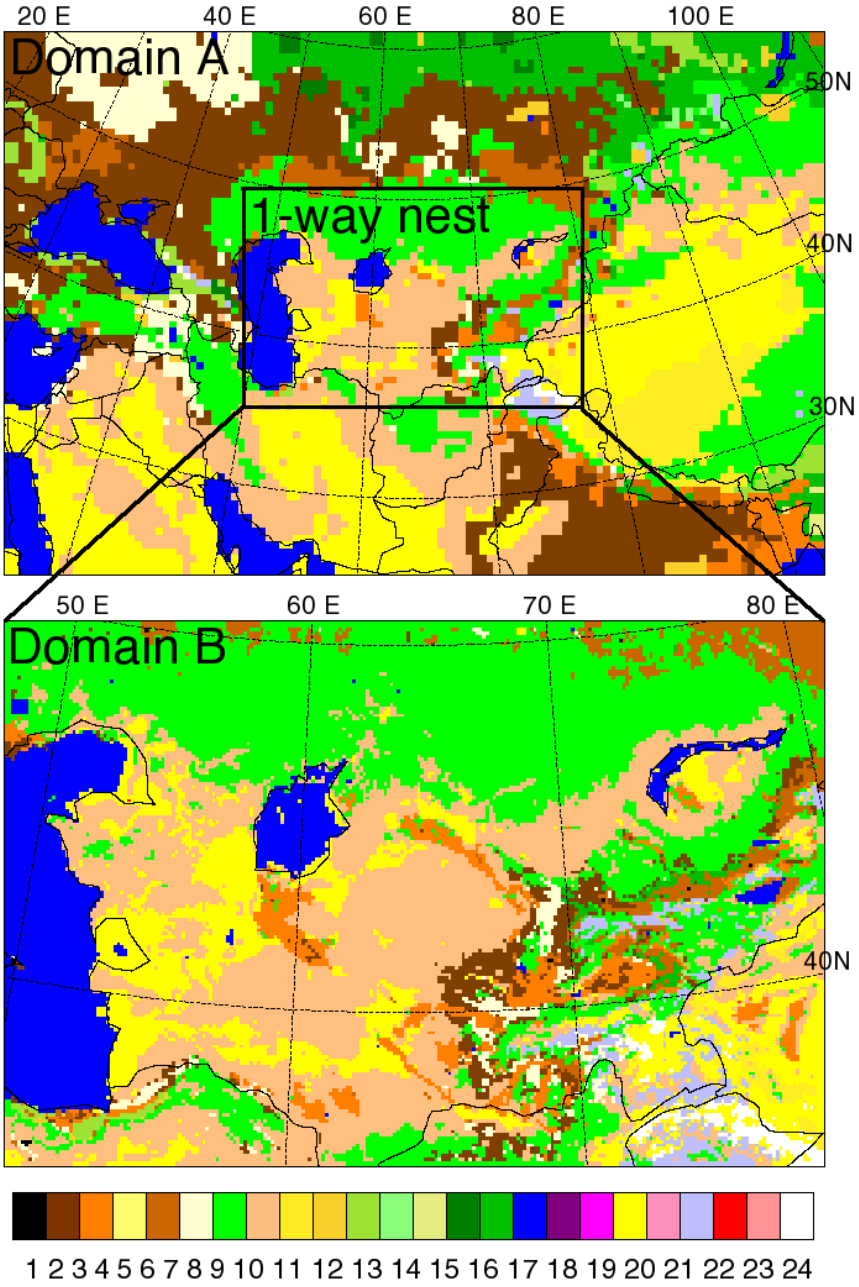

Figure 7: MM5 domain setup for Central Asia: the coarse domain A has a horizontal resolution of 50 km and the nested domain B has a resolution of 10 km. USGS land-use/vegetation categories are as follows: 1-Urban and Built-In Land, 2-Dryland Cropland and Pasture, 3-Irrigated cropland and Pasture, 4-Mixed Dryland/Irrigated Cropland, 5-Cropland/Grassland Mossaic, 6-Cropland/Woodland Mosaic, 7-Grassland, 8-Shrubland, 9-Mixed Shrubland/Grassland, 10-Savanna, 11-Decifuous Broadleaf Forest, 12-Decidious Needleleaf Forest, 13-Evergreen Broadleaf Forest, 14-Evergreen Needleleaf Forest, 15-Mixed Forest, 16-Water Bodies, 17-Herbaceous Wetland, 18-Wooded Wetland, 19-Barren or Sparsely Vegetated, 20-Herbaceous Tundra, 21-Wooded Tundra, 22-Mixed Tundra, 23-Bare Ground Tundra, 24-Snow or Ice.

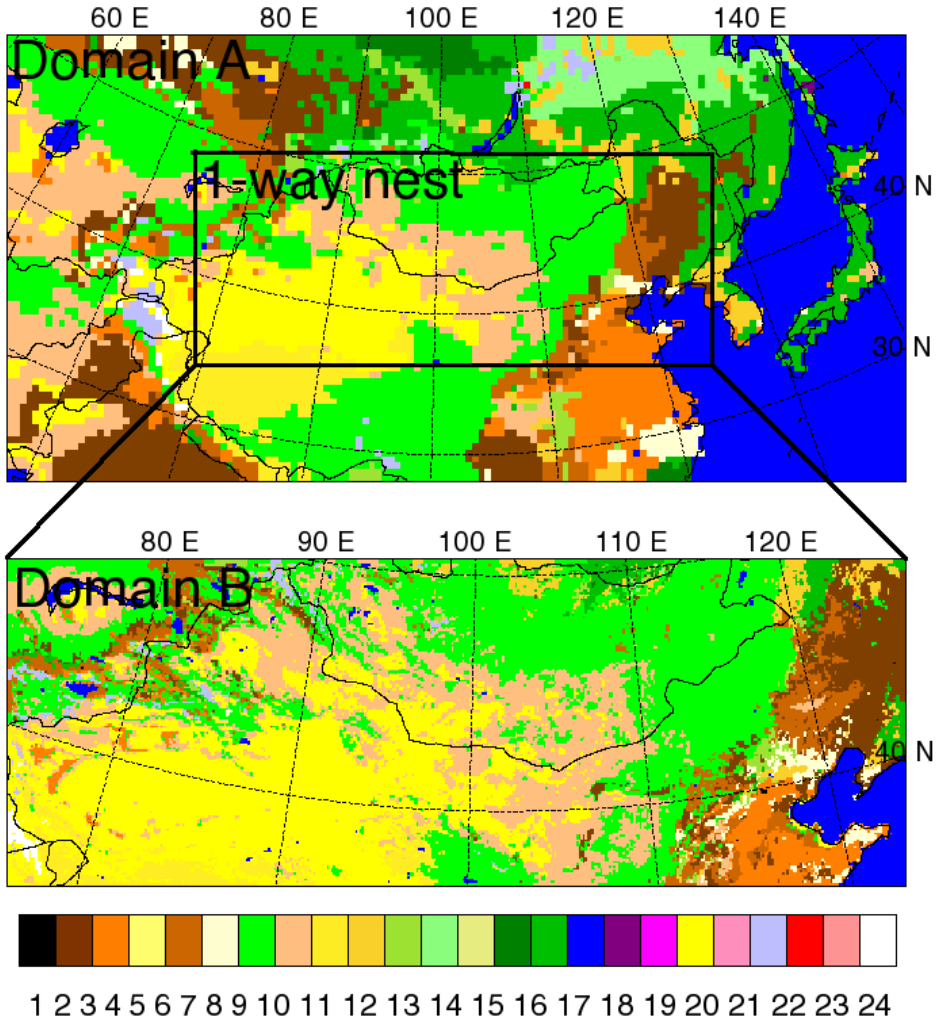

Figure 8: Same as Figure 7 but for East Asia.

were recalculated from the friction velocity using Eq.(10). As pointed out already, the desire to work with surface winds instead of the friction velocity mainly comes from the fact that the former can be directly compared to wind observations. In general, recalculated winds U_{10*} could differ from U_{10} predicted by the meteorological model. To explore how these differences affect the dust emission for considered PBLs, we calculated the U_{10*} - driven dust flux with Eq.(10) using the roughness length and friction velocities from MM5.

Knowing the spatiotemporal distribution of threshold velocity over the simulation domain enables one to accurately assess the timing and intensity of a dust event. This critical dust emission parameter varies greatly in space and time, and it is a complex function of land surface properties (see Section 2.2.2). Parameterization of the threshold velocity is a challenging issue because it exhibits strong regional heterogeneity. To develop an advanced dust emission scheme for Central and East Asia, we adopted the approach of *Draxler et al.* [2001]. In this approach the threshold friction velocity and local friction velocity are calculated by taking into account the increase in roughness due to saltation. The friction velocity and wind speed are related via drag coefficient [*Stull*, 1988]:

$$u_* = \sqrt{C_D} U_{10} \tag{12}$$

The drag coefficient C_D represents sum of two terms - saltating and nonsaltating part [*Gillette et al.*, 1998]:

$$\sqrt{C_{D_S}} = \sqrt{C_{D_{NS}}} + 0.003 \left(1 - \frac{U_{10th}}{U_{10}}\right) \tag{13}$$

The drag coefficient for nonsaltating conditions is:

$$\sqrt{C_{D_{NS}}} = \frac{k}{\ln(z/z_{0NS})} \tag{14}$$

Then for $U_{10} < U_{10th}$: $C_D = C_{D_{NS}}$ and for $U_{10} > U_{10th}$: $C_D = C_{D_S}$. The calculation of the threshold friction velocity follows *Marticorena and Bergametti* [1995]:

$$u_{*th} = \frac{u_{*ths}(D_p)}{f_{eff}} \tag{15}$$

where u_{*ths} is the threshold friction velocity over a smooth surface, D_p is the mean soil particle parameter, and f_{eff} is the efficient friction velocity ratio defined as:

$$f_{eff} = 1 - \left\{ \frac{\ln(z_0/z_{0s})}{\ln\left[0.4(10/z_{0s})\right]} \right\} \tag{16}$$

The roughness length of the soil and the corresponding threshold friction velocity over a smooth surface used in Eq. (15) are $z_{0s} = 4 \times 10^{-6}\,\mathrm{m}$ and $u_{*ths}(D_p) = 0.22\,\mathrm{m/s}$, respectively [*Iversen and White*, 1982].

To compare the dust production schemes listed in Table 1, we calculated the normalized dust fluxes to avoid uncertainties associated with the selection of the constants C. For instance, the instantaneous normalized u_* - driven dust flux, $F_{u_*,norm}$, is calculated as

$$F_{u_*,norm}(t) = \frac{F_{u_*}(t)}{\bar{F}_{u_*}} \tag{17}$$

where $F_{u_*}(t)$ is the instantaneous dust flux computed with a given u_* - driven scheme listed in Table 1, and $\bar{F}_{u_*}$ is the mean flux for the simulated time period defined as follows:

$$\bar{F}_{u_*} = \frac{\sum_{i=1}^{N} F_{u_*}(t_i)}{N} \tag{18}$$

where N is the number of model outputs. Here fluxes are integrals over the erodible part of the domain of interest. The normalized U_{10} - driven dust flux, $F_{U_{10},norm}$, and U_{10*} - driven dust flux, $F_{U_{10*},norm}$, were calculated in a similar fashion. Using normalized fluxes also helps to minimize uncertainties associated with the choice of the erodible fraction f, and thus enables us to better delineate the effects of dynamical (time-dependent) meteorological factors.

2.4.2 The effect of the dust production schemes

Shao [2001] pointed out that it might be difficult to determine whether one dust emission scheme is better that the other and suggested that MB95, O64, and W79 are likely to be equally effective. Here we compare these three schemes by calculating the MB95$-$O64 and W79$-$O64 differences of instantaneous normalized fluxes (denoted as $\Delta\bar{F}_{MB95-O64}$

and $\Delta\bar{F}_{W79-O64}$, respectively). The results for the Central and East Asia for considered PBLs are presented in Figure 9(a, b, c). Instantaneous normalized O64 fluxes are also shown in Figure 9(a, b, c) to facilitate the interpretation of $\Delta\bar{F}_{MB95-O64}$ and $\Delta\bar{F}_{W79-O64}$. All compared fluxes are integrals over the domain B. The O64 flux shows a clear diurnal cycle with the highest values at about 1 PM local time (more exactly, between 12 PM and 2 PM local time) when the PBL has maximum development and surface winds are the strongest. The lowest emission occurs during the nighttime. The considered five-day time period consists of a sequence of strong and weak dust events. For the sake of consistency, here we define a strong (weak) dust event as having instantaneous normalized fluxes higher (lower) than two. For the Central Asian domain most of the dust mass is emitted on 7 and 8 April whereas for the East Asia the days with strongest emission are 6, 7 and 8 April. The presence of dust plumes over the two regions of interest on these days was confirmed with MODIS and SeaWiFs true-color images [*Darmenova et al.*, 2005]. The dust storms dissipated completely on 10 April. Interestingly enough, both dust outbreaks in Central and East Asia almost coincide in time but the synoptic situations resulting in their appearance are quite opposite. In the spring season, formation of dust storms over Central and East Asia is commonly associated with cyclonic cold fronts [*Merrill and Kim*, 2004; *Qian et al.*, 2004; *Warner*, 2004]. This was also the case of the dust storm that occurred over East Asia during 6–10 April 2001. A powerful cyclone located over Mongolia and Northwest China resulted in the so-called "perfect dust storm" responsible for transport of Asian dust over the large distances, as far as the west coast of the U.S. [*Darmenova et al.*, 2005]. At the west edge of the cyclone and in the periphery of an anticyclone centered over the Western Siberian plane, cold arctic air penetrated south due to the strong baric gradient formed over Central Asia. This caused rapid anticyclogenesis, and a powerful anticyclone (central pressure 1050 hPa) was formed with a center located over the Tien Shan Mountains and Taklamakan Desert. As a result, the Central Asian region experienced strong east-northeasterly winds during 7–8 April and dust outbreaks were initiated due to

the intense anticyclonic circulation.

Analyzing Figure 9(a, b, c), one can notice that $\Delta\bar{F}_{MB95-O64}$ and $\Delta\bar{F}_{W79-O64}$ tend to be lower than zero during the time period of strong dust emission (i.e., peaks in O64 fluxes on 6, 7 and 8 April) and larger than zero during weak dust emission. It is also apparent that $\Delta\bar{F}_{MB95-O64}$ differences are larger compared to $\Delta\bar{F}_{W79-O64}$ during the entire period. Relatively small values of $\Delta\bar{F}_{W79-O64}$ indicate that W79 and O64 schemes produce similar normalized dust fluxes. Overall, one can observe in Figure 9(a, b,c) that $\Delta\bar{F}$ values are in the range between -0.18 and 0.05 indicating that the compared schemes would result in up to an 18% discrepancy. However, it is important to keep in mind that the differences in normalized fluxes do not tell us what scheme produces higher fluxes at any given moment in time.

Figure 9(d, e, f) shows the differences between normalized u_*^3 -, u_*^4 -, U_{10*} - driven dust fluxes and the U_{10} - driven dust flux for MRF and BLK PBLs, e.g., $\Delta\bar{F}_{MB95-U_{10}}$, $\Delta\bar{F}_{U_{10*}-U_{10}}$, etc. The instantaneous normalized U_{10} - driven flux is also shown in Figure 9(d, e, f). One can clearly observe a discrepancy of about 50% between these differences for the MRF PBL cases, whereas for BLK in Central Asia the discrepancy reaches almost 100% on 7 April (the day with strongest emission). On this day, almost all $\Delta\bar{F}$ values are negative, except for $\Delta\bar{F}_{GP88-U_{10}}$ which shows high positive values. For the rest of the time, the differences tend to be positive during the daytime and negative during the night. Distinct differences in the behavior of $\Delta\bar{F}_{GP88-U_{10}}$ indicate that predicted dust emission would be more affected by changing the power dependence in the production scheme from three to four rather than by changing the polynomial expression of the u_*^3 - driven schemes (MB95, O64, and W79).

Notice that $\Delta\bar{F}_{U_{10*}-U_{10}}$ follows closely the differences between u_*^3 - driven fluxes and U_{10} - driven flux. This can be expected since U_{10*} was calculated from u_* under the assumption on a neutral boundary layer. The question which therefore arises is how reliable is this assumption for simulations of dust emission. It can be observed in Figure 9(d, e)

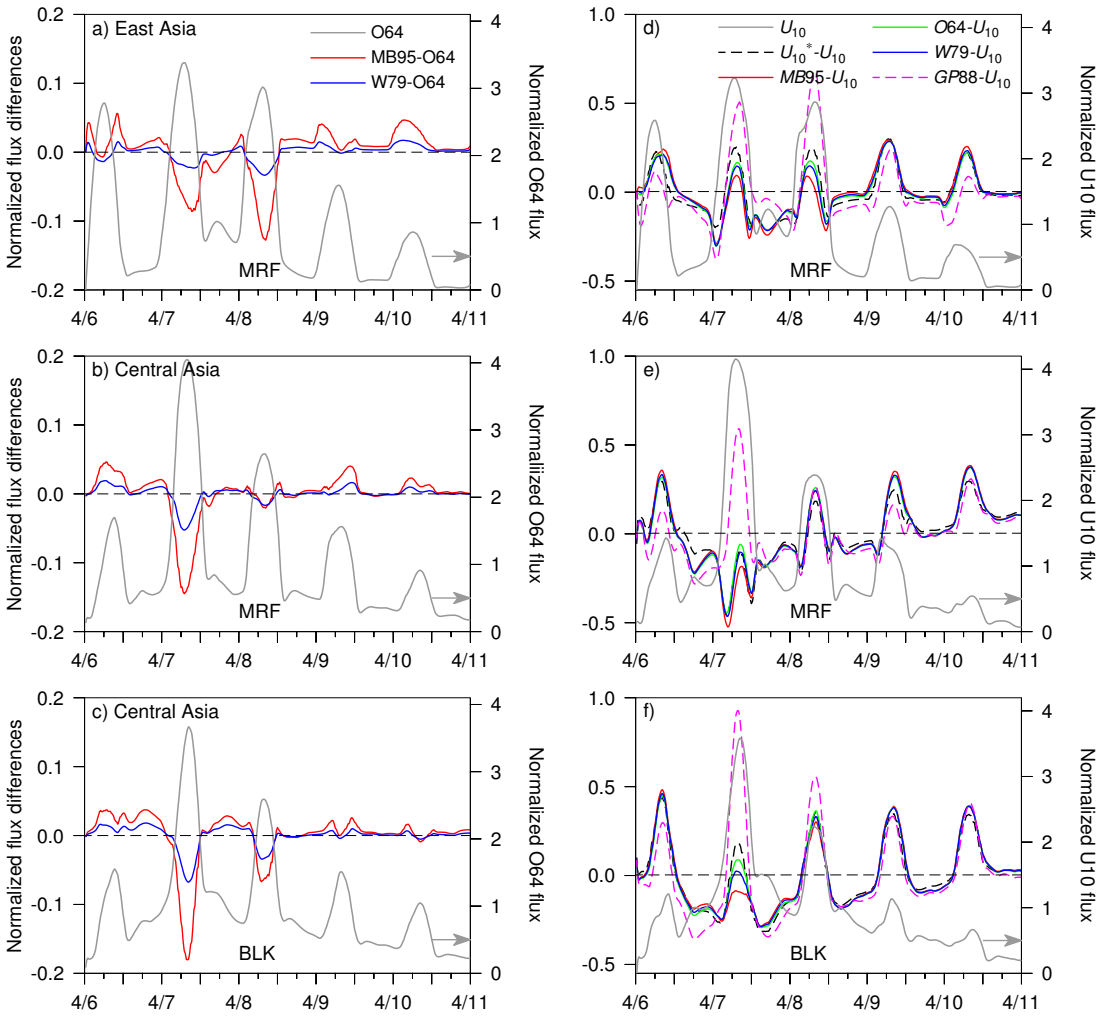

Figure 9: a) Normalized dust flux differences MB95-O64, W79-O64 and normalized O64 flux for East Asia calculated with MRF PBL; b) Same as a), except for Central Asia; c) Same as b), except for BLK PBL; d) Normalized dust flux differences $U_{10*} - U_{10}$, $MB95 - U_{10}$, $O64 - U_{10}$, $W79 - U_{10}$ and $GP88 - U_{10}$ for East Asia calculated with MRF PBL; e) Same as d), except for the Central Asia; f) Same as e), except for BLK PBL.

that during the nighttime $\Delta\bar{F}_{U_{10*}-U_{10}}$ values are closer to zero compared to the daytime values when they can reach up to -0.5. Thus, it seems that the neutral layer assumption might be appropriate during the nighttime for the MRF PBL. However, looking at Figure 9(f) one can notice that $\Delta\bar{F}_{U_{10*}-U_{10}}$ for the BLK PBL have almost the same discrepancies both during the day and the night, though the latter are somewhat smaller. As we already pointed out in section 2.1, the BLK PBL has three regimes in the nocturnal module, which are likely to result in a better representation of the boundary layer during the nighttime. Assuming that BLK produces more realistic behavior of the nocturnal PBL, we conclude that re-calculating the 10 m winds from u_* under the neutral PBL assumption can lead to significant discrepancies in the instantaneous normalized dust fluxes during both day and night. It is also important to point out that U_{10} - and U_{10*} - driven fluxes were calculated using the same threshold speed of 7.0 m/s obtained from Eq. (11). Since this equation is valid for the neutral PBL only, the U_{10th} and U_{10*th} threshold wind speeds could differ in the general case. This may also add to differences between U_{10} - and U_{10*} - driven fluxes.

All discussions presented above are within the scope of the simple dust emission schemes. It is important to determine the differences between the simple and the advanced dust schemes. Figure 10 shows the threshold friction velocities for Central and East Asian domain calculated with Eq. (15). The spatial pattern of the threshold velocity follows closely the behavior of the roughness length as stated by Eq. (16). Figure 10 shows that the threshold friction velocity is rather uniform over the both regions. The reason is that the 25-category USGS land-use classification has the same roughness of 0.10 m prescribed for the bare and sparsely vegetated land, shrubland and grass land. We calculated that the area-averaged threshold velocity for the Central and East Asian domain is 0.86 and 0.85 m/s, respectively.

To compare the uncertainties in the emitted dust mass introduced by the use of a fixed versus variable threshold velocity over the simulation domain, we calculated the vertical dust fluxes with the O64 scheme, originally used in *Draxler et al.* [2001]. The production

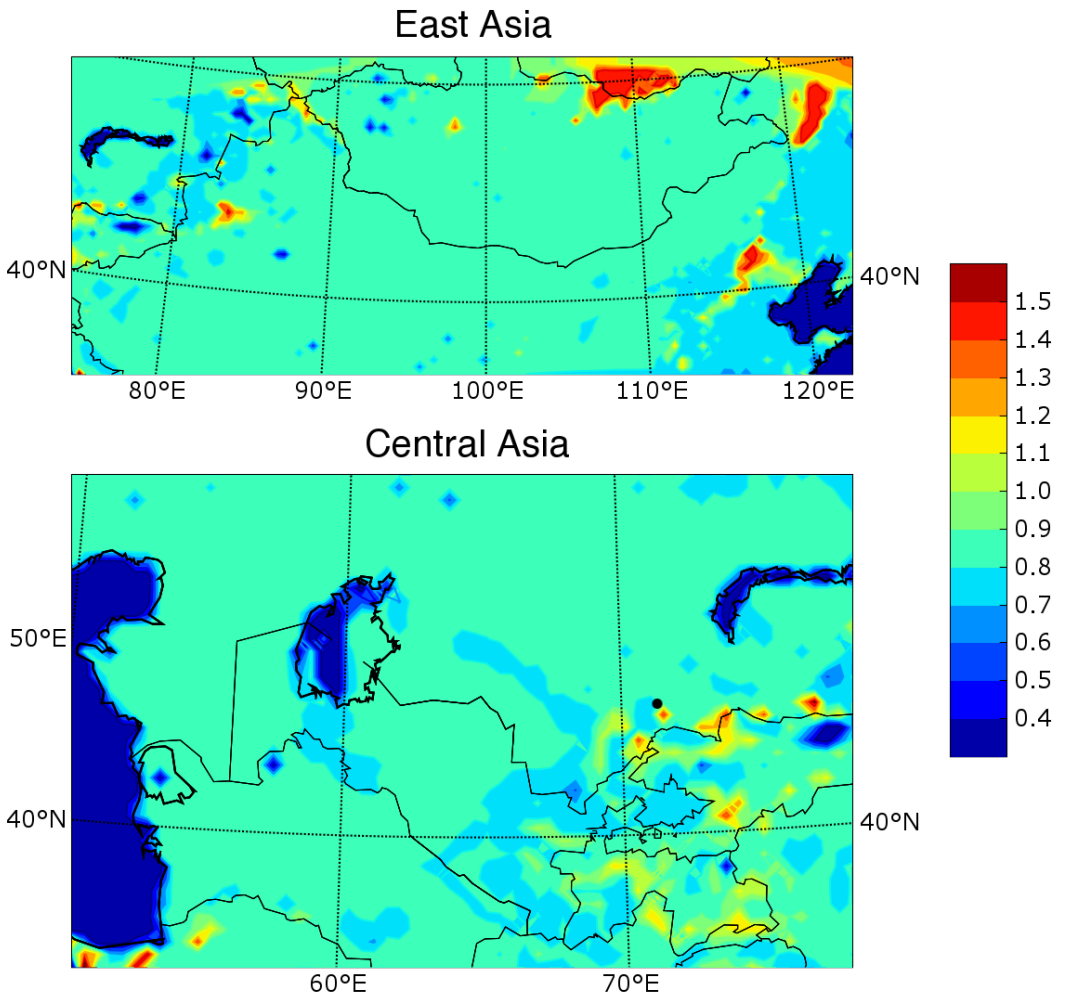

Figure 10: Threshold friction velocity for the East and Central Asian domain.

scheme requires a value of the local friction velocity and the threshold friction velocity for each model cell. Since MM5 has friction velocity readily available (see section 2.2.1) we used it in parallel to the friction velocity derived from *Draxler et al.* [2001] to compare the differences in the simulated dust loads. Thus, we computed vertical dust fluxes using either the local friction velocity calculated with Eq. (12) (the run is denoted as O64(D01)) or by using the MM5 predicted friction velocity adjusted for saltating conditions (Gillette et al. 1998) (denoted as O64(MM5)). The variable threshold friction velocity was calculated following Eq. (15). For the fixed threshold velocity runs, the area averaged values of 0.86 and 0.85 m/s were used for the Central and East Asian domains, respectively.

The normalized flux differences O64(D01)-O64, and O64(MM5)-O64 are shown in Figure 11. The normalized O64 dust flux, calculated with a fixed threshold velocity, is also shown for comparison. It is evident from the plot that O64(D01) - O64 show higher variability compared to O64(MM5)-O64. It also can be seen that normalized flux differences show distinct diurnal patterns being negative during the day and positive during the night during most of the simulation. O64(D01) - O64, and O64(MM5) -O64 tell us how much is the difference between the use of a variable threshold velocity versus a fixed one and the plots show that it can be up to 60%. Discrepancies are higher for the Central Asia, for the East Asia the differences reach only up to 25%. It has to be pointed out that O64(D01) and O64(MM5) differ only by the formulation of the friction velocity, therefore the differences between the blue and red curve on the plot show the discrepancy between the assumption in Eq. (12) and the MRF and BLK approach for calculating the friction velocity (see Section 2.2.1). It would have been interesting to compare real measurements of friction velocities during the simulated period, however such observations are unavailable. Therefore we can only point out the differences without being able to conclude which assumption for calculation of the friction velocity is more realistic.

Another point needs to be raised here. The MM5 roughness map seems to be too crude

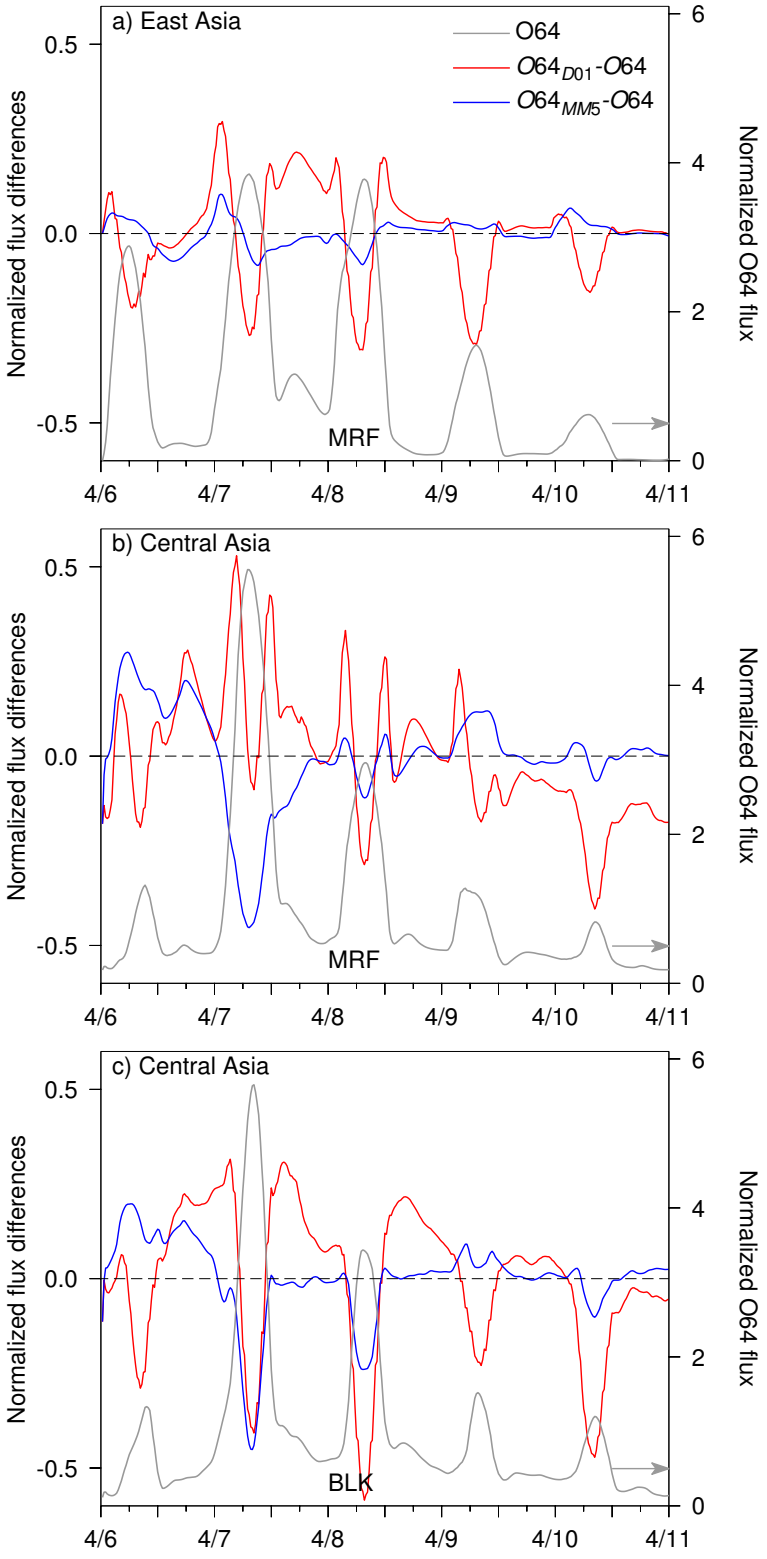

Figure 11: a) Normalized dust flux differences O64(DO1)−O64, O64(MM5)−O64 and normalized O64 flux for East Asia calculated with MRF PBL; b) Same as a), except for Central Asia; c) Same as b), except for BLK PBL.

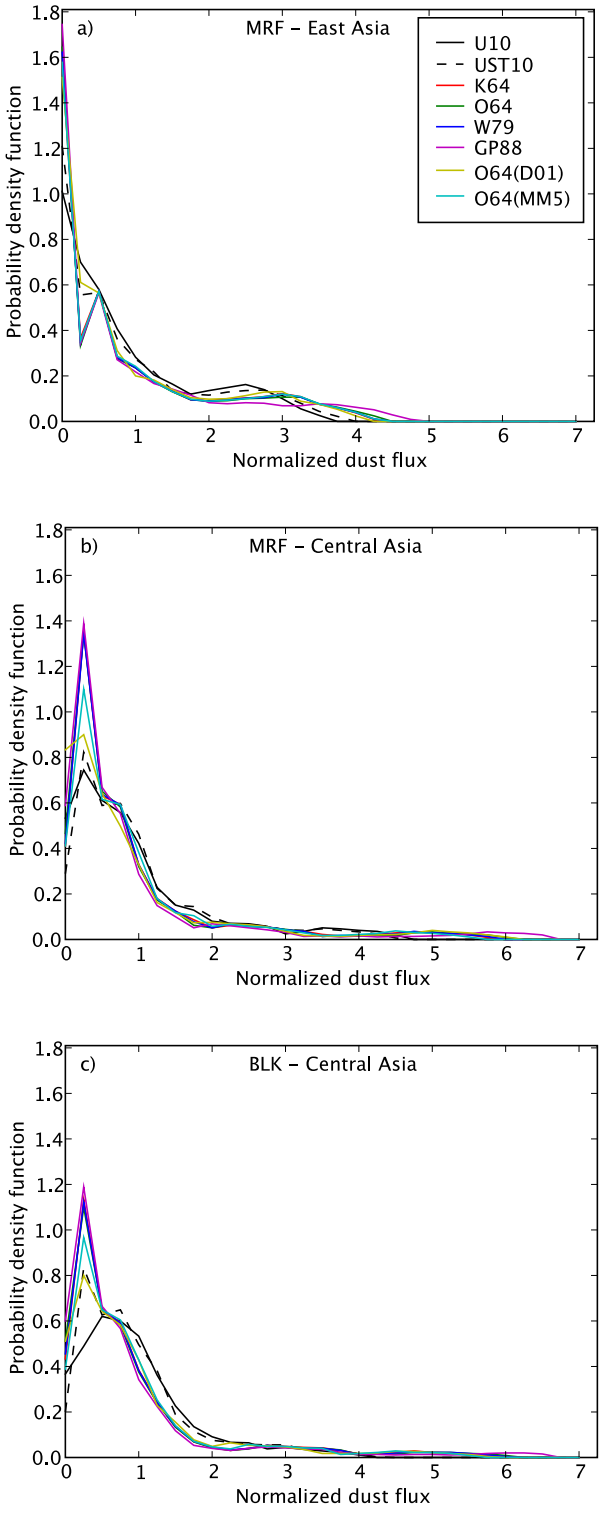

Figure 12: Probability density function of normalized fluxes for the a) East Asia for MRF PBL; b) Central Asia for MRF PBL; c) same but for BLK PBL.

to produce a reliable representation of the land use types in both domains. Only nine roughness classes exist in the 25-category USGS land-use classification, which obviously do not represent well the complexity of the land types and vegetation over the domains of interest. It is evident that surface roughness is a critical parameter for a realistic determination of threshold velocity and a detailed mapping of the roughness length over arid regions is needed. Two studies attempted to perform such mapping based on remote sensing retrievals [*Laurent et al.*, 2005; *Prigent et al.*, 2005], however many technical and scientific issues on how to relate remote sensing measurements to surface characteristics exist. For now this is a wide open and unresolved issue. Development of an advanced dust scheme capable of predicting the threshold friction velocity in the Central and East regions as a function of land surface properties would be required to better constrain the uncertainties of emitted dust mass.

We further explored the differences between the dust schemes by introducing a Probability Density Function (PDF) of normalized dust fluxes. The probability for the normalized dust flux to be in the interval $F_i + \delta F$ is given by:

$$P(F_i, F_i + \delta F) = \int_{F_i}^{F_i+\delta F} f(F)dF \tag{19}$$

where $f(F)$ is the PDF expressed as:

$$f(F_i) = \frac{1}{\delta F}\frac{\delta N}{\sum_i N_i} \tag{20}$$

where i is the number of model outputs for the simulated time period, δF is the bin width, and δN is the number of occurrences of the normalized dust flux within a given bin.

Figure 12(a, b, c) shows PDFs calculated for the normalized dust fluxes, integrated over domain B for the Central and East Asia. The PDF gives the probability for the normalized area-integrated dust fluxes to be in a certain range. The shape of the PDF for both regions indicates that there is a higher probability for the domain to produce weak dust events rather than strong ones during the considered period. The PDF for the East Asia shows high and sharp peak at lower normalized fluxes and a second smaller peak for normalized fluxes

with values between 2 and 3. The presence of a second peak at higher normalized fluxes is an indication for strong emission during the simulated period, although with quite low probability. There are not too many differences between the u_*^3 - and u_*^4 - driven schemes and between the u_*^3 - driven schemes themselves for both regions. However, for Central Asia there is a noticeable difference between the two PBLs. The PDF calculated for the BLK PBL is wider and has lower values. A possible interpretation is that the BLK scheme produces winds than are higher than threshold wind during a longer time period compared to the MRF PBL. This indicates that the choice of the PBL scheme may result in different timing, duration, and intensity of simulated dust events.

2.4.3 The effect of the PBL parameterizations

As we already pointed out above there are several important differences in dust normalized fluxes calculated for the two MM5 PBLs. To further explore this issue, we calculated the relative error of the instantaneous (not normalized) dust fluxes as follows:

$$\frac{F_{i,BLK}(t) - F_{i,MRF}(t)}{\bar{F}_{i,BLK}} \tag{21}$$

where $F_{i,BLK}(t)$ and $F_{i,MRF}(t)$ are the instantaneous dust fluxes calculated with the i^{th} dust emission scheme for the BLK and MRF PBLs, respectively, and $\bar{F}_{i,BLK}$ is the mean flux for the i^{th} dust scheme and the BLK parameterization. The calculated relative errors are shown in Figure 13(a) along with instantaneous normalized O64 fluxes (right axis). Figure 13(b) shows the errors calculated using five-day mean instantaneous fluxes.

Examining Figure 13(a) one can notice that the relative error reaches 143% at the peak of strong dust emission in the case of the GP88 dust scheme. On average the error is about 34%, revealing the significant discrepancy between dust fluxes calculated with the BLK and MRF parameterizations, with the latter being consistently much lower. Figure 13(b) helps to examine the differences in the PBL behavior between day and night. Some differences between the dust schemes are also apparent. The largest error of the U_{10} - driven scheme is around 50% for both day and night. Unlike this scheme, other dust emission

schemes give larger errors during the day than at night. Nevertheless, our results indicated that the discrepancy in dust fluxes between the two PBL parameterizations is much higher compared to the discrepancy associated with the use of different dust production schemes.

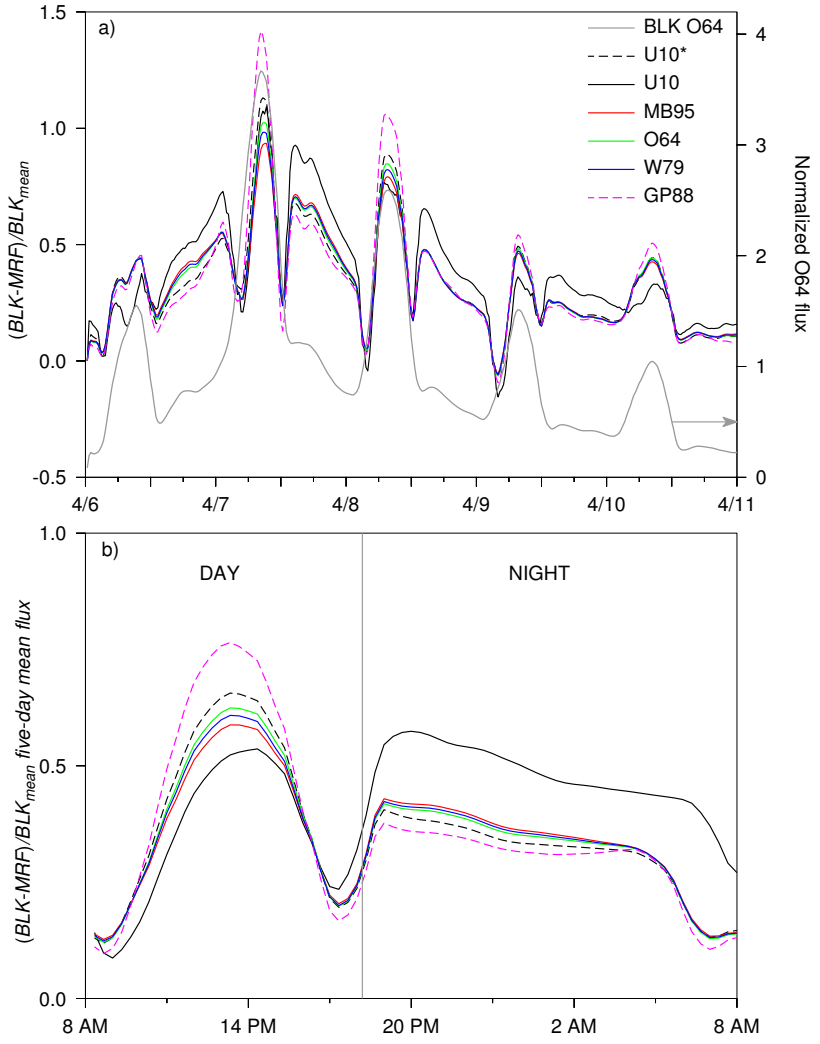

Figure 13: $(BLK - MRF)/BLK_{mean}$ relative errors a) as a function of time, and b) daily averaged for the five-day simulation.

The discrepancy in area-integrated dust fluxes can be caused not only by magnitudes of winds but also by their spatial patterns. To illustrate this, Figure 14 compares U_{10} fields simulated with MRF and BLK for 7 April at 00 UTC. There are many similarities between the two wind fields. For instance, in both cases the highest winds are observed in the central

part of the domain B covering the Aral Sea basin, sparsely vegetated areas in the central part of Turkmenistan, and the southeastern slopes of the Tien Shan. However, BLK results in overall higher winds over the Central Asia region. Noting various differences in the spatial pattern and intensity of the winds in Figure 14, a question arises on which PBL gives the more realistic surface winds. Unfortunately, comparison with observations is severely hampered by the lack of data in the region of interest. For the time period considered here, we were able to find wind observations conducted by only two WMO stations located in the Aral Sea basin: Aralsk (46.783°N, 61.667°E) and Kungrad (43.083°N, 58.933°E). Figure 15(a, b) compares observational data from these stations against U_{10} predicted with MRF and BLK PBLs in the model grid cells containing the stations. It is apparent that both PBL schemes tend to underpredict the surface winds compared to observations, especially in the case of strong winds. This is in agreement with a study by *Dailey and Keller* [2002] who pointed out that the MM5 PBL schemes consistently underestimate the surface winds over areas of strongest winds. Overall, based on the above discussion, one can conclude that the MRF PBL results in a large underestimation of dust emission compared to the BLK PBL regardless of the dust emission scheme, although the largest discrepancy between the PBLs is found for the GP88 and U_{10} - driven schemes. Both MM5 PBLs would likely underpredict the emitted dust mass due to problems in reproducing strong winds.

2.5 Conclusions

A new regional dust modeling system consisting of a terrestrial preprocessor, dust module DuMo and the mesoscale model MM5 was developed. The modeling system operates at a range of scales, has options of flexible nesting, advanced model physics, and incorporates several production schemes with different level of complexity. This chapter presented the results of our study applying this regional modeling system to dust sources in Central and East Asia. In particular, we investigated the capability of the modeling system for predicting the timing, duration and intensity of individual dust events by calculating dust fluxes

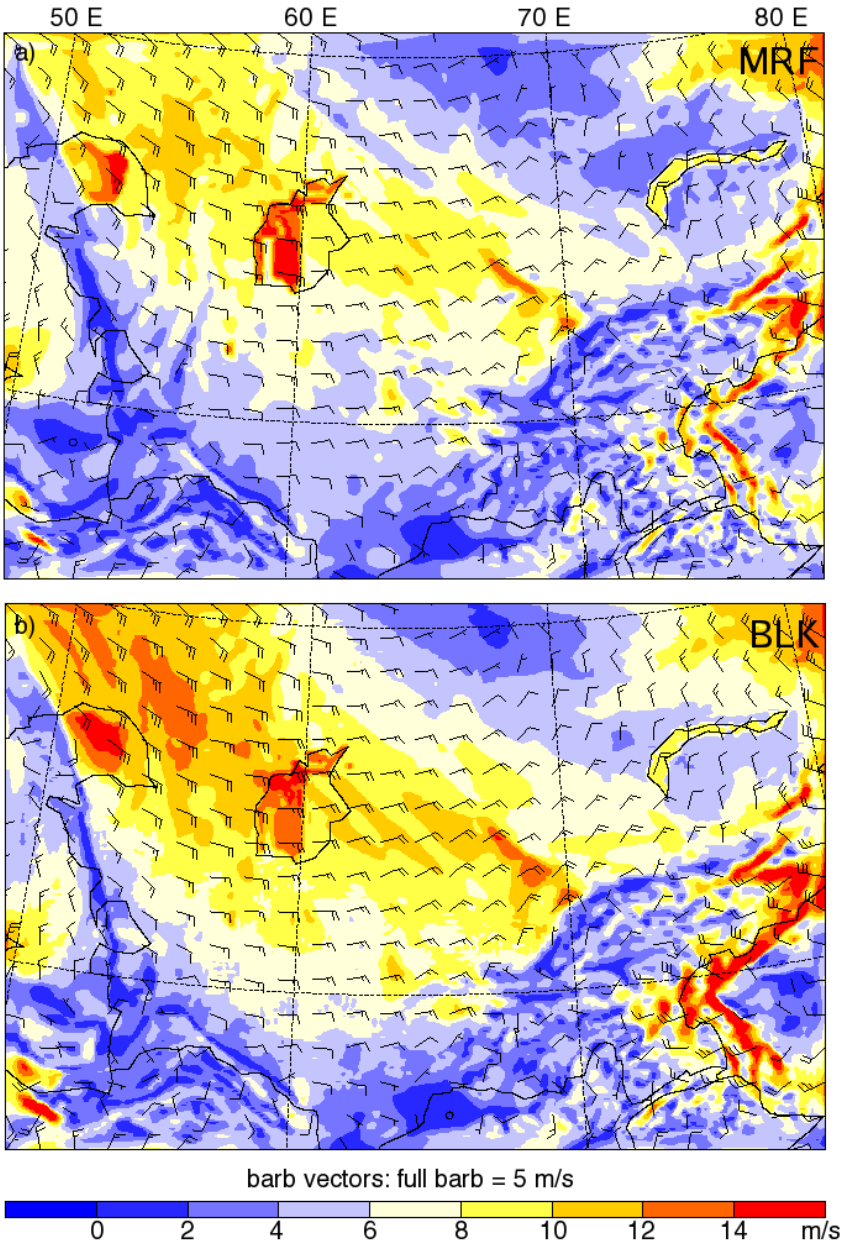

Figure 14: Surface winds at 10 m simulated for 7 April 2001, 00 UTC (5:00 A.M. local time) with a) the MRF PBL scheme, and b) same as a) except with the BLK PBL scheme.

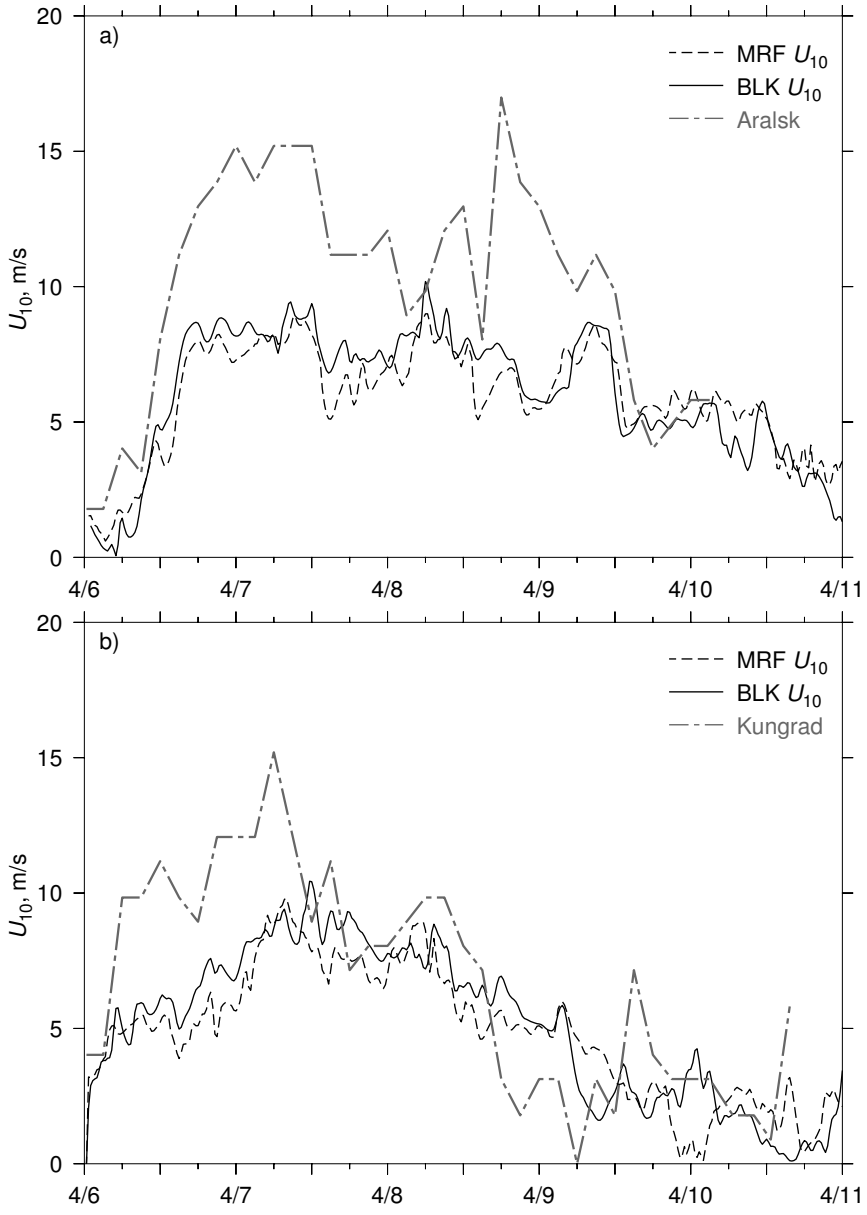

Figure 15: Comparison of the 10 m surface winds simulated with MRF and BLK PBL schemes against observed winds for a) Aralsk and b) Kungrad WMO weather stations.

for different choices of model physics, spatial resolution and dust emission schemes.

A major finding was that the area-integrated dust flux decreases with the increasing grid resolution in both geographical regions considered. Model predicted dust fluxes vary as much as one order of magnitude due to change in the grid resolution. This discrepancy is mainly due to the model resolution-dependent variability of the surface winds and to less extent to variability in the erodible fraction. This result is somewhat expected given the power dependence of vertical dust fluxes on surface winds. Even relatively small changes in surface winds would result in large changes of the dust fluxes. The above findings immediately imply that the coarse resolution of GCMs will lead to underestimating the intensity of model predicted dust events. Furthermore, dust fluxes computed at the 200 km resolution failed to capture weak dust events and as a result, produce wrong timing and duration of dust outbreaks.

On the other hand, we found a relationship between the total fluxes produced at different resolutions. Introducing a correction factor (i.e., a dimensional constant C) will likely allow one to account for the difference in total emitted dust mass across the scales. This finding has an important implication for a sub-grid parameterization of global transport models for improving the simulations of strong and moderate dust events. Moderate-to-weak and weak dust events can be successfully simulated by either introducing the wind PDF to account for the subgrid wind variability or decreasing the threshold wind speed at coarse resolutions. The use of the PDF results in an increase of the instantaneous model predicted dust fluxes, however the magnitude of increase is very sensitive to the selection of a particular PDF and its statistical parameters. One has to be also aware that correcting dust loads at coarse resolutions by decreasing the threshold wind speed for dust emission will adjust only the total dust loads but any changes in their spatiotemporal distribution will stay unaccounted.

We investigated the performance of several simple dust emission schemes, in which the erodible fraction was prescribed based on land cover/land use categories, and the threshold

wind speed was kept constant. We found that the differences between considered u_*^3 - driven schemes themselves are much smaller compared to those found between the u_*^4 - and u_*^3 - driven schemes. Thus, our results indicate that the intensity of model- predicted dust events would be more affected by changing the power dependence in the production scheme from three to four than by changing the polynomial expression of the u_*^3 - driven schemes. In addition, we explored the differences in the model-predicted events due to substitution of the fixed threshold velocity over the entire domain with a variable threshold velocity depending on surface roughness. Significant discrepancies in dust fluxes in Central and East Asia due to different treatments of both local and threshold friction velocity in the advanced schemes were found despite the current limitations of the MM5 roughness map. It is evident, that development of an improved dust scheme capable of predicting the threshold friction velocity in the Central and East regions as a function of land surface properties along with new data set of land surface properties would be required to decrease the uncertainties in the emitted dust mass.

The Probability Density Function (PDF) calculated for instantaneous normalized dust fluxes showed that weak dust emission events were more frequent than strong ones during the considered time period. For a given PBL, different dust emission schemes resulted in very similar PDFs. However, there were differences between PDFs calculated for the MRF and BLK PBLs. In particular, the BLK PBL produced wider PDFs indicating a longer duration of dust emission. This result indicates that the choice of the PBL parameterization can affect the timing and duration of modeled dust events. Furthermore, we demonstrated that the two PBLs produced very different instantaneous dust fluxes. The relative error can be as high as 143% during the strong dust emission, and about 34% on average. Our results showed that the discrepancies in dust fluxes between the two PBL parameterizations are much higher compared to the discrepancy associated with the use of different dust production schemes.

Comparing observed winds from two WMO stations operating in the Aral Sea region,

we found that both MM5 PBLs underestimate the 10 m winds, especially in the case of strong winds. This would result in underprediction of emitted dust mass and incorrect timing and duration of dust events simulated with the MM5 model. This fact stresses the need for further improvement in parameterizations of boundary layer processes in a mesoscale model, especially in desert and semi-desert regions. Given that dust particles strongly affect solar and thermal radiation reaching the surface as well as cause radiative heating or cooling within the interior of the planetary boundary layer, the presence of dust can be an important factor in controlling dynamical and thermodynamical processes in PBL.

Existing differences in the duration and intensity of model-predicted dust events simulated here with one mesoscale model are sufficiently large as to warrant a detailed intercomparison between the mesoscale models used in regional dust modeling. Performing an ensemble simulation with several mesoscale models and/or several PBL schemes can be useful in constraining the range of model-dependent uncertainties in simulated dust events.

CHAPTER III

INTEGRATED SPATIOTEMPORAL CHARACTERIZATION OF EAST ASIAN DUST SOURCES AND OUTBREAKS IN SPRING OF 2001 USING GROUND-BASED AND SATELLITE DATA

3.1 Introduction

One of the outstanding issues in dust studies is the quantification of spatial and temporal variability of the burden and properties of atmospheric dust at all relevant scales [*Darmenova et al.*, 2005]. Regional and global aerosol transport models commonly used for quantification of the dust cycle produce a significant range of uncertainties in the estimated intensity and duration of individual dust outbreaks (see Chapter II). Some of the existing uncertainties can be eliminated when numerical models are validated with observational data. The goal of this chapter is to investigate the potential of observational data, available on a variety of spatiotemporal scales, for providing a reliable constraint for aerosol transport models. In parallel, the extent to which the routine surface observations and satellite data help to characterize the spatiotemporal distribution of dust plumes was examined. A case study presented here focuses on Asian dust in the spring of 2001, addressing the active source regions of mineral dust in China and Mongolia, mid-range transport and trans-Pacific, long-range transport of dust outbreaks on a case-by-case basis. Adequate and consistent characterization of the timing and duration of an individual dust event is central to establishing a reliable climatology, ultimately leading to improved assessments of dust impacts on the environment and climate.

The data sets used in this study include meteorological characteristics and visibility records from 750 weather stations located in China and Mongolia, as well as the images and products provided by several satellite sensors: TOMS (Total Ozone Mapping Spectrometer), MODIS (Moderate Resolution Imaging Spectroradiometer) and SeaWiFS (Sea-viewing Wide Field- of-view Sensor). The NCAR MM5 atmospheric dynamic model driven by NCEP reanalysis data is also employed here in conjunction with observations.

Meteorological parameters (wind speed, precipitation, temperature, etc.) and visibility seem to be the logical candidates for an analysis of the spatiotemporal distribution of dust. These characteristics are routinely reported from numerous weather stations located in China and Mongolia. In addition to land surface properties, meteorological parameters (especially, winds) are the key factors governing the emission and transport of dust, whereas visibility degradation is controlled by the dust loading. A number of previous studies have used meteorological observations to study the dust events in China [e.g. *Zhang et al.*, 2001; *Qian et al.*, 2002; *Xuan and Sokolik*, 2002], but just a few studies have considered both China and Mongolia [*Chen and Chen*, 1987; *Sun et al.*, 2001; *Shao and Wang*, 2003; *Shao et al.*, 2003]. These studies differ in the number of stations included in the analysis, meteorological characteristics considered, as well as in time periods and time-averaging scales. For instance, *Sun et al.* [2001] analyzed wind speed, precipitation and dust storms (defined as dust events with visibility $< 1\,\mathrm{km}$) from 174 Chinese weather stations from 1960 to 1999. Their study reported the spatial distribution of the frequency of dust storms, as well as preferential mid-range transport routes. *Qian et al.* [2002] analyzed dust weather types (including dust haze, blowing sand and dust storms) for the 1954–1998 time period using the data from 338 Chinese stations. They also have used monthly air mean temperature and precipitation from 160 stations and NCAR NCEP reanalysis data of 850-hPa geopotential height and 1000-hPa air temperature with a horizontal resolution of 2.5×2.5 degrees. Despite the fact that overlapping meteorological data sets were used in the above studies, there are various discrepancies in the reported results. *Sun et al.*, and *Qian et al.* both

agreed that the Taklamakan and the Gobi Deserts in northern China and southern Mongolia are the main source regions of dust in East Asia. However, the former study estimated a maximum annual mean number of dust storms of 20 and 40 for the Taklamakan and Inner-Mongolian Gobi, respectively, whereas the latter study reported 35 and 20 dust storms for those regions. There are also noticeable differences in the reported spatial distribution of dust storms (see Figure 2a of *Qian et al.* [2002] and Figure 5 of *Sun et al.* [2001]). Furthermore, there are some discrepancies between the studies that characterized dust outbreaks in spring of 2001. *Gong et al.* [2003] identified four dust events in spring of 2001 associated with low pressure systems, whereas *Gao et al.* [2003] reported 20 dust storms. Here we explore the potential sources of these discrepancies by performing a detailed analysis of the meteorological data for the spring of 2001. Several specific questions are of interest. What is an appropriate definition of a dust event? How much can we actually learn from surface visibility measurements about dust events (e.g., timing and duration)? What other meteorological observations can be used in addition to visibility? Can meteorological data provide any constraints for the dust emission schemes? To what extent can the ground-based meteorological data be used to identify the active source regions and mid-range transport?

The linkage between the individual dust events in the source region and their mid-range transport routes is important because the properties of atmospheric dust and thus its impacts are controlled to a large extent by dust sources. Mid-range transport of East Asian dust has been the focus of a number of previous studies, and several preferential mid-range transport routes of dust in East Asia have been suggested. Based on the 40-year meteorological data, *Sun et al.* [2001] suggested four types of transport routes (called A, B, C and D, see Figure 3 in *Sun et al.*). In contrast, *Zhang et al.* [2003a] defined five general pathways (see Figure 5 in *Zhang et al.*): Northeast, Northerly Mongolian, Northern desert path, Western desert path and Turning path (north to Beijing). The routes B and C in Sun et al. are similar to the Western desert path and Northerly Mongolian path in *Zhang et al.*. Another study by *Chen and Chen* [1987] identified four types of dust storm systems based on the synoptic charts

for ten years: stationary, moving (corresponding to type B in *Sun et al.* [2001]), stationary-moving, and high level transport. However, the latter classification was focused more on the synoptic conditions favorable for dust storm formation rather than on transport routes. Whereas the above studies relied on the ground-based observations only, here we examine the mid-range transport routes of East Asian dust during spring of 2001 by utilizing both surface and satellite observations.

It has been demonstrated that East Asian dust could be transported over the North Pacific reaching the United States and Canada. For instance, a detailed analysis of a single dust outbreak (19–25 April 1998) was conducted by *Husar* [2001] by utilizing several data sets (such as AVHRR aerosol optical depth, IMPROVE network concentration measurements, AERONET sun photometer data, TOMS Aerosol Index, etc.). Recently, *Jaffe et al.* [2003] discussed several other cases of trans-Pacific episodes of dust transport occurring during 1993–2001. In addition to observational evidence, several modeling studies simulated trans-Pacific transport of individual Asian dust outbreaks [*Uno et al.,* 2001; *Takemura et al.,* 2002; *Chin et al.,* 2003]. It would be desirable to relate the number of long-range dust episodes to the number of dust events in the source regions, as well as to understand the conditions favorable for long-range transport of dust. Here we examine the capability of TOMS, MODIS and SeaWiFS observations in tracking the dust plumes and constraining the areas affected by dust transport over the land and oceans. The latter is of particular importance to the number of problems ranging from regional climate radiative forcing of dust to dust iron deposition in the oceans. The important question is: What spatiotemporal resolutions of dust coverage can be achieved with MODIS and TOMS, considering sensor footprints, the time of data acquisition, and cloud contamination? Do dust spatial distributions inferred from independent satellite products agree well enough to provide a reliable constraint for aerosol transport model validations?

The chapter is organized as follows. In section 2 we introduce the data used in this study and procedures utilized for the data analysis. Section 3 deals with the sources and

mid-range transport of East Asian dust, whereas section 4 presents the reconstruction of long-range transport of dust over the Pacific Ocean. Section 5 summarizes our main results and discusses the implications.

3.2 Data Description and Approach

Several data sets in conjunction with the NCAR MM5 meteorological fields were included in our analysis. Figure 16 shows ground-based meteorological data and satellite multi-sensor (MODIS, TOMS and SeaWiFS) products used in this study. All data sets were incorporated into the Asian Dust Databank, which we have been developing over the past years.

Meteorological data for China and Mongolia were provided by the National Meteorological Center of the China Meteorological Administration and the NOAA National Climatic Data Center. The ground-based meteorological stations systematically report several meteorological variables such as visibility, temperature, relative humidity, wind, precipitation, etc., as well as several types of weather occurrences. Overall, the data from 750 stations for the spring of 2001 were analyzed.

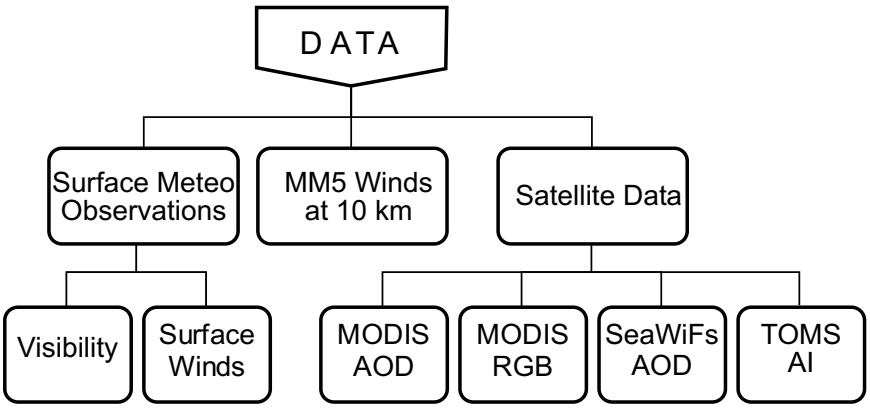

Figure 16: Observational and modeled data used in the study (see text for details).

Several important issues must be addressed in analyzing the meteorological data that may affect the characterization of dust events. The first issue is that the stations have

different frequencies of observations. In addition, not all meteorological parameters are reported sometimes. In March of 2001, 388 Chinese stations reported visibility. Of those, 240 stations measured visibility four times a day, 92 stations reported visibility each hour and 56 stations every three hours. In April, 356 Chinese stations measured visibility every six hours, 56 stations every three hours and 95 stations hourly. In Mongolia, 38 stations reported visibility each three hours during both March and April. Figure 17 shows the location of weather stations whose data were used in our analysis. The stations located in the dust source regions (according to the classification of *Xuan and Sokolik* [2002]) are denoted by triangles and squares, showing different frequencies of visibility observations. The white squares and black triangles denote the Chinese stations having a frequency of visibility observations of one hour and six hours, respectively, whereas the black squares denote the Mongolian stations in the source region measuring visibility every three hours. The black plusses show the stations measuring visibility in China and Mongolia, which are located outside the source regions. Overall, we analyzed the 1464 visibility fields for March and April of 2001. Because of the differences in the frequency of observations and time zones, only visibility fields for 00 UTC, 06 UTC, 12 UTC and 18 UTC include all 750 stations.

Examining Figure 17, one can notice the heterogeneous spatial distribution of the stations. Thus, an interpolation procedure would be required to characterize the spatial pattern of dust events, as well as to provide continuous coverage to facilitate comparisons of ground-based data with transport models and satellite observations. The choice of the interpolation technique does affect interpolated fields in terms of both the spatial distribution and the values of interpolated characteristics. Unfortunately, previous studies, dealing with the analysis of Chinese and Mongolian weather data, rarely discussed interpolation procedures used, with a few exceptions (e.g., *Shao et al.* [2003]). This might introduce various biases in relating the spatial distribution of dust reported by different studies, especially in the dust source regions where the number of weather stations are limited. We tested several

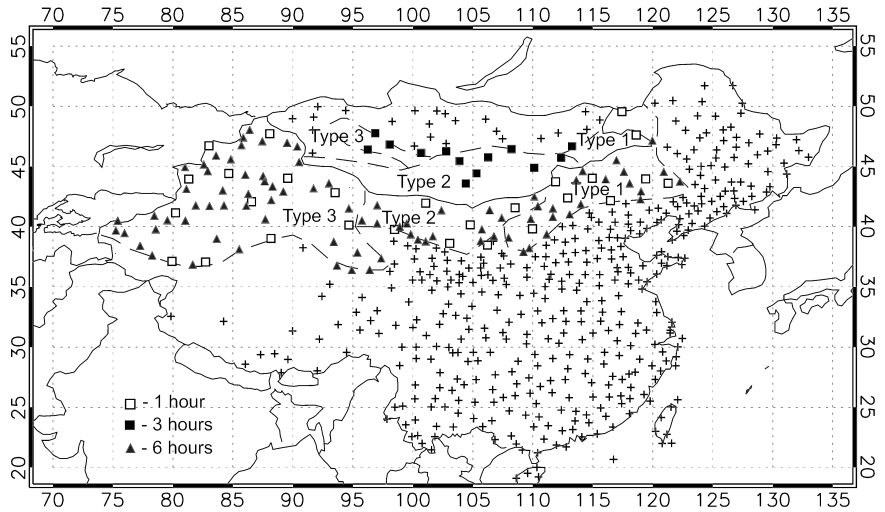

Figure 17: Locations of meteorological stations used in the study. Open squares and black triangles denote Chinese stations in the source regions with a frequency of visibility measurements 1 hour and 6 hours, respectively. Black squares denote Mongolian stations in the source region measuring visibility every 3 hours. Black plusses show the stations measuring visibility in China and Mongolia but located outside the source regions.

interpolation techniques (such as the minimum curvature, nearest neighbor, polynomial regression and Kriging method) and found various differences in interpolated fields produced by different techniques. Based on our analysis, we selected the Kriging method to perform the spatial interpolation of ground-based data (visibility and winds) in this study. The Kriging method is described elsewhere (e.g., *Matheron* [1976]). We believe that differences in the interpolation procedures and in the number of considered stations could be responsible for some discrepancies in the spatial patterns of dust events in China reported by previous studies as discussed above.

Using measured winds and winds modeled with the MM5 model, we attempt to identify the active dust sources and the duration of dust emission (see Section 3.3). The weather stations report winds at the 10 m height. Winds from the Chinese stations are available four times a day, whereas the Mongolian stations report winds eight times a day.

The wind fields were simulated with the NCAR MM5 model over a domain centered

at 44°N and 96°E with a spatial resolution of 10 km. The domain (34.5°–69.9°N)×(51.3°–122.1°E) was selected to cover the dust sources in both China and Mongolia. MM5 runs were initialized by the National Centers for Environmental Predictions (NCEP) reanalysis data with a resolution of 2.5° by 2.5° each six hours. The integration time step was 30 s and the output was saved every 20 minutes for a 120-hour run (see Chapter II for the MM5 setup).

In addition to surface observations and MM5 simulations, we analyzed the data from TOMS, MODIS and SeaWiFS. The Aerosol Index (AI) retrieved from TOMS onboard the Earth Probe (EP) satellite was used to detect dust over both the land and oceans. The EP TOMS AI is retrieved using two channels centered at 0.331 μm and 0.360 μm. These channels are sensitive to aerosols but less sensitive to absorption by gases. The spatial resolution of the EP TOMS sensor is about 40 km at nadir and it decreases with the increasing of the satellite viewing angle (up to 200 km). The current AI product (available at `http://toms.gsfc.nasa.gov/aerosols/aerosols.html`) represents three-day composite images - images use averaged data for one day and data from the two previous days to fill the data gaps [Dr. Hsu, personal communication].

We also analyzed the RGB (red-green-blue channels) images and aerosol optical depth (AOD) at 0.55 μm from the MODIS sensor onboard the Terra satellite. MODIS RGB images are Level-1 data reported as 5-minute granules with the 1 km resolution. The MODIS Aerosol product (MOD04_L2) contains data that have a spatial resolution (pixel size) of 10 km (at nadir). Each MOD04_L2 product file covers a five-minute time interval (based on the start time of each MODIS Level-1B granule). This means that the MOD04_L2 output grid is 10 km (at nadir) in width and 10 km in length for the nine consecutive granules. Each granule has an output grid size of 135 by 204 pixels. To illustrate the MODIS spatial coverage over East Asia, Figure 18 shows the Terra MODIS orbit track as the 5-minute granules with the retrieved aerosol optical depth for 1 April 2001. One can notice that AOD are missing over the large areas that renders the characterization of dust spatial distribution

over the land with MODIS aerosol optical depth data alone highly problematic (see further discussion in section 3.4).

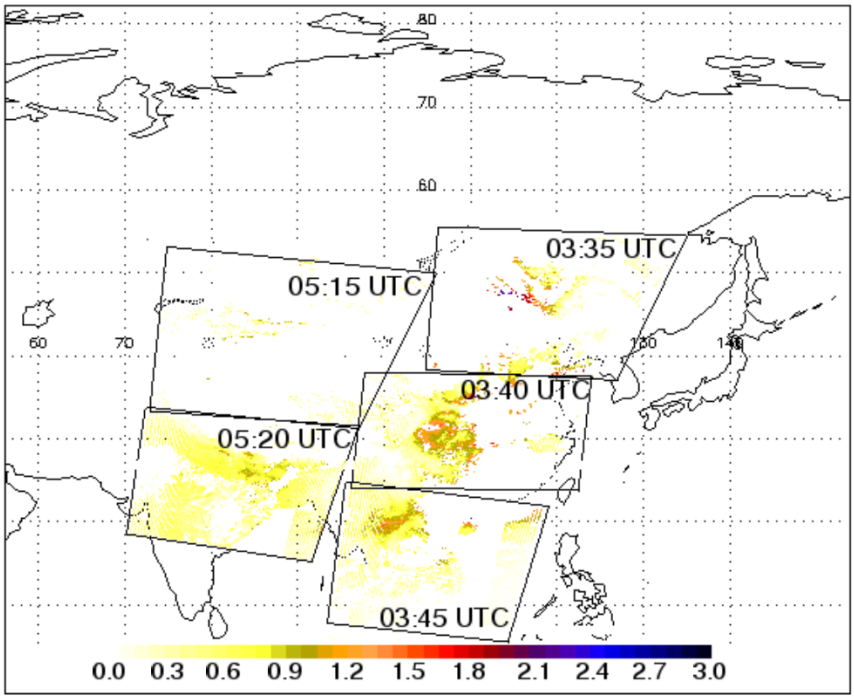

Figure 18: Terra MODIS orbit track over China for 1 April 2001, showing 5-minute AOD granules along the swath.

The daily mean AOD retrieved from MODIS (Level-3 global product MOD08_D3) were also used in our analysis. The daily mean AOD is derived from Level-2 data and averaged in space to a $1° \times 1°$ equal-angle grid that spans a 24-hour (00:00 to 24:00 Greenwich Mean Time) interval.

In addition, aerosol optical depth retrieved from SeaWiFs over the East China Sea by Dr. Christina Hsu (`http://code916.gsfc.nasa.gov/Missions/ACEASIA/satellite/`) was incorporated in the analysis of mid-range transport. These images are made using SeaWiFS Level 1A HRPT Data with a nadir pixel spatial resolution of 1.1 km. More information about the HRPT retrieval and specifications is available at `http://`

seawifs.gsfc.nasa.gov/SEAWIFS/ANNOUNCEMENTS/SeaStar.pdf.
We analyzed 61 images (one per day) corresponding to granules that cover the East coast of China and the neighboring coastal waters.

3.3 Sources and mid-range transport of dust in East Asia

3.3.1 Definitions of a dust event and its duration

Our examination of the previous studies has revealed that existing discrepancies in the reported frequency and duration of dust events could be explained to a large extent by the differences in used definitions. This problem arises because various criteria can be employed to define a dust event. For instance, several different definitions were proposed based on the range of visibility values. *Goudie and Middleton* [1992] define a dust storm as occurring when the visibility decreased below 1 km, whereas the China Meteorological Administration uses the following operational classification: dust haze (visibility $< 10\,\mathrm{km}$), blowing sand (visibility between 1–10 km) and sand storm (visibility $< 1\,\mathrm{km}$). *Shao and Wang* [2003] used four dust weather types reported by meteorological stations following the World Meteorological Organization protocol. However, the dust weather type is determined by different observers and thus prone to subjective errors [*Shao and Wang*, 2003]. In turn, *Prospero et al.* [2002] determined the frequency and sources of dust storms relying on the TOMS Aerosol Index. *Gong et al.* [2003] identified the dust events based on prevailing meteorological conditions associated with dust outbreaks.

For the sake of consistency, here we adopt the following definition: a dust event occurs when two or more stations located in a particular source region report visibility less than or equal to $5\,\mathrm{km}$. Dust events are further subdivided into two types: dust storm (visibility $< 1\,\mathrm{km}$) and blowing dust ($1\,\mathrm{km} <$ visibility $< 5\,\mathrm{km}$). Based on this definition, we use the visibility records from meteorological stations located in potential dust source regions to identify and classify the individual dust events. The visibility data from stations outside of the dust sources were used to constrain mid- range transport (see Section 3.3.3.2). Our

reasoning for using the visibility data for the classification of dust events is that visibility is the only systematic ground-based observation which is readily available and suitable for at least qualitative assessments of the spatial and temporal distribution of dust outbreaks, although various issues must be addressed in the analysis of visibility observations as discussed below. Another advantage is that visibility observations have been carried out by weather stations in China and Mongolia since about 1950 and thus they seem to be appropriate for developing a climatology of the dust events in this region.

Another important issue is how to define the start and the end of a dust event. Several different criteria have been used in the literature. *Chen and Chen* [1987] define a dust storm start when at least three adjacent stations continuously report lithometeors of any intensity for at least three synoptic times (i.e. $> 24\,\mathrm{h}$). The China Meteorological Administration reports blowing dust when five or more stations measure visibility less than 10 km at the same time and a dust storm when three or more stations report visibility less than 1 km. Our classification requires two or more stations to report visibility less than 5 km for blowing dust and 1 km for a dust storm and it is based on statistical analysis of the frequency of visibility values observed by the meteorological stations in the spring of 2001.

It would require some time, from the start of the dust emission process, for dust particles to accumulate in the atmospheric boundary layer resulting in the visibility degradation. This implies that the use of visibility in determining the start time of the dust event might lead to a time delay relative to the beginning of the entrainment of dust. We will further address this issue in section 3.3.2 by analyzing the time series of visibility and winds at selected weather stations and discuss the implications for validation of dust emission schemes.

Some ambiguity exists in defining the duration of a dust event. Following the visibility-based classification, it seems reasonable to define the duration as a time needed for visibility to recover to its background value. But this time can differ between the individual stations because of their location and the frequency of visibility observations. Moreover, visibility

records cannot be used in the case of long-range, trans-Pacific transport because no regular visibility observations are carried out over the oceans. It becomes clear that this term might have a different meaning depending on the application ranging from the duration of a dust event in the source region to the duration of long-range transported dust episodes. Here we use the term “duration” to characterize the interval of time required for the visibility to decrease from 5 km to its minimum value and recover back to 5 km (see further discussion in section 3.3.2.1).

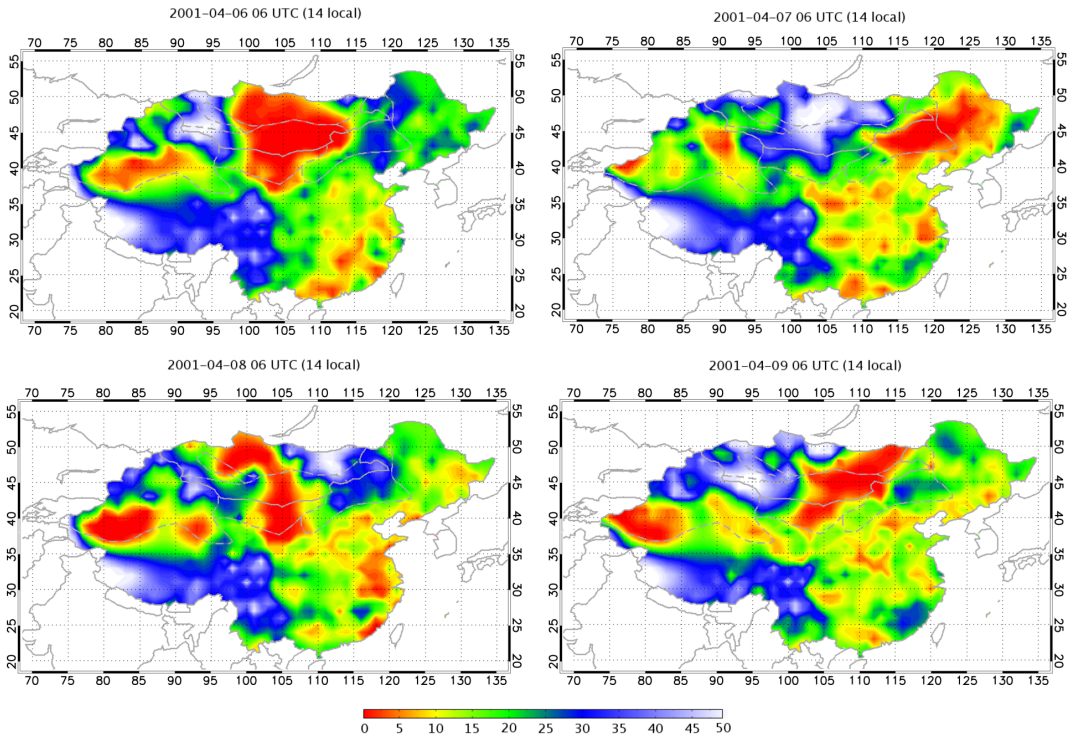

Figure 19: Visibility fields reconstructed for 6, 7, 8 and 9 April 2001 at 06 UTC.

One of the key issues in characterizing the dust events in the active dust source regions is a limited number of the weather stations. Most of the stations in China are located near populated, industrial regions and far from dust production areas. Visibility degradation is often observed over the industrial regions of China (mainly, eastern and southeastern parts of the country). A reasonable question arises on how to discriminate dust from local

pollution episodes. Dust storms in East Asia originate in desert and semi-desert areas having low population density. In those regions a pollution plume hardly can be mistaken with the dust plume since urban and industrial pollution never degrades the visibility lower than 5 km, whereas in all dust events identified in this study visibility was lower than 5 km, and for 60% of the cases below 1 km (see section 3.2.1). However, the reconstruction of the mid-range transport of dust especially over the polluted east and southeast parts of China must be performed with care. To illustrate, Figure 19 shows interpolated visibility fields for 6, 7, 8, and 9 April 2001 at 06 UTC (the time when all stations report visibility). The plots clearly show the degradation of visibility over the Gobi and Taklamakan during the so called "perfect dust storm", which represents two separate dust episodes originating on 6 and 8 April and associated with low pressure systems [*Huebert et al.*, 2003]. Figure 19 also shows that some urban areas in Southeast China could have low visibility (between 8 and 15 km). However, the presence of dense dust plumes can be unmistakably identified because of their large area of coverage and associated lower visibility (0 to 5 km).

3.3.2 Analysis of ground-based data and MM5 simulations

3.3.2.1 Dust events in the source regions

Based on the visibility analysis for the spring of 2001, we concluded that there were five main dust production regions: (A) Taklamakan Desert, (B) Central Chinese Gobi, (C) Central Mongolian Gobi, (D) Eastern Chinese Gobi, and (E) Eastern Mongolian Gobi. Figure 20 shows the number of stations which reported visibility $< 1\,\mathrm{km}$ (heavy black line) and $< 5\,\mathrm{km}$ (light black line) as a function of time in each region. The location of source regions is shown in Figure 21. These regions support the classification proposed by *Xuan and Sokolik* [2002]: Type 1 sources include the deserts in dry- agricultural areas, Type 2 are Gobi-deserts and deserts located on the plateaus, and Type 3 sources are deserts and Gobi-deserts located in topographic lows (see Figure 17).

Figure 20 shows that some dust outbreaks were reported only during one observational

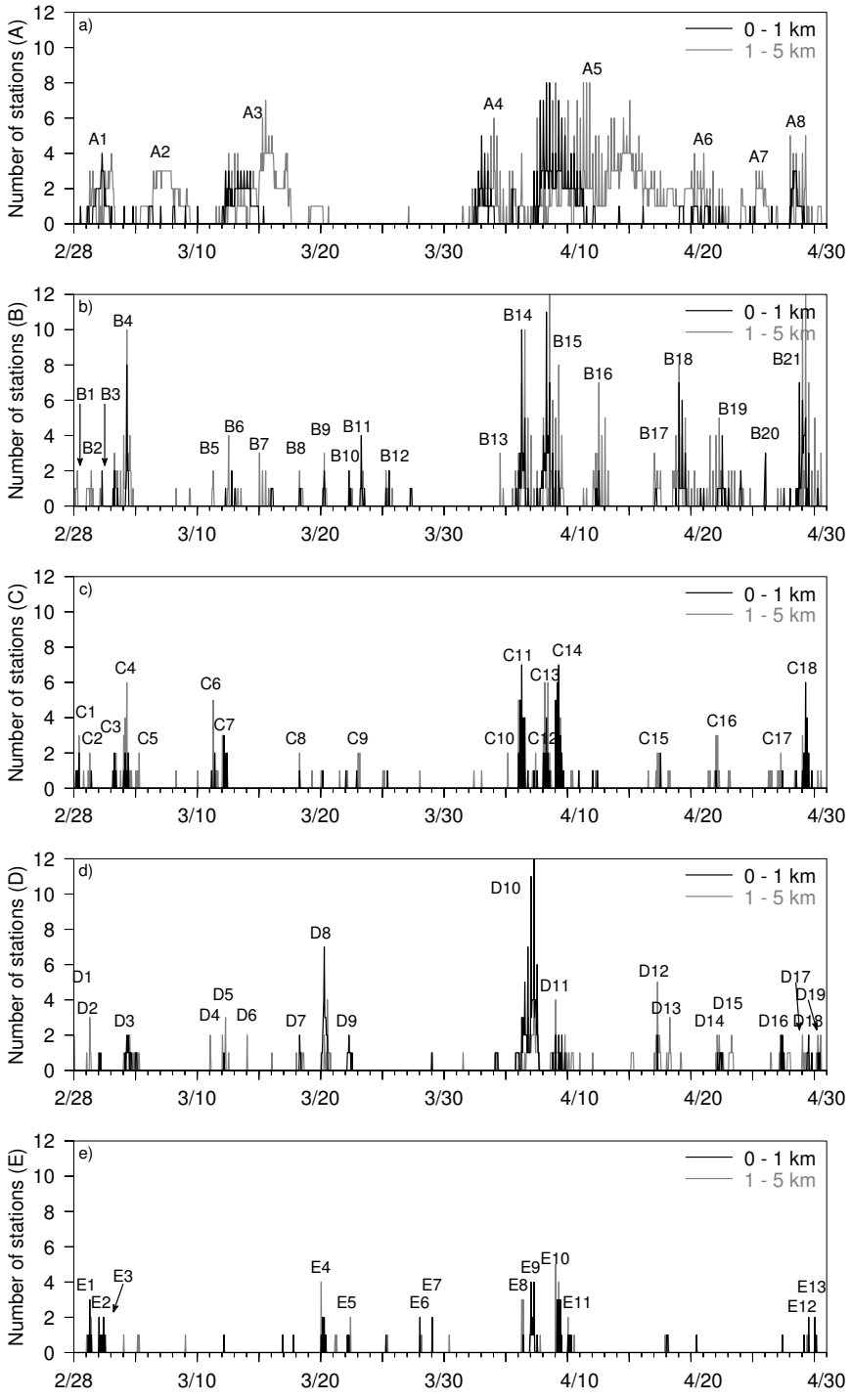

Figure 20: The number of stations reported visibility $< 1\,\mathrm{km}$ (black color) and $< 5\,\mathrm{km}$ (light color) during March and April of 2001 in the A, B, C, D and E source regions. Individual cases in each source region are denoted by letters and numbers.

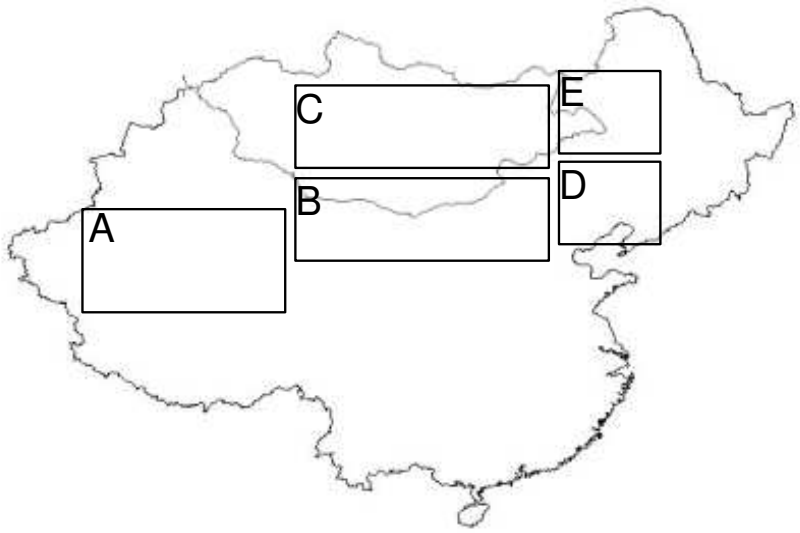

Figure 21: Active dust sources during Spring 2001: (A) Taklamakan Desert, (B) Central Chinese Gobi, (C) Central Mongolian Gobi, (D) Eastern Chinese Gobi, and (E) Eastern Mongolian Gobi.

time. Since our visibility data has different temporal resolution (one hour, three hours and six hours) (see Table 3), we selected the lowest frequency to be an indicator of an occurrence of a dust event (i.e. we selected only these cases that lasted more than six hours). Thus for a dust event to be identified, we required at least two consecutive observations for stations reporting each 6 hours, and 3 or 6 reports for the stations measuring visibility each three hours and one hour, respectively. Thus our complete definition of a dust event in this study is the following: a dust event occurs when two or more stations located in a particular source region report visibility less or equal than 5 km during at least six hours.

Out of all outbreaks shown in Figure 20, Table 4 summarizes only those that lasted more than six consecutive hours. Also shown in Table 4 are the starting date and time, event type (DS-dust storm, BD-blowing dust), duration by the event type, event duration, and mid-range transport routes. In total, 35 dust events were identified for March and April 2001: 8, 10, 7, 7 and 3 in A, B, C, D and E, respectively. Some events consisted of one dust event type (e.g., blowing dust), whereas other consisted of several dust event types (e.g.,

Table 3: Frequency of visibility observations in the source regions.

Source	Total stations	1 hour	3 hours	6 hours
A	37	9	–	28
B	51	10	–	41
C	14	–	14	–
D	31	10	1	20
E	15	3	5	7

blowing dust, dust storm and blowing dust). We found 40 cases of blowing dust and 25 cases of dust storm for the considered regions. Regions A and B showed the highest dust activity. For each dust event, mid-range transport routes were reconstructed by combining visibility and wind fields and constrained against satellite observations as discussed below.

One problem that we encountered while performing the classification of dust events in the source region was the low frequency of observations. For instance, we had just a few stations in the source regions with the frequency of observations of one hour. This renders the determination of the exact start of the dust event problematic. As a result, starting times reported in Table 4 are within an error of at least ± 1 hour. Unfortunately, the measured surface winds also cannot be used for constraining the starting time of a dust event since the frequency of wind measurements is even lower (between three and six hours). The low observational frequency of meteorological data limits their use in validating the dust emission schemes since dust production commonly occurs at shorter time scales.

It is important to point out that the number of the dust events in spring of 2001 identified in this study (see Table 4) differs from those reported by *Shao and Wang* [2003] and *Gong et al.* [2003], mainly because of different definitions used. *Gong et al.* [2003] reported only four major dust storm episodes in spring of 2001 based on synoptic considerations: DS1 (2 March – 6 March), DS2 (21 March – 27 March), DS3 (4 April – 14 April) and DS4 (29 April 29 – 1 May). The problem in using the approach of Gong et al. for dust event classification is that it requires an analysis of synoptic conditions which can be subjective depending on the information used (e.g., meteorological fields predicted by a dynamical

Table 4: Classification of dust events for spring of 2001.

Dust event number	Regional dust event case, see Fig.5	Starting date	Starting time (UTC)	Event type	Duration by type (hours)	Dust event duration (hours)	Mid-range transport route
1	A1	2-Mar	10	BD/DS/BD	8/19/16	43	Local
2	B4	4-Mar	06	BD/DS/BD	23/4/5	32	SE
3	C4	5-Mar	00	BD/DS	3/6	9	E
4	D3	5-Mar	06	DS/BD	4/3	7	E
5	A2	7-Mar	09	BD	53	53	Local
6	C7	13-Mar	00	BD/DS	3/7	10	E
7	D5	13-Mar	00	BD	7	7	E
8	A3	13-Mar	05	DS/BD	50/78	128	E
9	B6	13-Mar	12	BD	6	6	E
10	B7	16-Mar	00	BD	12	12	Local
11	E4	21-Mar	00	BD/DS	3/4	7	E
12	D8	21-Mar	03	DS/BD	10/1	11	E
13	A4	2-Apr	06	BD/DS/BD	6/31/60	97	SE[a]
14	B14	5-Apr	18	BD/DS/BD	6/13/12	31	SE–E
15	C11	6-Apr	00	DS	13	13	SE–E
16	D10	6-Apr	06	DS/BD	32/1	33	SE–E
17	E9	7-Apr	00	DS	7	7	SE–E
18	A5	7-Apr	06	DS/BD	97/174	271	E
19	B15	7-Apr	12	BD/DS/BD	9/34/6	49	SE–E
20	C13	8-Apr	00	DS/BD	10/3	13	E
21	D11	8-Apr	23	DS/BD	19/6	25	E
22	C14	9-Apr	00	DS	13	13	E
23	E10	9-Apr	00	BD/DS	3/7	10	E
24	B16	12-Apr	01	BD	30	30	SE
25	B17	16-Apr	23	BD	14	14	SE
26	D12	17-Apr	03	BD/DS/BD	3/1/4	8	E
27	C15	17-Apr	06	BD	7	7	E
28	B18	18-Apr	12	BD/DS/BD	9/18/6	33	SE
29	A6	19-Apr	11	BD	56	56	E
30	B19	21-Apr	12	BD/DS/BD	24/12/13	49	E
31	A7	25-Apr	06	BD	19	19	Local
32	A8	28-Apr	00	DS/BD	14/18	32	E
33	B21	28-Apr	18	DS/BD	19/24	43	SE–E
34	C18	29-Apr	00	BD/DS	3/10	13	SE–E
35	D18	30-Apr	06	BD	7	7	E

[a]Case identified based on visibility and MODIS RGB images.

model vs. weather forecast based on synoptic observations), as well as the assumptions on how to relate a particular synoptic condition and dust storm occurrence. In turn, the frequency-based approach of *Shao and Wang* [2003] does not allow linking an individual dust event in the source region to its mid- and long-range transport. We believe that the classification of the dust event and its duration proposed in this study overcomes the above limitations, though our approach depends on the number of stations and source regions considered. It becomes clear that a consistent approach for characterizing the dust events that would be widely adopted by the scientific community is urgently needed.

3.3.2.2 Mid-range transport of dust

First, we used the visibility data to reconstruct mid-range transport of the dust outbreaks on the case-by-case-basis. Then the satellite data were examined as to whether they could provide an additional constraint. To illustrate the use of visibility data, Figure 22 shows a mid-range transport route reconstructed for a dust storm originating over the Gobi on 8 April 2001. Visibility measurements for 00 UTC, 06 UTC, 12 UTC and 18 UTC are shown, and regions with visibility less than 1 km are marked by dark gray color, whereas the region with visibility $< 5\,\mathrm{km}$ is shown in light gray color. The evolution and transport of this particular dust plume can be easily observed. The storm that started earlier on 7 April was transported to the southeast-east. Another storm in the Taklamakan started to develop around 06 UTC on the previous day and the plume was transported to the east on 8 April.

Overall, our analysis was performed for 1464 visibility fields in March and April of 2001. Two main transport routes determined for this time period were identified: east and southeast. In the Taklamakan (region A), out of eight dust events, three events were local (i.e., no dust was transported outside of the source region); four were transported to the east, and one to the southeast. Out of 27 events occurred in sources B, C, D and E, 15 were transported eastward, seven events to the southeast and then to the east, four to the

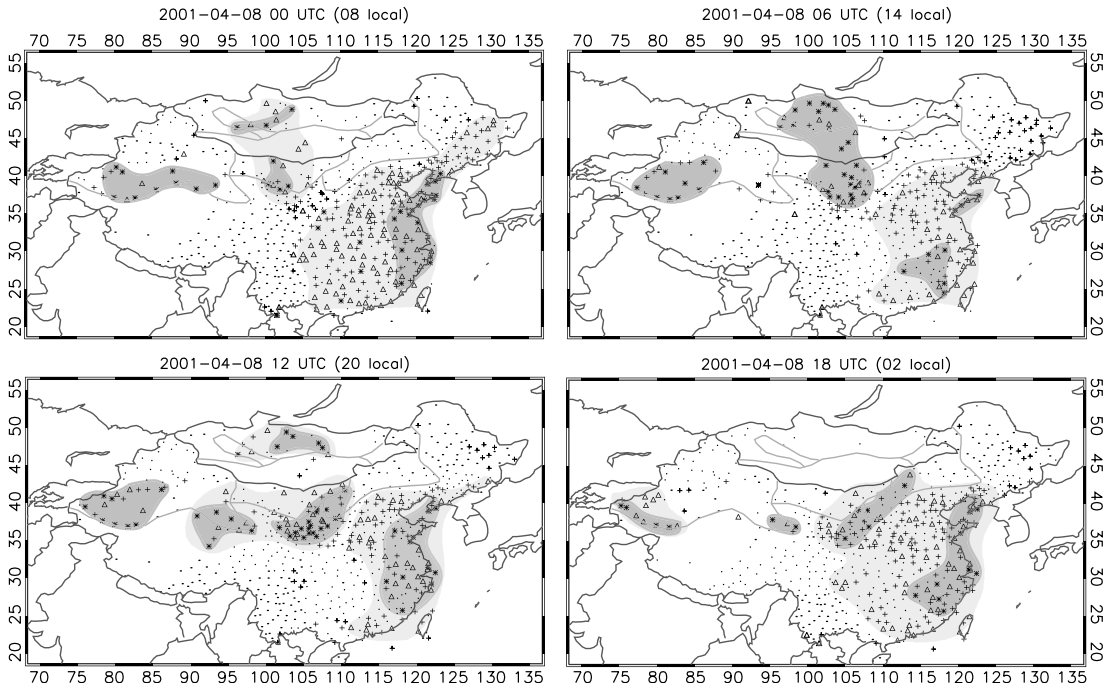

Figure 22: Mid-range transport route of a dust storm originated over the Gobi on 8 April 2001 based on visibility measurements for 00 UTC, 06 UTC, 12 UTC and 18 UTC. Dark gray contours show visibility less than 1 km, whereas light gray contours show visibility less than 5 km.

southeast, and one event was local.

Mid-range transport routes identified here are somewhat different from those reported by *Sun et al.* [2001] They suggested four routes based on the 1960–1999 data: east (through North Korea, case A), east (through South Korea, case B), southeast (case C), and northeast (case D) (see Figure 3 in *Sun et al.*). Our east route is similar to the combined routes A and B in *Sun et al.* We did not distinguish between dust plumes being transported over North or South Korea as separate routes, assuming that there is only one path to the east. Our southeast route out of the Gobi coincides with the southeast path of *Sun et al.* From the visibility data for spring of 2001, we did not find the route D suggested by *Sun et al.* However, examining MODIS RGB images for springs of 2000, 2001, and 2002, we found some indications of the presence of the route D out of the Taklamakan (see further discussion in section 3.3.2.3), as well as several other routes not discussed by *Sun et al.* It is possible

that a limited number of meteorological stations in mountain regions hampers the reconstruction of mid-range transport routes. This implies that *Sun et al.* climatology, based on ground-based data only, could have some biases. On the other hand, large interannual variability in mid-range transport could be the reason for the differences in our and Sun et al. results. Another possible reason is that we included also the blowing dust cases (visibility $< 5\,\mathrm{km}$) in our mid- range transport analysis. Nevertheless, here the MODIS RGB images provided helpful information on transport routes for the considered cases, although reliable discrimination of dust from the surface and clouds on true color images poses a serious problem in using the MODIS RGB data for consistent characterization of dust transport.

3.3.2.3 Analysis of time series of visibility and winds for selected ground- based stations

Our analysis of visibility time series along with observed and modeled winds had a two-fold goal. First, we were interested in finding a time delay between visibility and winds at the starting point of dust events as discussed in section 3.3.2. Second, we wanted to explore in detail the transport pathways (if any) of dust originating in the Taklamakan. Table 5 lists the stations selected for the time series analysis.

To find a time lag between the wind speed and visibility, we examined the data for 6–10 April for four stations located in different source regions: Mongolian station #44347, Hotan, Ejin and Lindong stations (see Table 5). Observed winds were only available for the Mongolian station, so, for the remaining stations, we used MM5 winds simulated at 10 m with a time step of 20 minutes. Figure 23 compares the time series of visibility and winds for the four stations considered. A time lag between the wind and visibility is defined here as the time (if any) required for visibility to start decreasing from its background value after a threshold wind speed (assumed 6 m/s) is reached. Unfortunately, we were unable to find a clear time delay. Our explanation is that one- to three-hour interval in visibility measurements is probably too large to detect the time delay.

Furthermore, we examined the time series of events (marked by the gray areas in Figure

Table 5: Geolocation data for the stations used in this study.

Station	Latitude, deg	Longitude, deg	Elevation, m	Source
# 44347	44.42	105.31	1298	C
Ejin	41.95	101.067	941	C
Lindong	43.967	119.4	486	D
Hotan	37.117	79.917	1275	A
Tikanlik	40.617	87.7	847	A
Ruoqiang	39.017	88.167	889	A
Minfeng	37.067	82.717	1410	A
Lintai	41.767	84.25	978	A

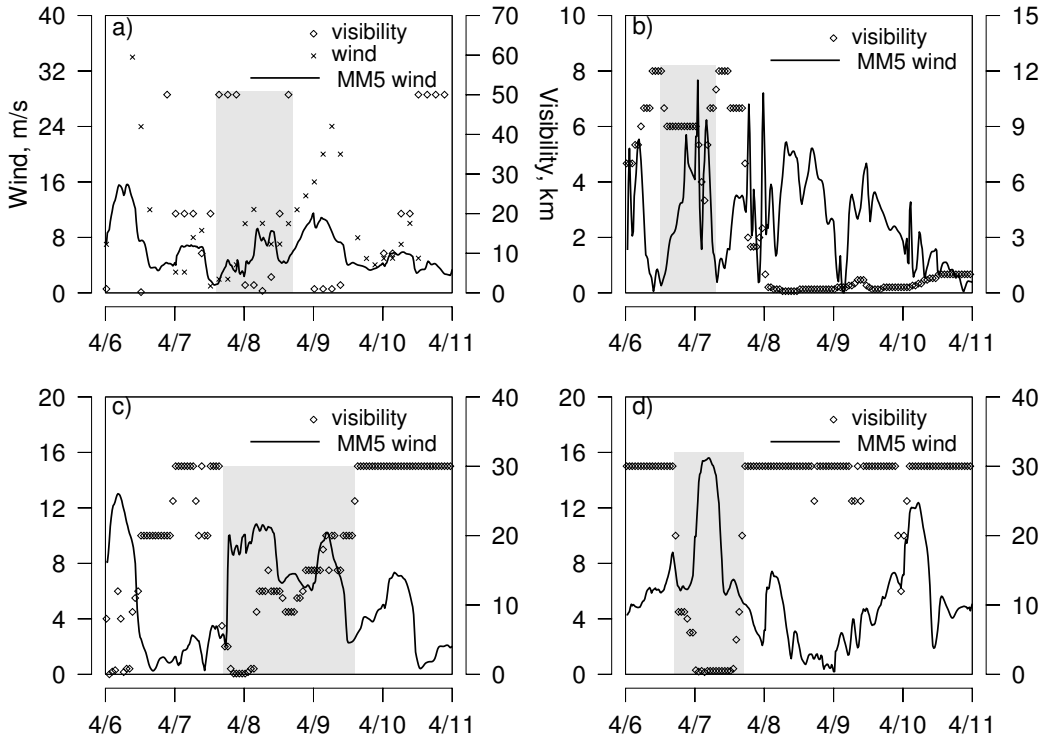

Figure 23: a) Visibility, and measured and simulated winds for Station #44247 in Mongolia, b) visibility and simulated winds for Hotan, c) Ejin, and d) Lindong.

23) to relate the changes in visibility and wind speed. The results are presented in Figure 24. Figure 24a illustrates the schematics of the expected linkage between winds and visibility for the case of strong dust events that would be observed by the stations located in the source region, whereas Figure 24b shows the schematics for a weak dust event. For the strong event case (Figure 24a), visibility shows a hysteresis behavior as a function of wind speed. Initially, visibility does not respond to the increasing wind speed for some time (branch A). When threshold speed is reached, visibility starts to decrease with some delay following a further increase in the wind speed (branch B). After large amounts of dust accumulated in the boundary layer, the further increase of wind does not cause decrease of visibility (branch C). When wind starts to decrease, visibility is still saturated and it takes some time to recover back to its background value (branch D). During the weak dust event (e.g., blowing dust), visibility decreases and then increases without any "saturation". Figures 24c–f show the hysteresis behavior of visibility found for considered individual stations. The distance between the points is one hour for the Chinese stations and three hours for the Mongolian station. According to our classification, dust storms (visibility $<$ $1\,\mathrm{km}$) were observed at Ejin, Lindong and Station #44347, whereas Hotan station reported a blowing dust event (visibility $< 5\,\mathrm{km}$). It has to be pointed out that the hysteresis behavior discussed above is valid for the stations located in the source region so winds measured locally are responsible for the mobilization of dust. For events that originated upwind from the station, the hysteresis curve can change its direction. For such cases it is possible to have decreased visibility before the local winds reaching the threshold value.

Figure 24c agrees well with the schematics outlined in Figure 24a. In turn, Hotan data show a good agreement with the schematics for blowing dust events (Figure 24b). For this case, visibility decreases from 8 km to 4 km and back to 8 km during the three-hour time period. The behavior of visibility at Ejin and the Mongolian station follows the hysteresis curve but in the opposite direction. As discussed above, a possible explanation is that dust did not originate locally but was transported from upwind sources. This is supported

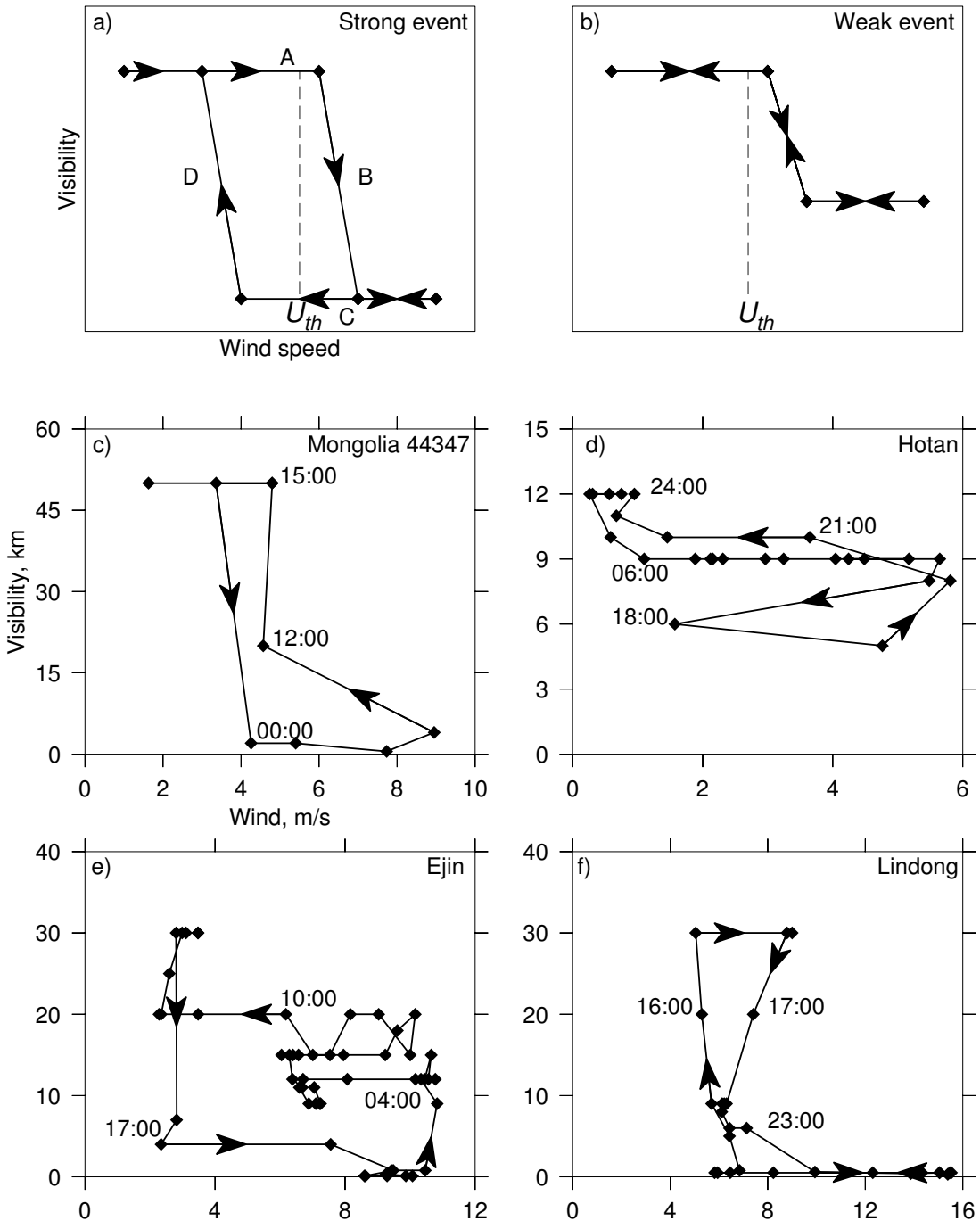

Figure 24: Hysteresis behavior of visibility as a function of wind speed for a) strong dust events, b) weak dust events, c) Lindong, d) Hotan, e) Ejin, and f) Mongolia, #44347.

by the fact that winds were much lower at the beginning of the dust storm compared to the threshold wind required to initiate the dust emission. Thus the initial sharp drop of visibility at Ejin could be caused by transported dust, then long saturation (approximately eight hours) could be a result of both local and transported dust and, then, slow recovery back to background conditions occurred. This finding was confirmed by the analysis of the wind and the visibility time series for the neighboring stations in the source region. From our time series analysis, we conclude that the hysteresis-like behavior of visibility, identified for the stations located in the source region, can be helpful in constraining the emission, boundary layer mixing and deposition schemes used in dust transport models, although care must be exercised in selecting the stations for such an analysis.

Dust transport out of the Taklamakan Desert. Somewhat conflicting results were reported by the previous studies regarding this issue [*Sun et al.*, 2001; *Sun*, 2002; *Iwasaka et al.*, 2003; *Wang et al.*, 2003]. All studies agree that the Tarim basin has a complex topography and hence a complicated surface wind pattern that drives dust emission. Based on a surface wind 1961–1999 climatology, *Wang et al.* [2003] concluded that winds in the western Taklamakan are blowing predominantly from northwest, winds in the eastern Taklamakan are from the east and, in the southern edge of the basin, prevailing winds are from the west and northwest. *Sun et al.* [2001], based on the motion of sand dunes, suggested that surface winds in the basin are mainly easterly/northeasterly. In addition, Sun et al. suggested that since the Taklamakan is surrounded by high mountains, easterly winds cannot easily entrain dust out of the desert. Their later study [*Sun*, 2002] suggested a possible scenario of transport of dust out of the Taklamakan by considering dust accumulation on the southern slope of the Kunlun mountains by surface northeasterlies. *Sun* [2002] also suggested that under specific meteorological conditions dust can be entrained to elevations above 5 km and transported by a westerly jet. The latter was confirmed by lidar measurements reported by *Iwasaka et al.* [2003].

Since the Taklamakan is a productive dust source, it is important to understand how

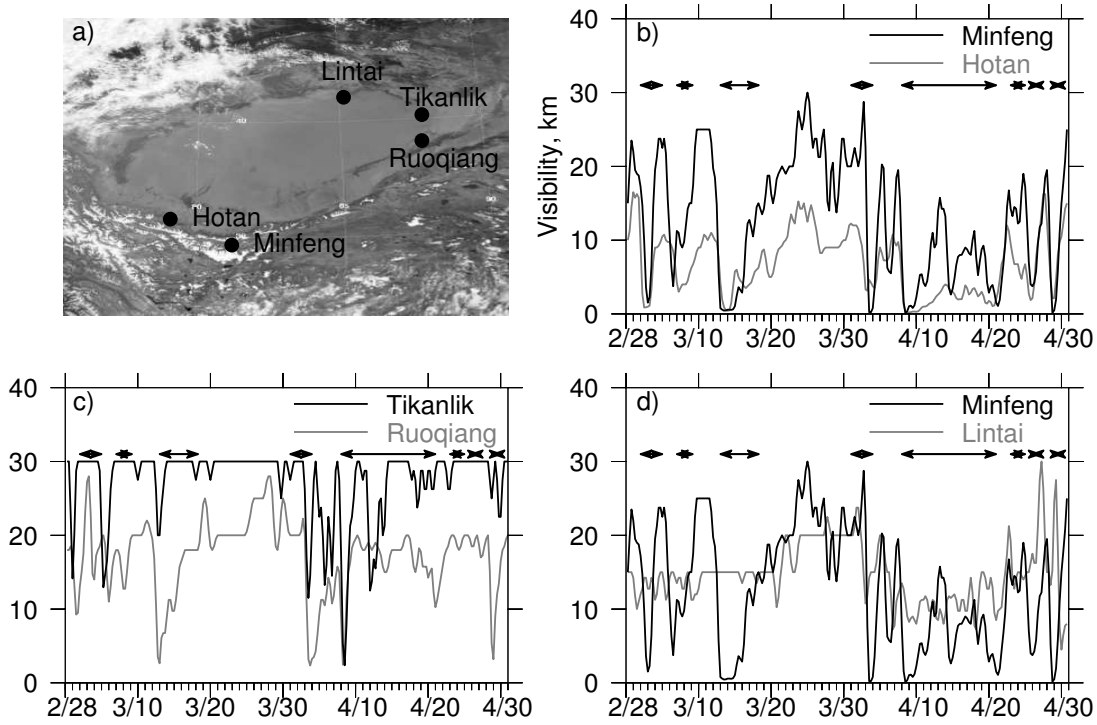

Figure 25: Visibility time series for five Chinese stations located in the Taklamakan Desert. The arrows show the dust events identified over the entire Taklamakan region (region A). (a, b, c, d - explained in the text)

much of this dust actually can be transported outside the Taklamakan Desert, contributing to mid- and long-range transport of East Asian dust. To examine the findings from previous studies, we analyzed the time series from five stations located in the Taklamakan area (see Figure 25a and Table 5). Two stations are located on the Tibetian Plateau (Kunlun Mountains), two are located at the east edge of the desert, and one is located in the desert. Figure 25b–d shows the visibility time series of individual stations for March and April of 2001. The duration of dust events identified over the Taklamakan (region A) are also shown by horizontal arrows on Figure 25. One can notice in Figure 25 that visibility records at these individual stations are somewhat different from the dust events identified based on the visibility data for all 37 stations located in this source region as discussed in section 3.3.2.1.

For Hotan and Minfeng stations (Figure 25b) located on the windward slopes of the Kunlun Mountains (both stations with elevation higher than 1 km), there is a good agreement between the duration of dust events and the degradation of visibility. This confirms the results of *Sun et al.* [2001] that dust originating in the Taklamakan Desert can be lifted to high altitudes (in this case to 1.5 km). On the other hand, Ruoqiang and Tikanlik stations (Figure 25c) located at the east edge of the Taklamakan show overall marginal agreement, showing some response to the dust events but having the visibility minima about a day after the dust event dissipated. Moreover, visibility at those two stations did not decrease below 3–4 km, in contrast to Hotan and Minfeng stations located high on the Tibetian Plateau where each dust event resulted in visibility close to zero. The results suggest that it is very unlikely for dust to be transported near the surface. A possible explanation is that, once mobilized, dust experiences forced lifting caused by the complex topography and, if dust is transported downwind, it has to be above the boundary layer. This is also confirmed by the time series from Minfeng and Lintai stations (Figure 25d). The former station is located on the Tibetian Plateau, whereas the latter one is located in the north part of the desert but at the relatively low altitude (there are no stations in the Taklamakan located lower than 800 m) (Figure 25a). Despite the fact that Lintai is located much lower than Minfeng, the former station did not experience great visibility degradations during dust events in spring 2001.

Our analysis revealed that, out of eight dust events originating in the Taklamakan, three were local, four were transported to the east, and one to the southeast. Of those transported to the east, all were associated with westerly-northwesterly winds. However, as we discussed above, the stations located at the east edge did not show significant response to dust events. Our explanation is that dust was lifted above the boundary layer and then transported downwind to the east. This is also supported by the visibility records at the stations located to the east of the Taklamakan: Magnai (elev. 2947 m) and Chugirty (elev. 924 m) and by MODIS RGB images.

Table 6: Comparison between surface visibility patterns and MODIS RGB imagery.

Visibility data	MODIS RGB Image	Result	Number of Granules	%	Typical conditions
Low ($< 10\,\mathrm{km}$)	Dust	Agreement	67	30	Clouds $\leq 20\%$ not overlapping the plume
Low ($< 10\,\mathrm{km}$)	Dust/clouds	Conditional agreement	66	30	$20\% <$ clouds $< 80\%$, usually overlapping partially the plume
Low ($< 10\,\mathrm{km}$)	Clouds	Cloud contamination	27	12	Clouds $> 80\%$
Low ($< 10\,\mathrm{km}$)	Undetermined	Undetermined	0	0	Undetermined
High ($> 10\,\mathrm{km}$)	Clear	Agreement	41	18	Clouds $\leq 20\%$
High ($> 10\,\mathrm{km}$)	Clear/clouds	Conditional agreement	17	8	$20\% <$ clouds $< 80\%$
High ($> 10\,\mathrm{km}$)	Clouds	Cloud contamination	4	1	Clouds$> 80\%$
High ($> 10\,\mathrm{km}$)	Undetermined	Undetermined	3	1	Undetermined

The single case in spring of 2001 when dust was transported to the southeast seems to be unique. Using the MODIS RGB images for March, April and May of 2000, 2001 and 2002, we searched for other cases of southeast transport of dust from the Taklamakan. The 276 granules (about one per day over the Taklamakan) were analyzed. Our analysis indicated that 31 granules show dust transported to the east of the Taklamakan, five to the northeast, four to the north, four to the northwest, two to the southeast and only one to the south.

In summary, our analysis of visibility data and satellite MODIS RGB images lead us to the conclusion that dust is transported out of the Taklamakan preferably to the east. Since observational data did not indicate decreased visibility at the surface at the east end of the desert in all eight cases of spring 2001, it is likely that dust was lifted above the boundary layer and then transported to the east. Other routes out of the Taklamakan are also possible but seem to be infrequent, strongly depending on the meteorological conditions and complex topography of the region.

3.4 Satellite validation of mid-range transport of dust

Dust plumes can be detected by the satellite sensors operating in the UV, visible or IR spectral regions, though different spectral bands have different capabilities in sensing dust over the land and oceans. Here we examine several satellite aerosol products against the surface visibility measurements in terms of the spatiotemporal pattern of dust transported over East Asia to evaluate the potential of satellite aerosol products in constraining the dust distribution. The aerosol products inferred from satellite data are available at different time scales ranging from instantaneous observations to daily and monthly means, as well as at different spatial resolutions. To provide an adequate comparison, the surface data were interpolated to an appropriate spatial grid and averaged over time to match a particular satellite product. All satellite products used here are derived from polar orbiting satellites. Although geostationary satellites can be also helpful for mid-range transport studies, no

aerosol products retrieved from geostationary satellite sensors over East China are currently available openly to the scientific community.

3.4.1 Multi-day composite satellite product: TOMS Aerosol Index

Although the TOMS AI posted at the TOMS website are referred to as daily mean data, they are actually calculated as a composite of several days (see section 3.2). Nevertheless, we compared the daily mean visibility and the TOMS AI. For each day of March and April of 2001, the daily mean visibility fields were produced and compared to the TOMS AI pattern over the study domain. To illustrate, Figure 26 shows the daily mean visibility and TOMS AI for 6 April 2001. For this particular day, the visibility field shows five areas of decreased visibility numbered from one to five in Figure 26. We compare visibility and TOMS AI fields looking for the similar regional pattern. Areas 1 and 2 coincide on both plots so these two cases are classified as agreement. Area 4 on the visibility map does not have a counterpart on the TOMS AI plot and this is classified as disagreement. Areas 3 and 5 show some of the features seen in the visibility fields but not over the same geographical location. So these two cases are classified as conditional agreement. Based on this approach, we identified 206 cases of low visibility ($< 5\,\mathrm{km}$) in March and April of 2001. Of those, 144 cases were in agreement with TOMS AI (70%), 34 cases were in conditional agreement (16%), and disagreement was in 28 cases (14%). The highest number of disagreements and conditional agreements occurred over northeast and southeast China. The average TOMS AI for these areas is 1.3–1.5, in contrast to 1.5–2 over the dust source regions. Most of the disagreement cases occurred when no dust storm was evident and the low visibility over those regions was likely due to industrial pollution. Since the percentage of agreement cases is relatively high (70%), we concluded that the TOMS AI performed well in detecting dust over the areas with the visibility less than 5 km.

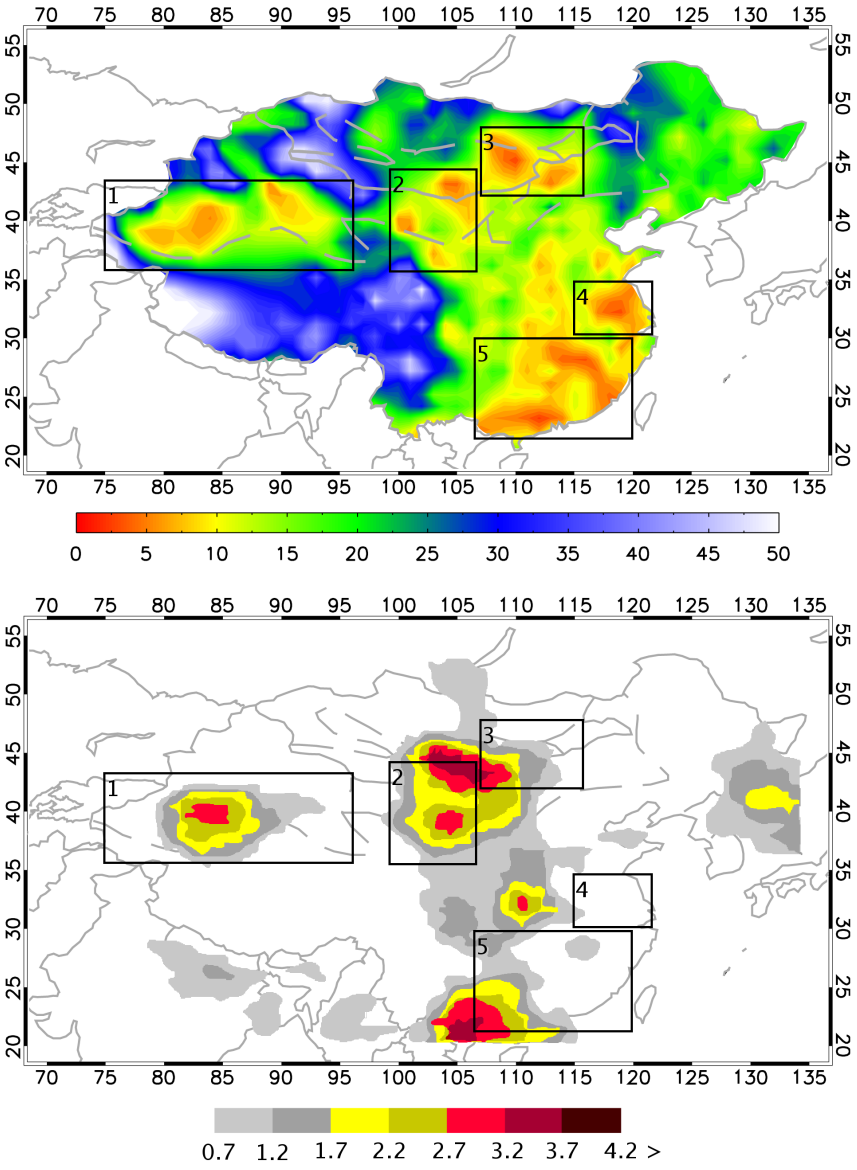

Figure 26: Comparison between daily mean visibility and TOMS AI for 6 April 2001.

3.4.2 Daily mean satellite product: MODIS aerosol optical depth

Following the procedure outlined above, we compared AOD inferred from MODIS against the visibility fields. The spatial patterns in daily mean values of visibility and AOD were examined and the cases of agreement, disagreement and conditional agreement were identified. Out of 206 cases analyzed, 108 cases were in agreement (52%), 51 cases were in disagreement (25%), 42 cases were in conditional agreement (20%), and the AOD data were not available for the remaining 5 cases (2%). Similar to the TOMS AI most of the disagreement cases occurred in southeastern China when no dust storm was present and the low visibility was likely due to urban pollution. We found that the level of agreement for MODIS AOD (52%) was lower than for the TOMS AI (70%). One possible explanation is the difference in the time scales. Multi-days composite products provide a better picture because data from several days are used to fill the gaps in contrast to daily averaged MODIS Level-3 product. However, multiple-day products miss the temporal evolution of dust outbreaks at shorter time scales. Another possible explanation is the problems with AOD retrieved from MODIS over the land as discussed below.

3.4.3 Instantaneous satellite products

We analyzed three different satellite products retrieved from instantaneous observations: MODIS true color images, MODIS AOD over the land, and SeaWiFs AOD over the ocean.

MODIS RGB images. The MODIS true color granules were analyzed using the following approach. China and Mongolia were divided into three large sectors: West (75°E–95°E), Central (95°E–115°E) and East (115°E–135°E). Then, each sector was further subdivided into three subsectors. The areal coverage of each subsector was about the size of a 5-min MODIS granule (see Figure 18). Visibility observations and MODIS granules collocated in time and space were examined to identify the similarities and differences in observed features. The following classification was introduced: agreement, when the image scene agrees with the surface visibility pattern and the cloud coverage is less than 20%,

conditional agreement, when only partial agreement is established due to the presence of clouds (cloud coverage is between 20 and 80%), cloud contamination, when the granule is more than 80% covered by clouds, and undetermined, when we could not decide what phenomena we dealt with (Table 6).

This analysis was performed for each day of March and April 2001 for the time periods when the satellite passes over China and Mongolia (from about 03 UTC to 06 UTC, approximately four granules per day). For different days, the different number of granules was analyzed because the MODIS spatial coverage varies over time. Out of the total 245 MODIS granules analyzed, 48% are in agreement with the surface visibility pattern (the percentage includes agreement in presence of dust and agreement for clear sky scenes). The percentage is smaller compared with the TOMS AI. The reason for low agreement is likely due to the problems in discriminating atmospheric dust from cloud and bright surfaces.

MODIS AOD over the land. Examining MODIS RGB images, we found 67 granules which show the presence of dust over the areas with low visibility. Those granules were further examined for retrieved AOD. Figure 27 shows the distribution of the number of granules versus the percentage of pixels for which AOD was retrieved in each granule. We found that there were no granules with more that 50% retrieved pixels, and the majority of granules had only 10–20% retrieved pixels, though the cloud coverage for the most of those granules was low (about 10–20%). This implies that the cloud contamination is not a main factor here. One possible explanation of poor retrievals of AOD over the land is that the MODIS retrieval algorithm does not account correctly for the spectral surface reflection. This problem has been already pointed out by *Ichoku et al.* [2003]. We conclude that, at this time, MODIS AOD over the land cannot be used as a standalone tool for detecting and characterizing dust. Moreover, the daily mean AOD which are calculated from instantaneous AOD by interpolating them to a larger spatial grid should be used with caution.

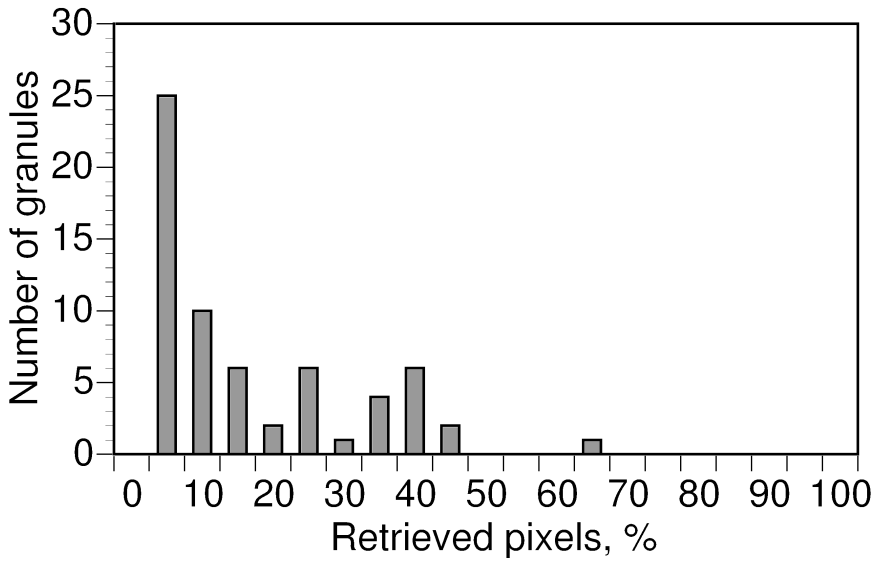

Figure 27: The distribution of the number of granules versus the percentage of pixels for which AOD were retrieved in each granule.

SeaWiFs AOD over the East China Sea. We analyzed 61 SeaWiFs AOD images (one per day) based on SeaWiFs HRPT granules (`http://seawifs.gsfc.nasa.gov/cgi/hrpt_browse.pl`) over the East China Sea. The reason to extend our analysis over the sea was to explore whether SeaWiFS AOD can provide an additional constraint for the mid-range transport routes of dust. The procedure consisted of comparing the aerosol optical depth images along the coast with the visibility measurements at the coastal weather stations at similar observational times. Since we worked with granules retrieved over the East China Sea, we were able to validate only those events that reached the east coast of China, 26 events out of total 35. Another limitation was that we had only one granule per day at a specific time and the percentage of the retrieved pixels was usually less than 50% out of the total area of the granule. As a result, we were able to compare directly only 13 dust events. For eight of them, the SeaWiFs granules showed increased AOD over the coastal waters in the expected locations. Therefore we were able to confirm that the mid-range transport routes for these eight events based on visibility analysis were correct. Despite the fact that some of the granules agreed with the visibility measurements and

confirm the observed transport routes, the results are not very satisfying - the retrieved AOD over the East China Sea was too scattered due to the coverage gaps and probably retrieval problems. In the process of comparing the visibility fields with SeaWiFs AOD, we had a good idea from the visibility fields as to where to look for an increased AOD along the coast. If we lacked the surface measurements, it would have been problematic to do any classification based only on SeaWiFs AOD.

In summary, we used the RGB images from MODIS, TOMS Aerosol Index and AOD from MODIS and SeaWiFs to reconstruct the spatiotemporal distribution of dust at different temporal and spatial scales and constrain it against surface visibility measurements. The procedure was prolonged and detailed (we processed and analyzed approximately 1300 satellite images), but it was valuable for determining the ability of the satellite products to characterize the dust distribution. Because of various limitations of satellite data over the land, we believe that satellite aerosol products should be used in conjunction with surface observations to provide a more reliable characterization of dust distribution over the land, as well as for validation of aerosol transport models.

3.5 Reconstruction of long-range transport of Asian dust plumes

The reconstruction of long-range transport of dust plumes over the Pacific was based solely on satellite data since visibility is rarely reported over the oceans. Two long-range transport dust episodes were identified and their day-by-day transport was independently reconstructed using two different satellite products: TOMS Aerosol Index and MODIS AOD. These products are often used for validation of dust transport simulated with the atmospheric general circulation models. Thus it is important to address the differences and similarities in dust spatiotemporal distribution reconstructed from the TOMS Aerosol Index and MODIS AOD.

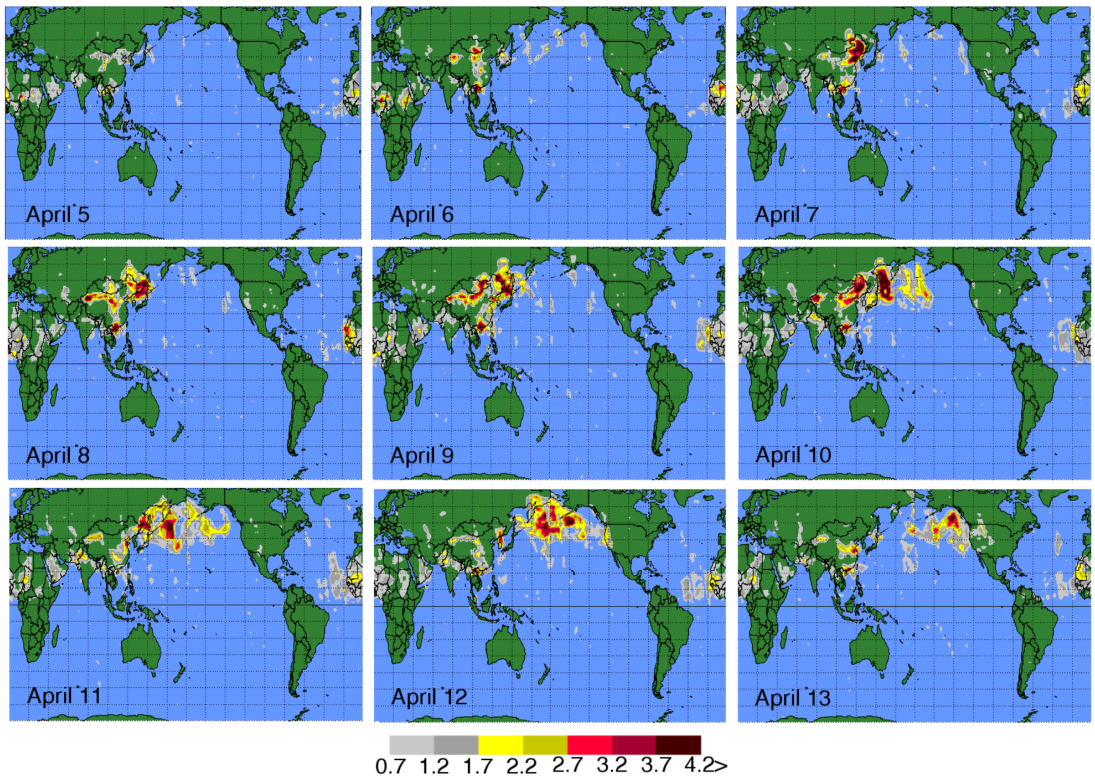

Figure 28: Long-range transport of the dust storms originated over the Gobi Desert on 6 April and 8 April 2001 based on TOMS AI (for AI > 0.7).

Figure 28 shows dust coverage reconstructed from the TOMS AI. The TOMS AI catches the start of the first dust storm on 6 April over the Central Gobi. On 7 April, the plume was transported over northeast China to the east. Later on the same day, another dust event started over the Central Gobi. On 8 April, the first storm reached far northeast China. On 9 April, it was further transported to north Japan and the second one reached the east coast of China. On 10 April, the front edge of the second storm reached the dust plume of the first one. Overlapping of two plumes resulted in the increased TOMS AI over the entire North Pacific (from China to Alaska) on 11 April. On 12 April, the dust plume reached the coast of North America and was detected with lidars and surface measurements in the U.S. and Canada.

In turn, Figure 29 illustrates the reconstruction of dust transport using instantaneous

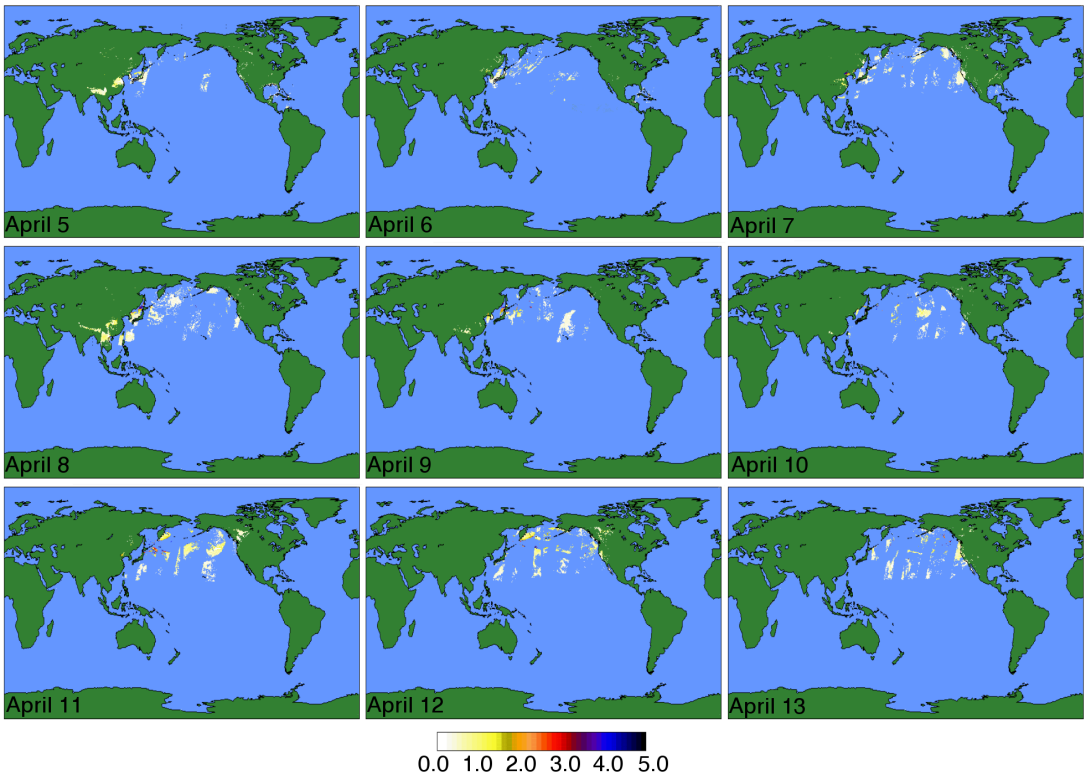

Figure 29: Long-range transport of the dust storms originated over the Gobi Desert on 6 April and 8 April 2001 reconstructed from MODIS AOD. Dust plume contours represent AOD > 0.4.

MODIS AOD higher than 0.4. The structure of the AOD contours is spotty, and the extent of the plume is hard to differentiate. Nevertheless, the MODIS AOD broadly agrees with the TOMS AI. They both capture relatively well the location and the shape of the dust plumes over the ocean. However, MODIS AOD fails to detect the beginning of the dust storms on 6 and 7 April over the source region likely due to the problems in aerosol optical depth retrievals over the land as we discussed above.

Over the ocean, the reconstructed dust coverage differs especially around 9–10 April. There are a few reasons for this discrepancy. One reason is the fact that we use different variables - aerosol optical depth versus aerosol index. As pointed out by previous studies, the relationship between aerosol index and optical depth depends on several factors. For instance, aerosols at low altitudes have lower TOMS Aerosol Index than an equivalent depth

of aerosol at a higher altitude. Another reason for the differences in the dust coverage is the contamination of clouds. Finally, the temporal resolution issue has to be mentioned again. EP TOMS Aerosol Index is a three-day composite, where previous days retrievals are used to fill the missing information for the gaps, whereas instantaneous values of MODIS AOD were used in the analysis. The latter product often has unretrieved pixels over the specific area. Nonetheless, both satellites show a somewhat similar picture in terms of transport and development of the dust plumes. This helps to assess the transport direction and the propagation speed of dust plumes, though the differences can be critical in evaluating the transport model performance.

Based on our analysis, we believe that the dust cases B14–15, C11, D10, E9, and A5 (see Figure 20 and Table 4) are likely contributed to the first long-range transport dust episode, whereas cases C13–14, D11, and E10 contributed to the second one. We were not able to assess the relative contribution of dust originating in the Taklamakan (A5) to the first long- range transport dust episode from the observational data sets used in this study.

Also, we would like to point out that only two dust outbreaks were transported across the Pacific Ocean and reached the North American continent, as far as the Great Lakes region, during March and April 2001. Those episodes were called by the community the "perfect dust storm" [*Huebert et al.*, 2003]. This brings up an interesting question. The year of 2001 is considered to be one of the years with highest dust activity during the last decade. Our study confirms this fact by identifying 35 dust events in the source regions only for two spring months. However, only two long- range transport dust episodes occurred. *Jaffe et al.* [2003] reported one trans-Pacific episode in 1993, one in 1997, two episodes in 1999, and three in 2001, whereas *Husar* [2001] discussed one long-range episode in 1998. A reasonable question is how to adequately assess the adverse impacts of long-range transport of dust over a wide span of time scales ranging from climate studies to air quality problems, if it turns out that inter- continental transport is relatively infrequent (on average, one to two severe dust episodes per two years). It will be important to develop

a climatology of long-range transport of Asian dust by combining satellite observations and aerosol transport models to better constrain the magnitude of dust impacts over the large geographical region. On the other hand, East Asian dust undoubtedly poses a serious regional problem, affecting Mongolia, China, Korea, Taiwan and Japan [*Chun et al.*, 2001; *He et al.*, 2003; *Kim et al.*, 2001].

3.6 Conclusions

Complex spatial and temporal dynamics of atmospheric dust in East Asia renders predictions of dust impacts particularly difficult. In this chapter we utilized several ground-based and satellite data sets to characterize the East Asian dust outbreaks during April–March of 2001, as well as to evaluate the potential of different data sets in dust studies. The main goal was to examine the extent to which the existing routine ground-based observations and satellite data allows us to constrain the spatiotemporal distribution of dust plumes over the land as well as over the oceans at a range of scales.

Our major findings are as follows:

1. We demonstrated that different definitions of the dust event and its duration used by previous studies led to conflicting results regarding the frequency and spatial patterns of dust outbreaks over East Asia. Here we introduced and consistently applied the following definition: a dust event occurs when two or more stations located in a particular source region report visibility less than or equal to $5\,\mathrm{km}$ during at least six hours. Dust events are further subdivided into two types: dust storm (visibility $< 1\,\mathrm{km}$) and blowing dust ($1\,\mathrm{km} <$ visibility $< 5\,\mathrm{km}$). We believe that a consistent approach for characterizing the dust events that would be widely adopted by the scientific community is urgently needed.

2. Five main dust source regions were identified in the spring of 2001: (A) Taklamakan Desert, (B) Central Chinese Gobi, (C) Central Mongolian Gobi, (D) Eastern Chinese

Gobi, and (E) Eastern Mongolian Gobi. The number of dust events identified in A, B, C, D and E were 8, 10, 7, 7, and 3, respectively.

3. Routine visibility observations appeared to be a valuable tool in constraining the regions of origin of dust outbreaks and mid-range transport, though the meteorological data is of limited use for validating the dust emission schemes mainly due to a limited number of stations in dust source regions and low frequency of observations. Visibility measurements can be potentially used to validate the calculated vertical dust fluxes in aerosol models, assuming proportionality between the visibility and the airborne particulate matter. However such relationships depend on the optical properties of mineral dust that show strong regional signature. Thus, constraining model-predicted dust loads is possible on regional level only.

4. It turned out that routine visibility observations are effective in constraining the mid-range transport of atmospheric dust outbreaks over land. Our analysis revealed that the mid-range transport routes were predominantly to the east, with several cases to the southeast-east, and southeast. These are in broad agreement with the climatology of Asian dust mid-range transport reported by *Chen and Chen* [1987] and *Sun et al.* [2001], though some differences exist in transport routes, especially out of the Taklamakan.

5. The source, mid-range transport, and dissipation of all dust events were analyzed using surface and satellite observations. The TOMS Aerosol Index showed the best agreement with the visibility fields. MODIS RGB images were useful when no clouds were present. MODIS and SeaWiFs AOD data showed marginal results in terms of detecting the dust events partly due to the high cloud presence during the studied period. Another reason is a poor performance of the MODIS AOD retrieval algorithm over the land. Even for cloud-free cases, MODIS AOD over the land were retrieved only in 20% of the cases. Because of various limitations of satellite aerosol

products over the land, we believe that satellite aerosol products should be used in conjunction with surface observations to provide a more reliable characterization of dust distribution, as well as for validation of aerosol transport models over the land.

6. Only two long range transport episodes were found during spring of 2001. Long-range transport of these episodes was characterized by utilizing the MODIS aerosol optical depth and TOMS Aerosol Index over the North Pacific Ocean. The day-by-day dust coverage reconstructed from these products show broad agreement, though various differences were observed that might be critical in evaluating the aerosol transport models. The existing problems in discrimination between dust and clouds in MODIS observations over the ocean could be an important factor [*Darmenov and Sokolik*, 2005].

Our analysis of satellite datasets at different spatial and temporal scales showed that remote sensing observations have high potential in dust studies, especially over the oceans where surface observations are rare. Satellite data provides systematic measurements on a regional and global level that makes it a perfect tool for validation of aerosol transport models. Despite the obvious advantages of remote sensing retrievals, many unresolved problems still exist. One major issue is the lack of dedicated dust products that will enable better estimates of the complex spatiotemporal dust distribution. Current aerosol products rarely take into consideration dust properties in their retrieval algorithms, hence the existing products have deficiencies in representing dust aerosols. Another problem stems from the large discrepancies in the retrievals of the same aerosol products from different instruments. Thus, using a particular aerosol product to validate transport models will produce a bias in the estimation of the distribution of dust loads. In addition, the high spatiotemporal intermittency of instantaneous satellite datasets that are especially helpful for validation of individual dust outbreaks makes them of limited use for constraining model simulations. Merging surface measurements and satellite data over the land seems to be a promising strategy for the study of dust events that enables, at least to some extent, to overcome

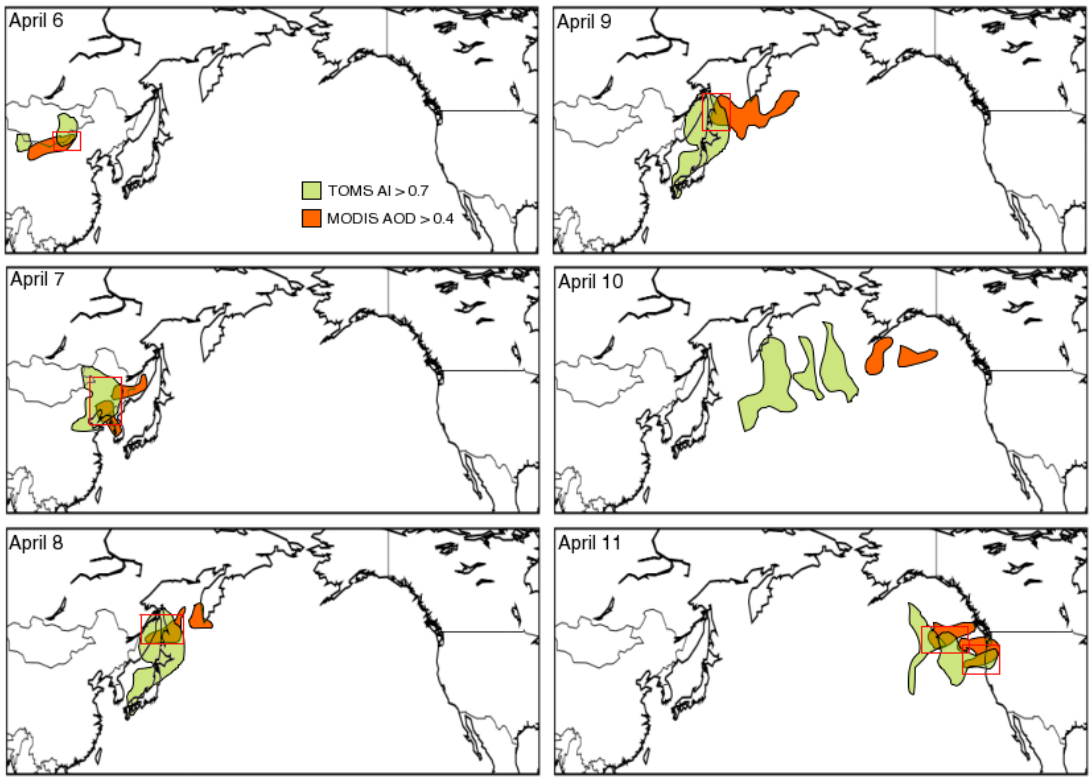

Figure 30: TOMS AI and MODIS AOD dust plume contours during the long-range transport across the Pacific Ocean. Red squares represent the areas with overlapping dusty pixels retrieved from both instruments, corresponding to high level of confidence for a presence of dust.

the intrinsic limitations of individual data sets. However, over the oceans satellite measurements in most cases are the only available tool. At this current stage of development of remote sensing products, we believe that using the collective capabilities of individual datasets, by introducing a level of confidence for the presence of dust depending on the percentage of overlapping dusty pixels from different datasets (see Figure 30) can provide a reliable constraint for aerosol transport models, ultimately leading to improved spatiotemporal characterization of dust distributions on regional and global scale. Integrated data sets could also help to identify the temporal and spatial scales at which the intercomparison between dust transport models and observations would be the most efficient.

CHAPTER IV

SPATIAL DYNAMICS OF ASIAN SOURCES AND IMPLICATIONS FOR THE ASSESSMENT OF THE ANTHROPOGENIC DUST FRACTION

4.1 Introduction

The climate of Northern Eurasia has been undergoing major changes in the past century [*Small et al.,* 2001]. Growing evidence suggests that land- use/land-cover changes and increasing amounts of anthropogenic aerosols might be among the key drivers of observed climate change [*IPCC,* 2001]. Among the main aerosol types, wind-blown mineral dust is strongly affected by human-induced land-cover and land-use changes. Desiccation of the Aral Sea, conversion of the steppe in Kazakhstan to the agriculture fields in the 1950s, and severe desertification of northeast China resulting in the formation of new deserts are just a few examples of land-use changes that occurred in Asia and potentially led to increased dust loads [*Orlovsky and Orlovsky,* 2002; *Xuan and Sokolik,* 2002]. The fraction of the dust load that originates from human-perturbed sources, called anthropogenic dust, is of special interest in climate change studies because of the important diverse impacts that atmospheric dust can exert upon the Earth‘s systems. Despite its important role, quantification of anthropogenic dust and its impact upon climate and the environment remain highly uncertain. Table 7 compares recent studies, which reported estimates of the percentage of atmospheric dust load originating from anthropogenic changes in land-use. Notice that the estimated anthropogenic dust fraction varies from 0 to 60%. This large range of uncertainties stems from the challenges in distinguishing natural dust sources from anthropogenic ones [*Sokolik and Toon,* 1996; *Tegen et al.,* 2004] as well as from the inherent problems of

GCMs used for calculation of dust loads (see Chapter II).

Table 7: Existing estimates of the anthropogenic dust fraction.

Study	Anthropogenic dust fraction
Tegen and Fung [1995]	$30 - 50\%$
Sokolik and Toon [1996]	$\sim 20\%$
Mahowald and Luo [2003]	$14 - 60\%$
Tegen et al. [2004]	$< 10\%$
Mahowald et al. [2004]	$0 - 50\%$

In Central Asia, intensive irrigation from the rivers feeding the Aral in a combination with the arid continental climate resulted in a drastic decrease of the lake water body over the last 50 years. Since the 1960s, the Aral Sea area decreased by half exposing about 42000 km^2 of the highly erodible dried sea bed [*Singer et al.*, 2003]. In addition to forming an active dust source, it has been suggested that the Aral Sea desiccation has affected the air temperature and hydrological cycle in the region and hence contributed to climate change [*Small et al.*, 2001].

In East Asia, the rapid economic growth over the last 50 years resulted in increasing the desert area by 2–7%. Depending on the degree of desertification, newly formed deserts cover 15–19% of the original desert areas and would generate more dust storms, ranging from 10% to 40% under the same meteorological conditions for spring 2001 [*Gong et al.*, 2004].

The increase of dust production from Central and East Asia will certainly result in an increase of the atmospheric dust burden in mid- latitude regions. Improved assessments of anthropogenic dust will be required to constrain the role of different individual factors as well as their coupled impacts in controlling climate change in these regions. The goal of this chapter is to investigate the spatial dynamics of dust sources in Central and East Asia to: (1) isolate an anthropogenic dust signal from one originating from the vast natural deserts and (2) assess the anthropogenic fraction of dust in the model-predicted total dust load and

associated uncertainties. In addition, we investigate possible changes in the meteorological variables due to human induced land-use changes.

4.2 Modeling setup and approach

We used the regional dust modeling system described in Chapter II to simulate 5-day dust outbreaks in April 2001, which occurred in both Central and East Asia. We performed 1-way nested modeling experiments similar to those discussed in Chapter II, but we allowed the area of the Aral Sea and the desert areas in East China to vary within domain B. Dynamics of the desiccation of the Aral Sea used in MM5 simulations is shown in Figure 31 (see region C). The motivation for introducing the region C in addition to the domain B was based on a study of *Small et al.* [2001]. They pointed out that desiccation of the Aral resulted in the changes of the meteorological variables in the surrounding region (decreasing the lake effect). This implies that the drying-up of the Aral can not only affect the dust emission by expanding the source area, but also by affecting atmospheric characteristics, especially winds. To reproduce the drying up of the Aral, the water mask in MM5 was partially or completely removed. A barren land vegetation category was assigned to the exposed grids. Three cases of modeling experiments (called full lake, FL; half lake, HL, and no lake, NL, see region C in Figure 31) were performed. In the full lake experiment, we used the water mask available from AVHRR land-use data collected in 1992–1993. The half lake case represents the current area of the Aral Sea, whereas in the case of the no lake experiment we completely removed the water body (see Figure 31). The current surface area of the Aral used in our simulations agrees with recent studies [*Orlovsky and Orlovsky*, 2002; *Singer et al.*, 2003; *Small et al.*, 2001].

In contrast to the Aral Sea where the area for the no lake scenario can be easily predicted, the estimates for the anthropogenic dust sources in East Asia vary significantly. Figure 32 shows four different desertification scenarios suggested by different institutions. The desertification categories for each scenario are based on different criteria. While the

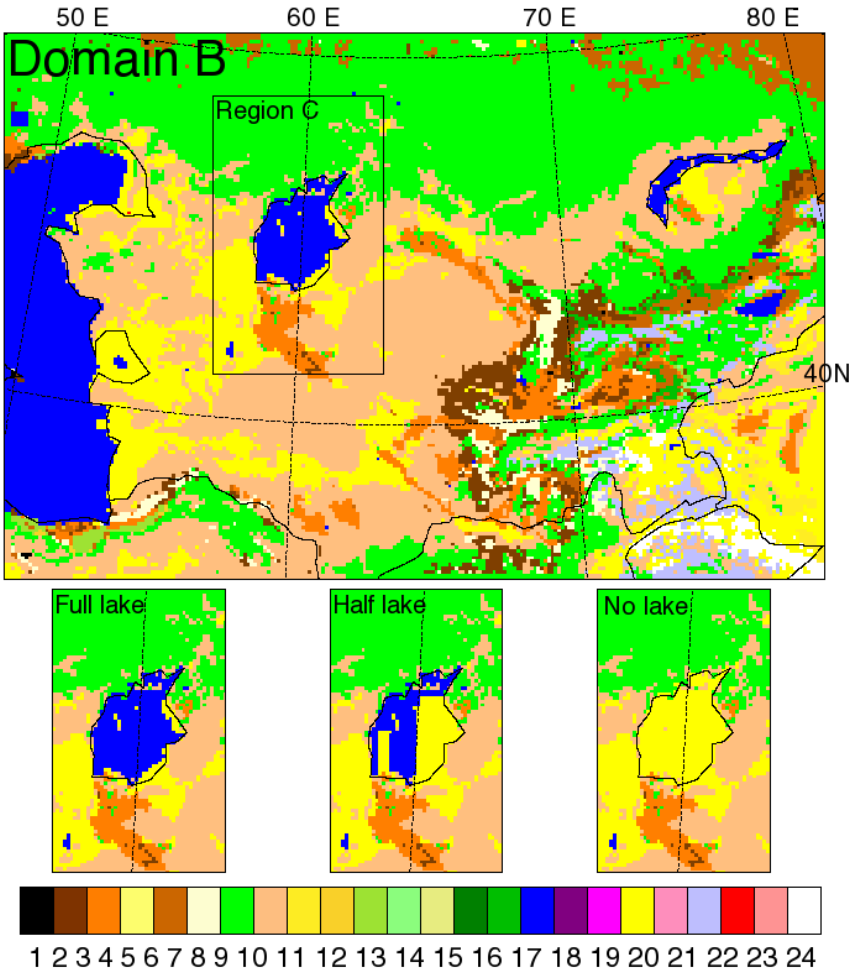

Figure 31: Desertification scenarios used for calculation of the anthropogenic dust fraction in Central Asia.

Chinese Academy of Sciences (CAS) and the China National Committee for the Implementation of International Convention to Combat Desertification (CCICCD) maps report the level of desertification, UNEP scenario gives the severity of soil degradation. In turn, the United States Department of Agriculture (USDA) maps show land vulnerability to erosion. We chose to work with the CAS and CCICCD desertification maps (hereafter abbreviated as CAS and CCICCD scenarios). The area and distribution of different desertification types and classes in the CCICCD scenario were produced based on the Landsat TM data, which

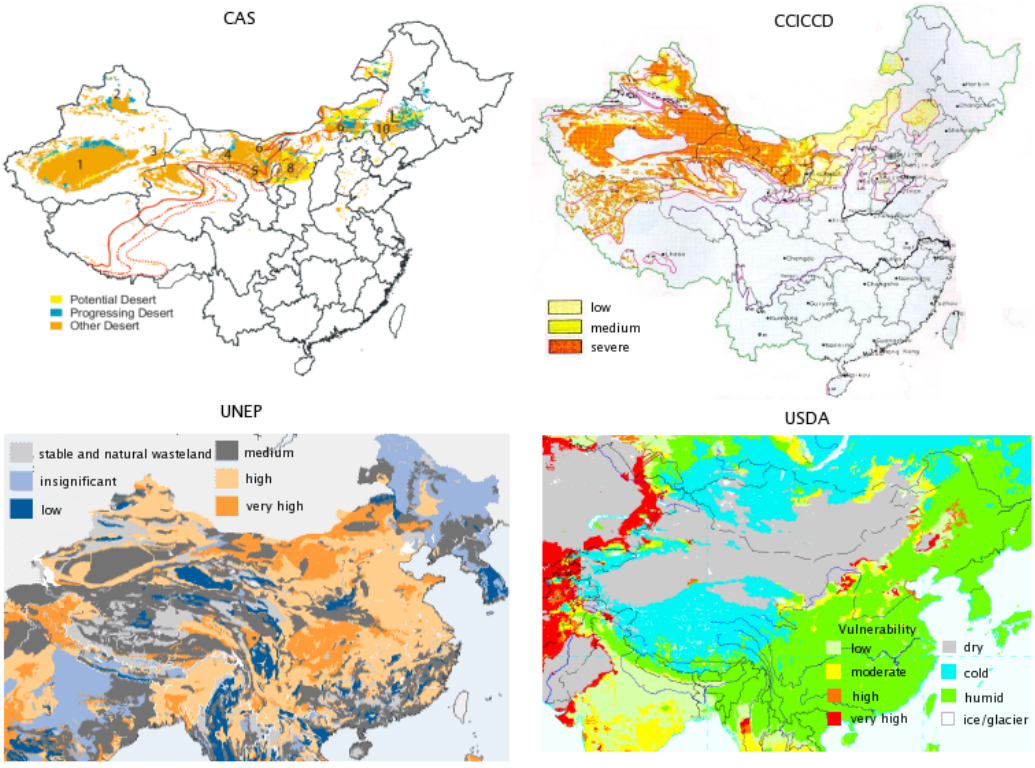

Figure 32: Desertification scenarios based on the estimates of the Chinese Academy of Sciences (CAS), China National Committee for the Implementation of International Convention to Combat Desertification (CCICCD), United Nation Environmental Program (UNEP) and the United States Department of Agriculture (USDA).

were combined with the ground survey guided by GPS during year 2000. The CAS scenario is based on geologic surveys and satellite images of desert areas from the 80s and 90s compiled by the Chinese Academy of Science in the so-called "Resource and Environment Database" [*Zhang et al.*, 2003b]

Estimates of desertification in Mongolia were based on the map from the Chinese Institute of Forest Resources (CIFR) (see Figure 33). The new erodible area over Mongolia was kept the same for both CCICCD and CAS scenarios. To reproduce the land use mask similar to that used in CAS and CCICCD, we removed the shrubland and grassland land-use categories in East Asia and replaced them with barren non-vegetated land (see Figure 34).

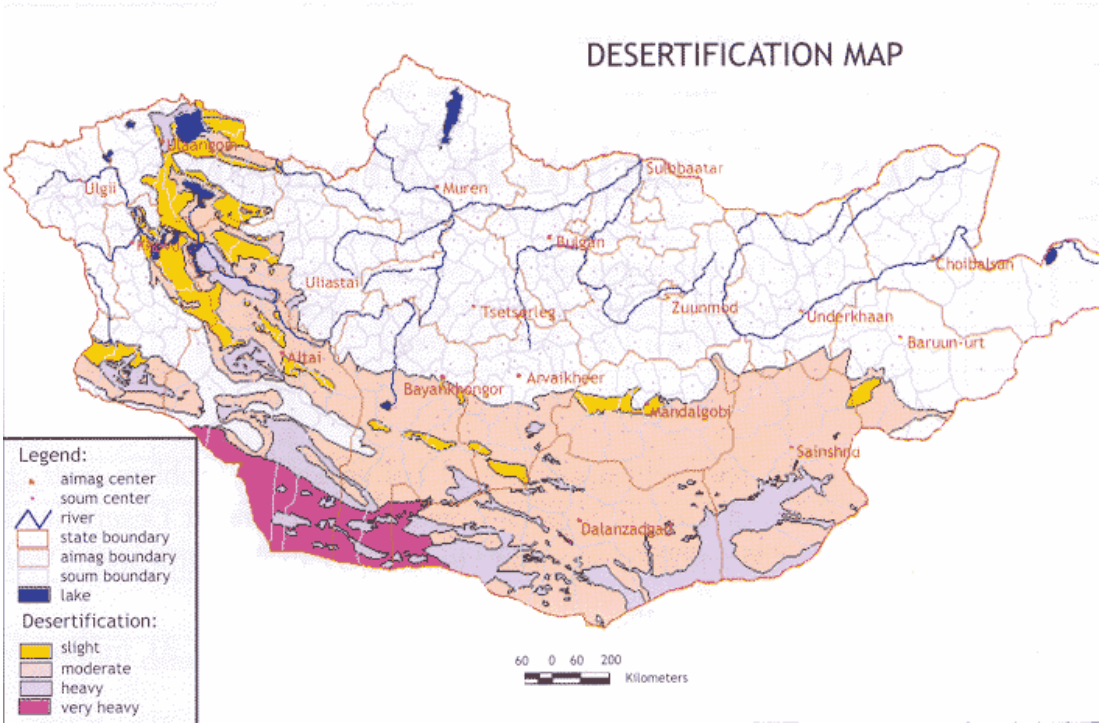

Figure 33: Desertification map for Mongolia based on the estimates of the Chinese Institute of Forest Resources (CIFR).

The default 25 category USGS land mask incorporated in MM5 (see Chapter II) served as a baseline experiment.

MM5 simulations of meteorological fields with all desertification scenarios for Central and East Asia were carried out, and in each case U_{10} - and u_* - driven dust fluxes (see Table 1 in Chapter II) were calculated and analyzed.

4.3 Assessment of the anthropogenic dust fraction in Central and East Asia and associated uncertainties

Table 8 presents the ratios of the no and half lake fluxes to full lake fluxes for considered dust production schemes in the case of MRF and BLK PBLs for Central Asia. These ratios were computed using fluxes integrated over either the domain B or the region C. In both cases dust fluxes were integrated in time over the entire period. The integral of the

dust fluxes over the domain and over the time period is proportional to the total dust mass emitted. Thus, the ratios shown in Table 8 can be interpreted as the ratio of total dust mass emitted in the domain B (or region C) in the no and half lake cases to the total mass emitted in the domain B (or region C) in the full lake case. Therefore, these ratios show the fraction of anthropogenic dust produced by desiccation of the Aral.

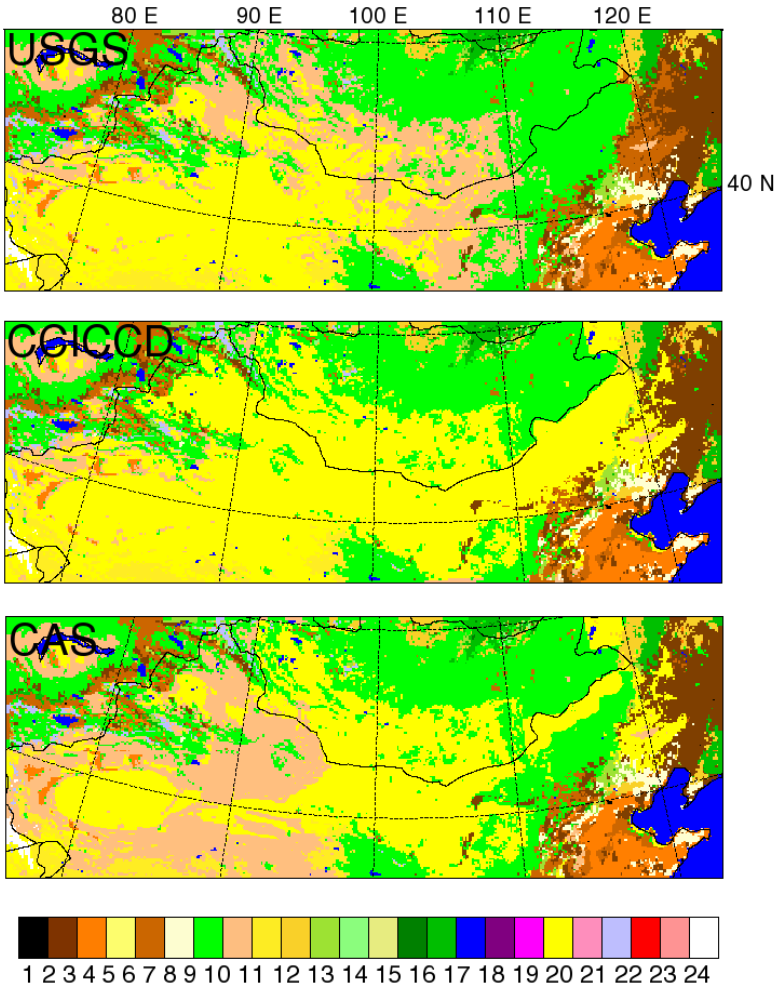

Figure 34: Desertification scenarios used for calculation of the anthropogenic dust fraction in East Asia.

It can be observed that the ratios calculated for the domain B with the MRF PBL scheme are within 1% for the all dust schemes, whereas for the BLK PBL they are about 5% and

Table 8: Ratios of the area- and time-integrated dust fluxes for the half and no lake experiments to the full lake flux simulated with MRF and BLK PBLs employing either U_{10} - or u_* - driven dust emission schemes. The results are shown for the domain B and region C.

Experiment	Domain B		Region C	
	MRF	BLK	MRF	BLK
		U_{10}		
Full lake	1	1	1	1
Half lake	1.008	1.05	1.09	1.41
No lake	1.006	1.06	1.10	1.48
		U_{10*}		
Full lake	1	1	1	1
Half lake	1.007	1.21	1.09	1.43
No lake	1.007	1.22	1.12	1.52
		MB95		
Full lake	1	1	1	1
Half lake	1.009	1.20	1.10	1.38
No lake	1.012	1.21	1.15	1.48
		O64		
Full lake	1	1	1	1
Half lake	1.008	1.20	1.10	1.40
No lake	1.010	1.21	1.14	1.50
		W79		
Full lake	1	1	1	1
Half lake	1.009	1.19	1.10	1.39
No lake	1.011	1.21	1.14	1.49
		GP88		
Full lake	1	1	1	1
Half lake	1.005	1.19	1.08	1.48
No lake	1.005	1.21	1.10	1.57
		O64 (D01)		
Full lake	1	1	1	1
Half lake	1	1	0.95	1.84
No lake	0.99	1	0.76	1.79
		O64 (MM5)		
Full lake	1	1	1	1
Half lake	0.99	1.18	0.98	1.92
No lake	0.99	1.18	0.85	1.94

20% for U_{10} - and u_* - driven schemes, respectively, when the lake is completely removed. In contrast, ratios in the region C in the no lake case vary between 8% and 94% for the MRF and BLK PBL schemes, respectively. Another interesting finding is that the two modifications O64(DO1) and O64(MM5) of our newly developed advanced scheme, which takes into account land surface properties for calculation of the threshold friction velocity (see Section 2.2 in Chapter II), produce smaller fluxes for the half and no lake compared to the full lake case. Since the dust source area is increasing as a result of the lake desiccation, decreasing dust fluxes can be explained only by decreasing winds over the domain. This is confirmed by our analysis of modeled surface winds.

To illustrate, Figure 35a shows the no lake to full lake differences in the surface winds at 10 m for April 7, 2001, 18 UTC. It is evident that desiccation of the Aral Lake causes decrease of the surface winds over the lake bed with more than 2 m/s. However, outside the lake the winds can increase or decrease depending on the PBL parameterization. The behavior of the friction velocity (Figure 35b) is more complex and it can increase or decrease both inside and outside the lake bed depending on the time of the day. To further investigate this issue, we plotted the U_{10} and u_* calculated with the MRF PBL for the full and no lake case at two model grid cells located inside and outside the lake bed, with coordinates (44.97°N, 59.92°E) and (44.99°N, 58.20°E), respectively (see Figure 36). It is evident from the plot that U_{10} inside the lake bed decrease when the water body is removed. While winds at 10 m inside the lake bed are always lower compared to those outside the lake contour regardless of the time of the day, the friction velocity inside the lake tends to increase/decrease during the day/night compared to the velocity outside the lake. The distinct behavior of U_{10} and u_* inside and outside the lake contour as a result of the desiccation, in combination with the higher on average threshold velocity (0.8 m/s) for the advanced O64(DO1) and O64(MM5) schemes explains the anthropogenic fractions smaller than 1. It is evident from the above discussion that the anthropogenic dust fraction depends on a combined effect of several factors such as wind changes inside and outside the lake bed,

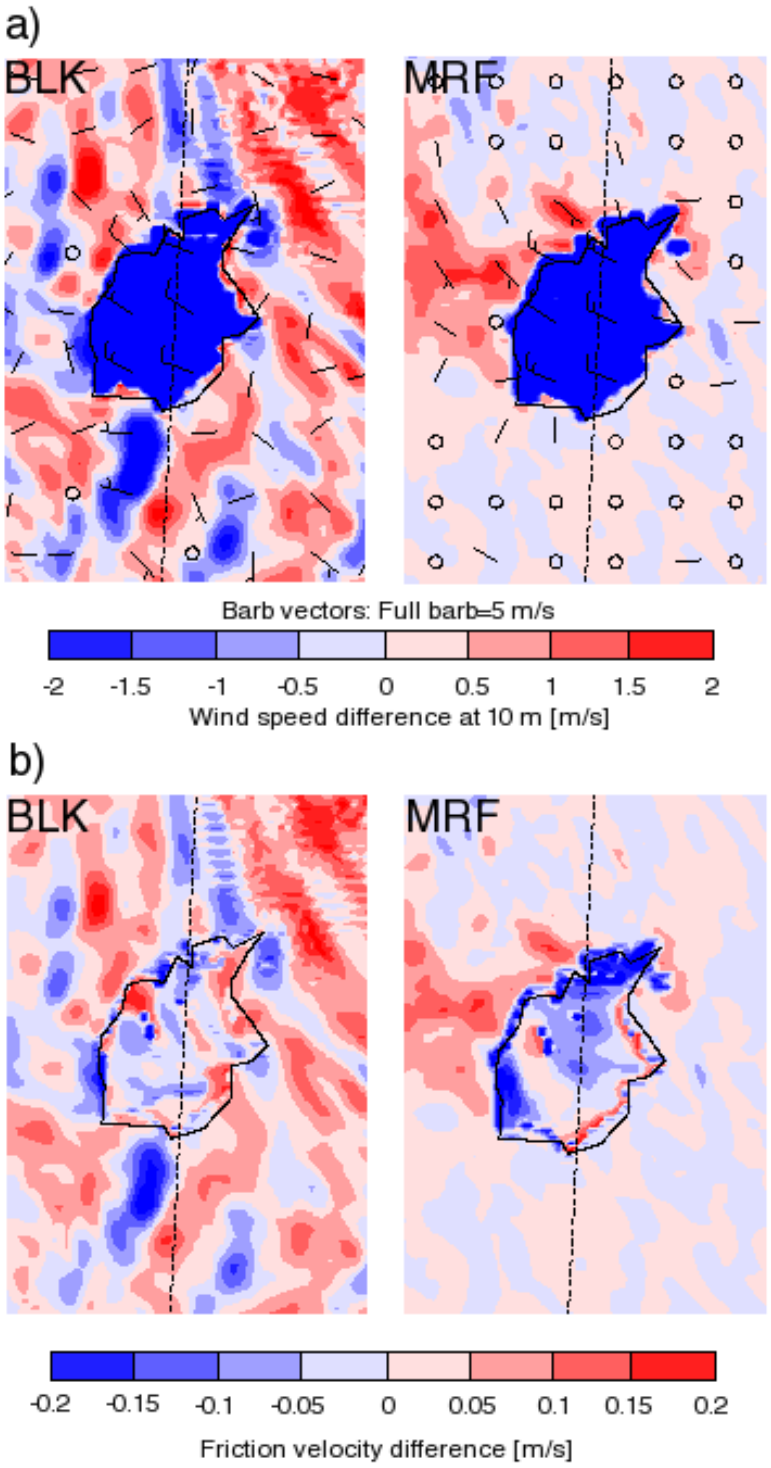

Figure 35: No lake to full lake differences in a) Surface winds at 10 m; b) Friction velocity for MRF and BLK PBLs for 7 April, 2001 at 18 UTC.

the threshold velocity selected for dust production, and the increase of the source area.

Thus, an interesting question arises. Can we delineate the relative changes in the total dust fluxes due to an increase of the erodible area from those that caused by changes in surface winds resulted from the land cover change? To investigate this issue, we calculated the total dust loads for domain B in two different ways. First, we used the winds simulated with MM5 before the land/water mask was changed (referred to as "old winds") in a combination with the MM5 land cover and roughness maps after the land/water mask was changed (denoted as "new land cover"). Thus, we expect that fluxes calculated with the "old winds" and "new land cover" will give us a fraction of dust mass due to land cover changes. The relative error of total dust loads due to changes in the land cover texture and surface winds was calculated as:

$$R_T = \frac{F_{NL}^{NW} - F_{OL}^{NW}}{F_{NL}^{NW}} \tag{22}$$

where NW, OL and NL stand for "New Winds", "Old Land cover" and "New Land cover", respectively. Next, we calculated dust fluxes by using "new winds" and "old land cover" in a similar fashion as described above. The second experiment is expected to produce a fraction of total dust mass due to wind variability resulting from land cover changes. The relative error of total dust loads due to changes in the surface winds is calculated as:

$$R_W = \frac{F_{NL}^{NW} - F_{NL}^{OW}}{F_{NL}^{NW}} \tag{23}$$

Figure 37(a, b) shows the relative errors in total dust fluxes due to wind and land cover changes calculated with the MRF PBL. Figure 37a illustrates that for the Aral Sea region, the changes in winds and land cover as a result of the desiccation lead to an increase in total dust fluxes calculated with all simple u_*-driven schemes. The combined relative errors due to changes in winds and land cover reach up to 2.5% indicating that the anthropogenic dust fraction is relatively small. Figure 37b shows that for the advanced O64(DO1) and O64(MM5) schemes and the U_{10}-driven scheme, the land cover and wind speed changes

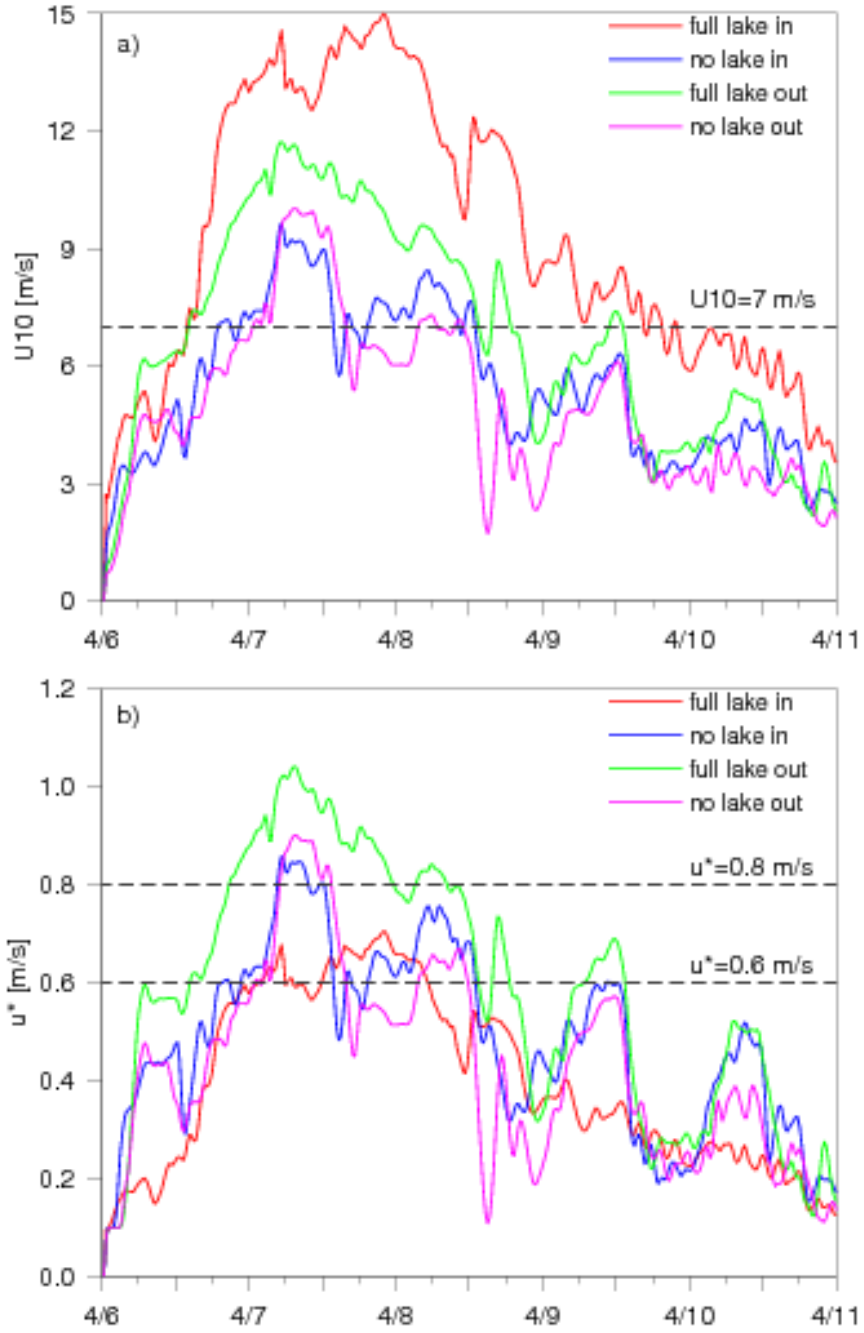

Figure 36: a) Surface winds at 10 m calculated with the MRF PBL for the full and no lake case for two model grid cells located inside and outside the lake contour. b) Same as a) but for the friction velocities.

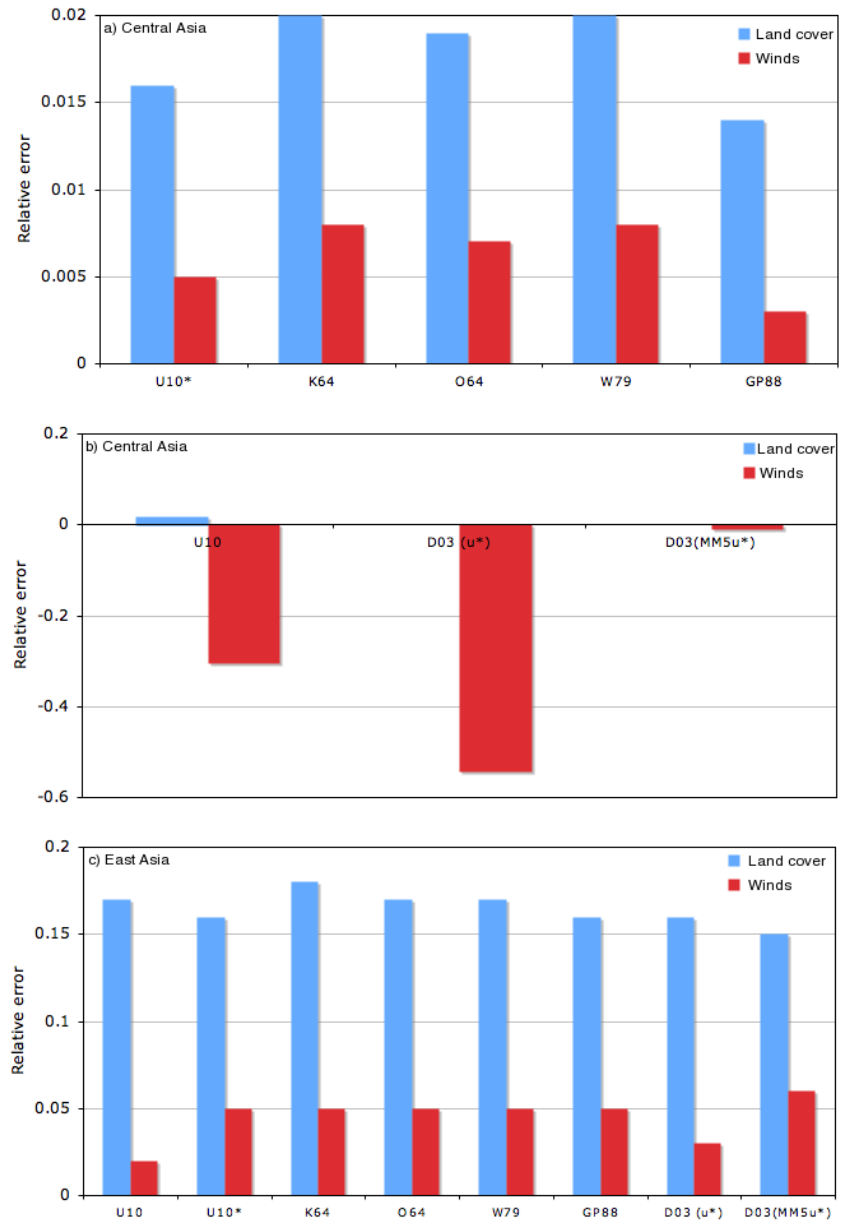

Figure 37: a) Relative error in the total dust mass as a result of the land cover and surface wind change in Central Asia for the u_* - driven schemes; b) Same as a) but for U_{10}, O64(D01) and O64(MM5) schemes; c) Same as a) for all dust production schemes in East Asia.

drive total dust fluxes in different direction. The negative change in total dust fluxes for these dust emission schemes is a good example of how the selection of the threshold speed can overcompensate land cover and wind changes and actually can lead to decrease in total dust loads. It has to be pointed out that this effect is observed only in the case of the MRF PBL since it tends to predict weaker surface winds (see Section 2.4.3 in Chapter II). BLK PBL produces overall higher winds, thus model predicted dust loads are not that sensitive to the selection of the threshold velocity.

Table 9: Ratios of the area- and time-integrated dust fluxes for the CAS and CCICCD experiments to the USGS flux simulated with MRF PBL employing either U_{10} - or u_* - driven dust emission schemes. The results are shown for the domain B.

	U_{10}	U_{10*}	MB95	O64	W79	GP88	O64 (D01)	O64 (MM5)
USGS	1	1	1	1	1	1	1	1
CAS	0.98	0.99	1.02	1.01	1.01	0.97	0.95	0.95
CCICCD	1.21	1.23	1.25	1.25	1.25	1.23	1.21	1.22

The anthropogenic dust fraction for East Asia was calculated as the ratio between the total fluxes computed for the CAS and CCICCD scenarios to the total flux obtained from the baseline USGS case. Table 9 shows the anthropogenic dust fractions for all dust emission schemes considered. The calculated fractions indicate that CAS and USGS cases produce somewhat similar dust loads. The discrepancies in dust loads are from -5% to 2% depending on the dust production scheme. For the CCICCD scenario, the anthropogenic fraction varies between 21% and 25%. The CAS and CCICCD scenarios give an increase of the source area of 6% and 20%, respectively. The numbers in Table 9 indicate that similar to Aral Sea region, the anthropogenic dust fraction in East Asia cannot be assumed to be simply proportional to the percentage of the new source area. Figure 37c shows the relative contribution of the land cover and wind changes to changes in total dust fluxes, calculated with Eq. (22) and (23) for the CCICCD desertification scenario. It is observed that the changes in winds and land cover act in the same direction of increasing total dust loads up

to 25%.

It is evident that for both Central and East Asia the anthropogenic dust fraction is not directly proportional to the new source area. This effect is more pronounced in the Aral region. This can be explained by the fact that in Central Asia the water body is replaced by the erodible land with quite different surface properties. These land surface parameters are critical for parameterization of the sensible heat flux, which in turn controls the friction velocity and surface winds in the PBL. In contrast, when the land cover category in East Asia is replaced by one with similar land surface characteristics, the effect on the model-predicted winds is not that well pronounced.

Careful examination of Tables 8 and 9 indicates that the anthropogenic dust fraction in Central and East Asia depends on the choice of model physics and a dust emission scheme. Figure 38a shows the range of estimated uncertainties in the anthropogenic dust fraction due to different dust emission schemes for the CAS and CCICCD scenarios. The red and the blue squares represent the estimates of the anthropogenic dust fraction for each individual scheme while the red and blue lines represent the average anthropogenic dust fraction from all schemes. The average anthropogenic dust fraction for the CAS scenario actually decreases compared to the USGS baseline case, and it is estimated to be -1% with a range of uncertainty between -5% and 2%. For the CCICCD scenario, the anthropogenic dust fraction is 23% with an uncertainty of ± 2%. Figure 38b shows the range of uncertainties in the estimated dust loads due to the combined effect of PBL parameterization and the selection of emission scheme for the no lake case for region C in Central Asia. The estimated average anthropogenic fraction is 30% with a range of uncertainty between -24% and 94%. It can be observed that the use of different PBL parameterizations results in larger discrepancies in dust loads compared to those from dust emission schemes. Exceptions are the schemes with the variable threshold value, which result in discrepancies comparable to those introduced by the PBL parameterizations.

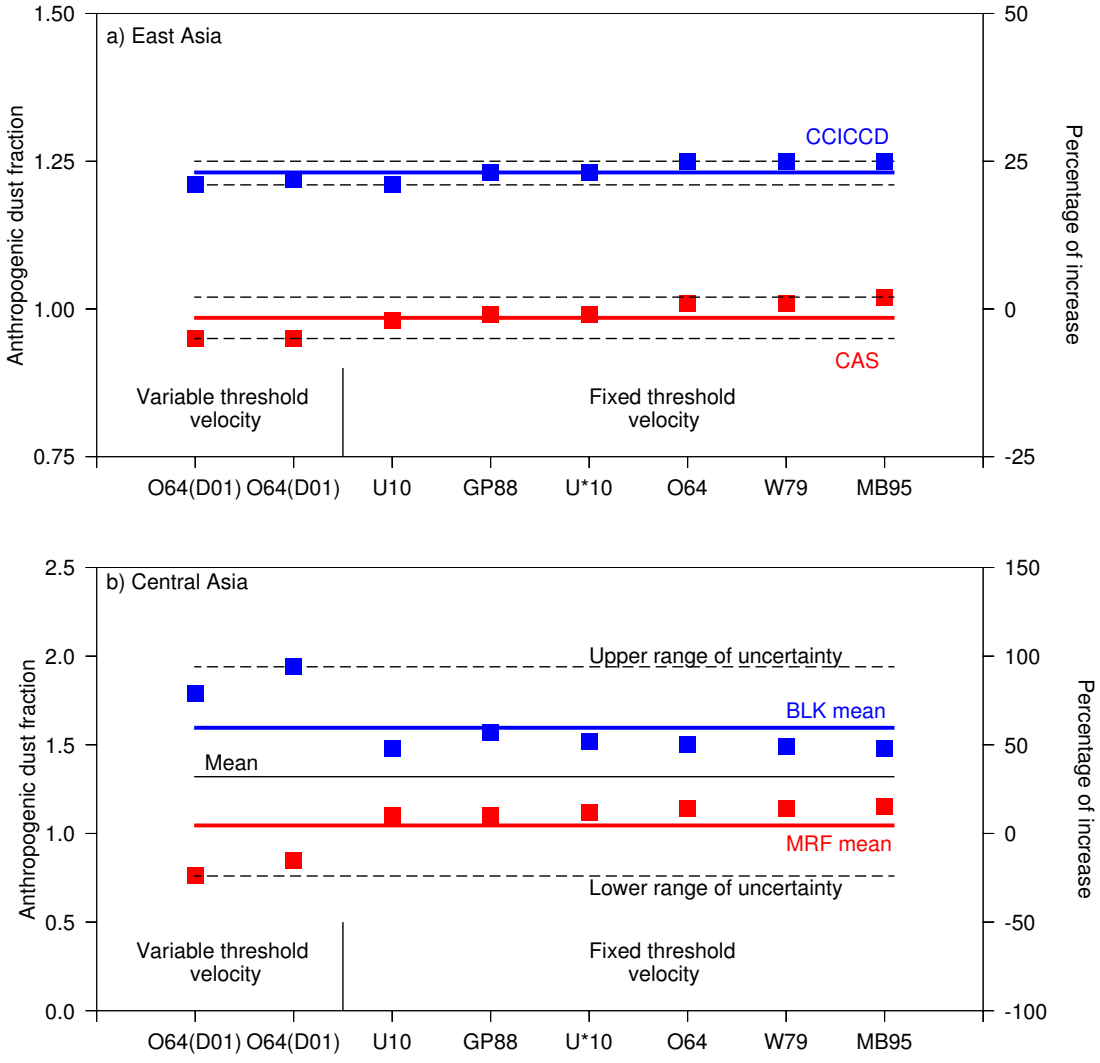

Figure 38: Estimated range of uncertainties in the anthropogenic dust fraction for a) East Asia and b) Central Asia.

4.4 Implications for regional climate

Several studies suggested that anthropogenically formed arid regions induce local mesoscale circulations [*Small et al.*, 2001; *Okin and Gillette*, 2004]. This effect is commonly observed in salt flats or dried lakebeds, which have a number of surface properties, such as thermal conductivity, albedo, vegetation and latent heat fluxes, significantly different from their surroundings. As a result, a phenomenon called "salt breeze" or "playa breeze", similar to the lake breeze effect, is observed due to differences in differential heating of the surfaces [*Rife et al.*, 2002].

We investigated a possible change in the meteorological variables due to land cover changes by comparing the surface winds and temperatures predicted by MM5 for the different desertification scenarios in Central and East Asia. Figure 39 shows the no lake to full lake temperature and surface winds differences at 10 m for April 7 2001, 12 UTC (local day time) and 18 UTC (local night time) calculated with both PBLs. It is evident that the removal of the water body leads to fast heating/cooling of the lake bed during the day/night. The BLK PBL shows increased response of the surface temperature not only in the vicinity of the lake but also in the entire Aral Sea basin. The diurnal temperature difference for both PBLs reaches up to 4 degrees as a result of the desiccation of the lake. This is in agreement with the findings of *Small et al.* [2001] who argued that the Aral Sea serves as an important temperature buffer in the arid continental climate of Central Asia. Thus, desiccation of the Aral can result in larger diurnal temperature differences. As already pointed out in the previous section, the lake desiccation alters the wind pattern inside and outside the lake bed. Therefore, it is evident that removal of the lake has important implications on the surface temperatures and mesoscale circulations in the vicinity of the Aral Sea basin.

Figure 40 shows the temperature and surface winds differences at 10 m in East Asia for April 7 2001, 06 UTC (local day) and 18 UTC (local night) calculated with MRF PBL for CAS and CCICCD scenarios relative to the USGS baseline case. It is evident that the change of the shrubland and grassland land cover to barren non-vegetated surface results in

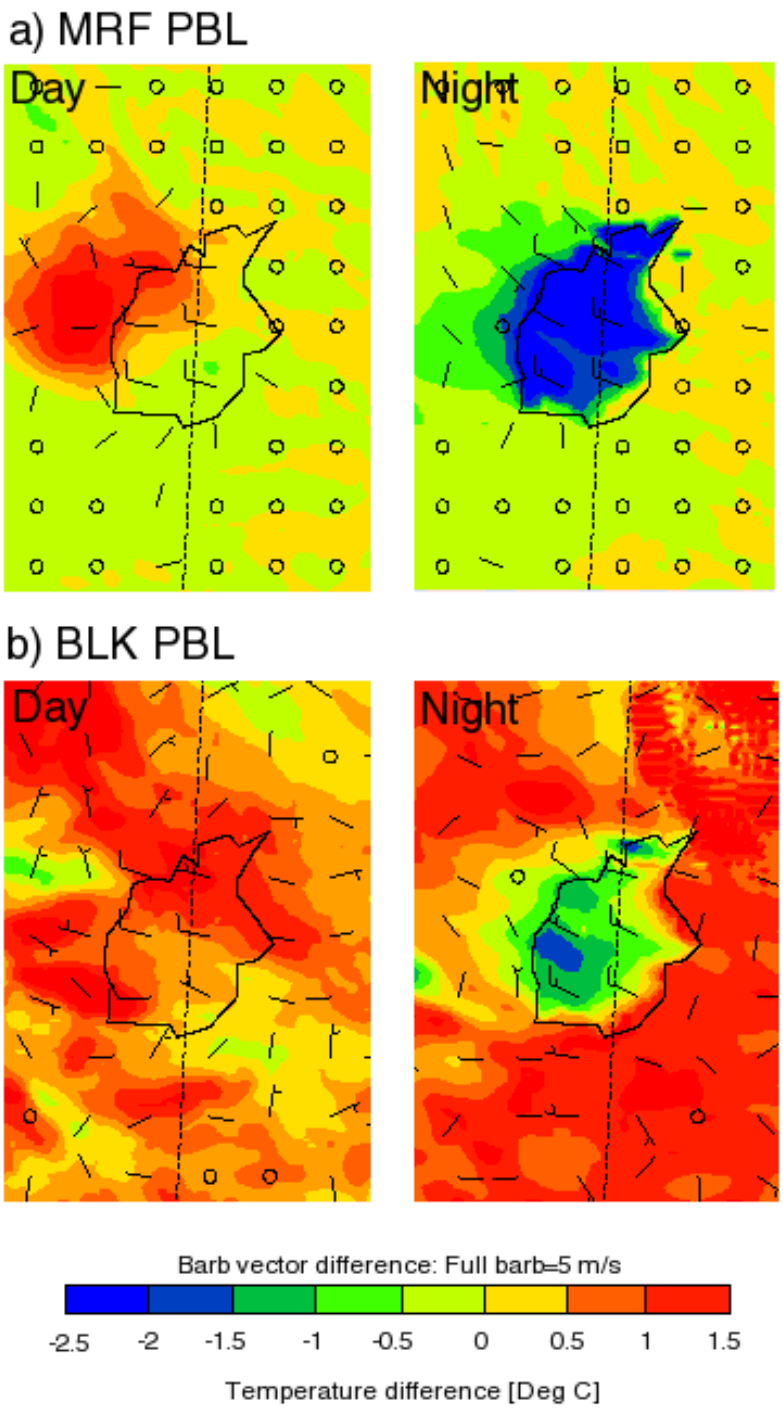

Figure 39: No lake to full lake temperature and surface winds differences at 10 m for April 7 2001, 12 UTC (local day) and 18 UTC (local night) calculated with a) MRF PBL; b) BLK PBL.

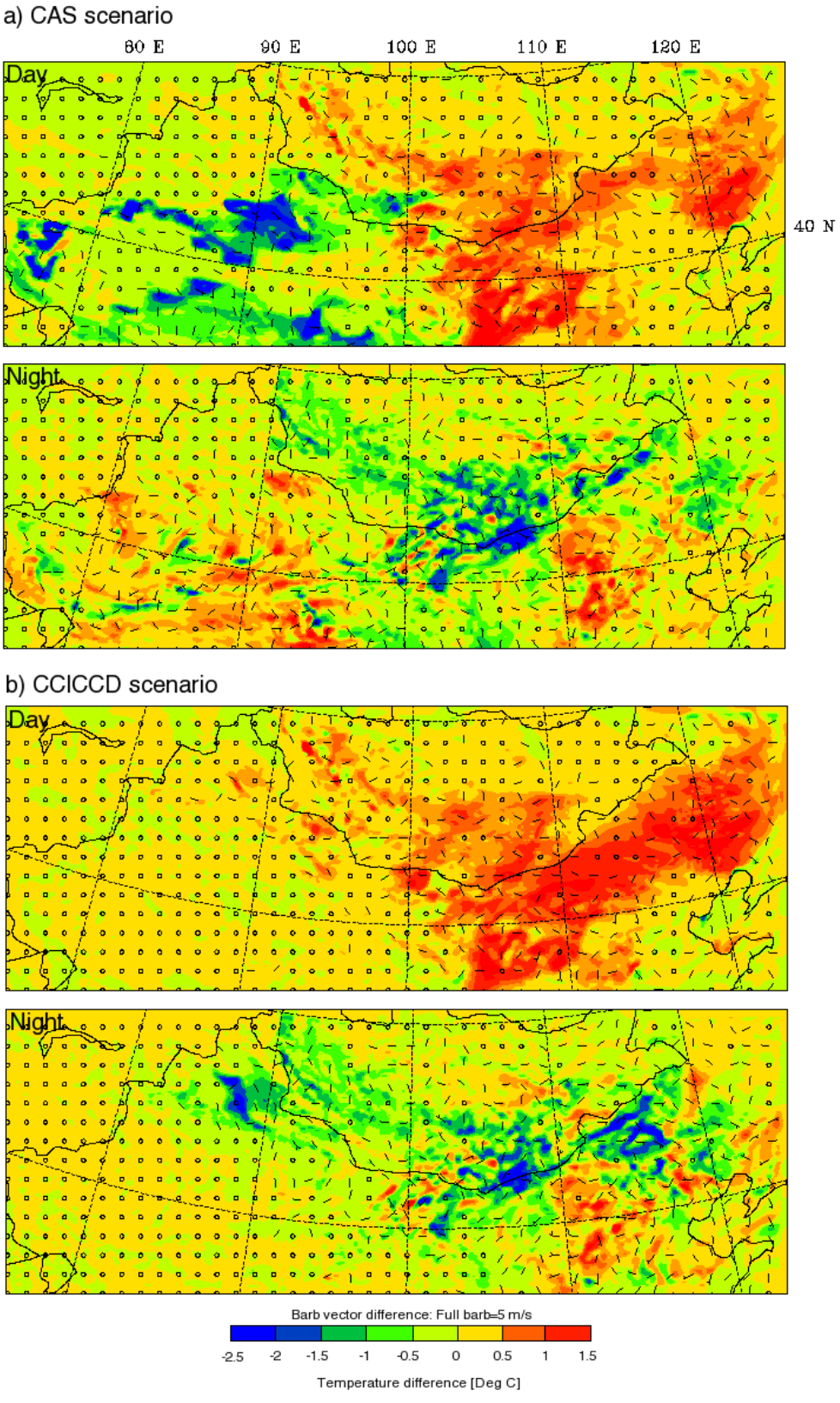

Figure 40: Temperature and surface winds differences relative to USGS baseline run at 10 m for April 7 2001, 06 UTC (local day) and 18 UTC (local night) calculated with MRF PBL for a) CAS scenario; b) CCICCD scenario.

increase of the diurnal temperature contrasts. Figure 40 illustrates that Northeast China and Central Mongolian Gobi experience significant changes in the surface temperature and winds. Thus, despite the uncertainties in the current estimates of desertification in East Asia, it is undisputed fact that land cover changes affect the local climate and the environment.

4.5 Conclusions

The human-induced land-use and land-cover changes in Central and East Asia produced large erodible areas with a high potential for dust emission. The goals of this chapter were to estimate the anthropogenic dust fraction in Central and East Asia given the full range of uncertainties due to model physics, desertification scenarios and dust production schemes.

We demonstrated that the magnitude of the anthropogenic dust fraction depends on a combination of three factors: increased source area, changes in surface winds as a result of altering the land cover, and the threshold velocity used in dust emission schemes.

An important conclusion is that the anthropogenic dust loads can be assessed only within a certain range of uncertainties, which are controlled by uncertainties in the desertification scenario, model physics and the dust emission scheme. In this study we found that on average the estimated anthropogenic dust fraction for Central Asia is 30% with a range of uncertainty between -24% and 94%. For East Asia, the anthropogenic dust fraction depends on the selected desertification scenario. The CAS experiment on average resulted in an 1% decrease of the total emitted mass, with a range of uncertainty between -5% and 2% due to use of different production schemes. For the CCICCD scenario, the anthropogenic dust fraction is 23% with an uncertainty of ± 2%.

Desiccation of the Aral Sea and desertification in East Asia has noticeable effect on the surface winds and temperatures on a regional level. Therefore, land cover changes influence not only dust production, but also alter the regional climate leading to significant impacts on the humans and environment.

Main problem that remains to be addressed is the discrimination between natural and anthropogenic dust sources. Different desertification scenarios for East Asia produce up to 20% difference in the estimated anthropogenic fraction. In addition, as already stated in Chapter 2, the existing differences in PBL parameterizations within one numerical model cause large discrepancies in emitted dust loads. Thus, developing a better parameterization of boundary layer physics in arid and semi-arid regions will be critical to improve assessments of dust emissions from natural and anthropogenic sources.

CHAPTER V

CONCLUSIONS

Atmospheric processes in general operate on a variety of temporal and spatial scales, posing an enormous challenge to both models and observations. Dust processes spanning over several orders of magnitude are no exception, though they exhibit characteristic scales that are specific to the dust life cycle. The traditional metrics of daily and monthly means commonly used for analyzing observational data and model simulations fail to capture the true physical nature of dust processes and their characteristic scales. Current global climate models do not incorporate the small temporal and spatial scales needed for adequate resolution of dust processes. This thesis addresses these issues by developing a new regional dust modeling system capable of operating over a range of scales. In addition, ground-based observations and satellite data for spring 2001 were analyzed to determine the extent to which they can be used to characterize the spatiotemporal distribution of dust outbreaks as well as to constrain the models.

The newly developed modeling system consists of a terrestrial preprocessor, which provides adjustable water/land cover mask able to reproduce different desertification scenarios in Central and East Asia, dust module DuMo and the mesoscale model MM5, which offers multiple choices of physical parameterizations and flexible nesting capability. DuMo incorporates several dust emission schemes of different complexity, including a newly developed, physically based scheme that takes into account land surface properties in computing the threshold wind speed. The new modeling system was applied for the first time to dust sources in both Central and East Asia allowing us to perform a comprehensive modeling of the individual dust events as well as explore the main factors controlling dust emission processes. It was also used to investigate the anthropogenic dust signal due to

land-use/land-cover changes for different desertification scenarios in Central and East Asia and associated uncertainties in the estimated total dust loads.

The modeling studies were performed in conjunction with ground-based and satellite data. We analyzed ground-based meteorological data from 750 stations in China and Mongolia during the spring season of 2001. Observed surface winds and visibility were used for identifying the active dust sources and the duration of dust events. A number of satellite images and aerosol products were analyzed such as MODIS true-color images, TOMS Aerosol Index, and MODIS and SeaWiFs aerosol optical depth. The satellite observations were compared against visibility measurements in terms of the spatiotemporal pattern of dust transported over East Asia to evaluate the potential of each data set in constraining the dust distribution. We also examined the extent to which routine surface measurements and satellite products can be used to constrain the timing and duration of model-predicted dust events. In addition, the capabilities of the observations for constraining aerosol transport models were investigated.

We found that model predicted dust fluxes vary as much as one order of magnitude due to changes in the grid resolution from 200 km to 10 km. The results indicate that coarse resolutions will lead to underestimating the intensity of model predicted dust events. Dust fluxes computed at the 200 km resolution fail to capture weak dust events and as a result, produce wrong timing and duration of dust outbreaks.

Our study demonstrates that total dust mass ratios calculated at 200 km, 100 km and 40 km to the 10 km resolution remain nearly constant during strong events. Thus, the total mass simulated with the coarse resolution model can be corrected by introducing a constant factor. However, we found that dust flux ratios vary during weak events, so total dust loads simulated with global models can not be simply corrected as in the case of strong dust events. To address the model resolution-dependent variability of the surface winds, we introduced and compared two different probability density functions (PDF): Bivariate

normal and Weibull. These functions were used by previous studies but were not compared against each other. We found that introducing PDF will result in an increase of instantaneous model-predicted dust fluxes. However, the magnitude of the increase is very sensitive to the selection of a particular PDF and its statistical parameters. Correction for the underprediction of dust loads at the coarse resolutions can be also done by decreasing the threshold wind speed for dust emission, although this approach enables to adjust only the total dust loads but not their spatiotemporal distribution.

We found that, in addition to the model spatial resolution, the selection of dust emission scheme results in noticeable differences in model-predicted dust events. We investigated the performance of several simple dust emission schemes, in which the erodible fraction was prescribed based on land cover/land use categories and the threshold wind speed was kept constant. We found that the differences between considered u_*^3 - driven schemes themselves are much smaller compared to those found between the u_*^4 - and u_*^3 - driven schemes. Thus, our results indicate that the intensity of model-predicted dust events would be more affected by changing the power dependence in the production scheme from three to four than by changing the polynomial expression of the u_*^3 - driven schemes. In addition, we explored the differences in the model-predicted events by comparing dust fluxes calculated with simple dust emission schemes against those obtained from the advanced scheme treating the threshold friction velocity as a function of surface properties. Our results demonstrated that differences in the instantaneous normalized dust fluxes calculated with simple versus advanced dust emission schemes can be up to 60%. These large discrepancies in modeled dust fluxes between the simple and advanced schemes stem from the different treatment of both friction velocity and the threshold friction velocity.

We introduced a probability density function (PDF) of the instantaneous normalized dust fluxes that shows the probability for the dust flux to be within a certain range. Computed PDFs showed that weak dust emission events were more frequent than strong ones

during the considered time period for both regions. For a given PBL, different dust emission schemes resulted in very similar PDFs. However, there were differences between PDFs calculated for the MRF and BLK PBLs. This finding indicates that the choice of the PBL parameterization can affect the timing and duration of modeled dust events.

Furthermore, we demonstrated that the two considered PBLs produced very different instantaneous dust fluxes. The relative error can be as high as 143% during the strong dust emission, and about 34% on average. Our results indicated that the discrepancies in dust fluxes between the two PBL parameterizations are much higher compared to the discrepancy associated with the use of different dust production schemes. Comparing observed winds from selected ground stations with model-predicted surface winds, we found that both MM5 PBLs underestimate the 10 m winds, especially in the case of strong winds. This would result in under prediction of emitted dust mass and incorrect timing and duration of dust events simulated with the MM5 model.

This study is one of the first attempts to identify and quantify the main factors controlling the model-predicted dust emission. We concluded that the selection of the dust emission scheme, model physics and spatial resolution has a strong effect on the timing, duration and intensity of model-predicted dust events. Figure 41 shows the relative contribution of these factors to the overall uncertainty in the model-predicted dust mass. Finding this large range of variability in the model-predicted atmospheric dust loads motivated us to examine the extent to which routine surface observations and satellite retrievals can be used to constrain model simulations of individual dust events and to characterize the complex spatiotemporal distribution of dust loads during dust outbreaks.

We suggested a new approach for classification of dust events in the source region which allows us to discriminate between the dust events of different types and intensity, e.g. dust storms (strong event) and blowing dust (weak event). This approach also helps to constrain the timing and duration of an individual dust event. Based on this classification, we determined five active dust production regions and in East Asia for the spring of 2001:

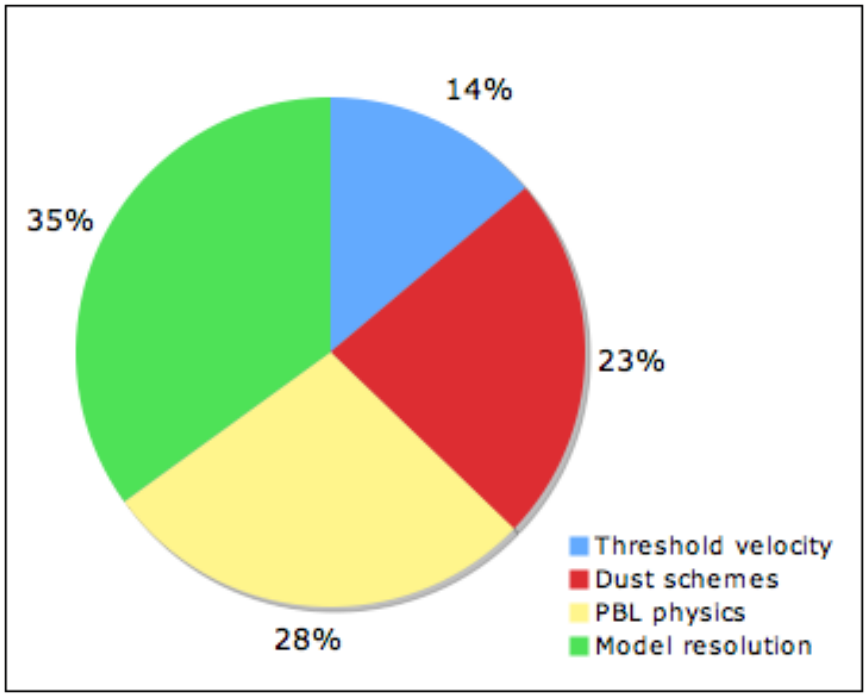

Figure 41: Relative contribution of model physics, spatial resolution and dust emission schemes to the uncertainty in the emitted dust mass, assuming total uncertainty of 100%.

Taklamakan desert, central Chinese Gobi, central Mongolian Gobi, Eastern Chinese Gobi and Eastern Mongolian Gobi. We identified 35 dust events in the source regions for the two spring moths, indicating that the year of 2001 was one of the years with highest activity during the last decade.We concluded that routine visibility observations are a valuable tool in constraining the regions of origin of dust outbreaks and the timing, duration, and intensity of dust events. Thus, the newly developed case-by-case classification can be used to constrain regional models capable of simulating individual outbreaks.

We found a hysteresis-like behavior of visibility as a function of wind speed, for selected stations located in the source region. The shape of the hysteresis curve enabled discrimination between strong and weak dust events. In addition, the direction of the hysteresis curve can indicate whether dust was local or originated upwind. This unique threshold-dependent behavior of visibility can be helpful for constraining emission, boundary layer mixing and deposition schemes in dust transport models.

Visibility observations were also used to reconstruct the mid-range transport of dust outbreaks. The main transport routes in spring of 2001 were found to be to the east, with several cases to the southeast. This is in broad agreement with climatology established by previous studies, though some differences exist in transport routes, especially for the Taklamakan desert. Our analysis revealed that routine visibility observations turned out to be a valuable tool in constraining the mid-range transport of atmospheric dust outbreaks.

The source, mid-range transport, and dissipation of all dust events were analyzed by merging surface and satellite observations. We found that daily TOMS AI agrees with the low visibility patterns in 70% of the cases. Despite the relatively good agreement, TOMS AI is of limited use for validation of individual model-predicted dust events since it represents a 3-day composite product and thus misses the temporal evolution of dust outbreaks on shorter scales. However, this product can be potentially used to validate daily dust distributions predicted by aerosol transport models.

We found that the daily MODIS AOD agrees with the low visibility patterns for 52% of the cases. The large percentage of missing data over land makes MODIS AOD of the limited use for constraining spatiotemporal distributions of dust. Thus, this product needs to be used in conjunction with other observational data (e.g., visibility).

We concluded that MODIS RGB can be used qualitatively for detecting and tracing atmospheric dust outbreaks. MODIS and SeaWiFs instantaneous AOD data showed marginal results in terms of detecting the dust events partly due to the high cloud presence during the studied period. The significant number of pixels with non-retrieved AOD from MODIS and SeaWiFs over land and ocean severely hampers their use for characterizing dust plumes or validating dust models.

Two long-range transport episodes were found during spring of 2001. Long-range transport routes over the North Pacific Ocean were reconstructed using the MODIS aerosol optical depth and TOMS Aerosol Index. The day-by-day dust coverage reconstructed from these satellite products shows broad agreement, though various differences were observed

that might be critical in evaluating the aerosol transport models.

Each individual satellite dataset considered in our analysis has its own specific spatial and temporal scales and it potentially can be used to constrain dust processes on similar scales. However, two major problems in using satellite retrievals to infer spatiotemporal dust distributions have to be pointed out. First, neither the aerosol optical depth nor the aerosol index is specifically designed for retrieving dust. The satellite product algorithms rarely take into consideration the complex regionally-dependent optical and microphysical dust properties; hence the inferred dust distributions will reflect these deficiencies. Second, the same aerosol product retrieved by different satellite sensors exhibit significant discrepancies in the estimated dust distributions due to differences in the retrieval algorithms. Thus, it seems reasonable to combine the capabilities of the existing satellite datasets, by introducing a level of confidence for the presence of dust in order to overcome the intrinsic limitations of individual datasets.

We applied our newly developed dust modeling system to explore the spatial dynamics of dust sources in Central and East Asia and assess the anthropogenic dust fraction. We used different desertification scenarios to calculate the dust flux ratios with several emission schemes and PBL parameterizations to constrain associated uncertainties. We found that the anthropogenic dust fraction is not proportional to the new exposed area, as commonly assumed. The anthropogenic dust fraction in the Aral Sea region depends on the combined effect of wind changes inside and outside the lake bed, the threshold velocity selected for dust production, and the increase of source area. In the case of the East Asian region, major uncertainties in the anthropogenic dust fraction stem from the lack of reliable estimates of desertification. Both regions experienced changes in the meteorological variables on a regional level as a result of land cover change.

Recommendations:

The complex dynamics of dust outbreaks and various limitations of observations and

numerical models pose a major challenge in developing an integrated analysis methodology. Several recommendations for the scientific community are listed below that shall potentially decrease the current uncertainties in the spatiotemporal distribution of dust loads.

1. Coarse spatiotemporal resolution severely hampers the prediction of the intensity and duration of dust events. Global models are likely to fail in capturing weak dust events. GCMs overall underpredict the emitted dust mass and duration of dust events. Modelers can address this problem in three ways: (1) by introducing a subgrid variability of model winds, (2) by reducing the threshold velocity, or (3) by adjusting the dimensional constant in the dust emission scheme by a fixed number that depends on the model grid size.

2. Although the mesoscale models overcome some GCMs problems, regional modelers should be aware of the uncertainties introduced in dust emission modeling by the choice of model physics. The selection of a PBL parameterization should be dictated by its realistic representation of surface winds.

3. Anyone of the simple dust production schemes examined in this study can be used with equal confidence. Major discrepancies stem from the model-predicted winds rather than from the polynomial expression in the dust emission parameterization. The use of advanced dust production schemes can be justified only if detailed information about surface parameters is available. A detailed mapping of the parent soil particle distribution and roughness length will increase the accuracy of model-predicted dust loads.

4. Routine visibility observations can be used to constrain active dust source regions and to characterize the duration of individual dust outbreaks. However, meteorological data is of limited use for validation of dust emission schemes mainly due to the small number of stations in the source regions and the low frequency of observations.

5. Potentially, it is possible to relate the duration and timing of dust events determined from visibility data with those predicted by aerosol transport models. However, a modeler has to ensure that the definition of the start, end and duration of the model-predicted event is based on the same physical assumptions as the one determined from visibility data.

6. Remote sensing observations have high potential in dust studies. However, the current intrinsic limitations of satellite data and their high spatiotemporal intermittency pose challenges for their use as a validation tool for aerosol transport models. Attempts have been made to assimilate retrieved AOD into global models [*Fillmore et al.*, 2005]. Yet, our study shows that discrepancies in the retrievals of the AOD from different instruments over the same regions and time are quite large. At this point, we believe that using the collective capabilities of individual datasets, by introducing a level of confidence for the presence of dust depending on the percentage of overlapping dusty pixels from different datasets can provide a better constraint for aerosol transport models, ultimately leading to improved spatiotemporal characterization of dust distributions on regional and global scales.

Future work

Our work demonstrated that the behavior of dust outbreaks depends strongly on the source region and showed the collective capabilities of satellite data, ground-based observations and regional model simulations in furthering our understanding of the spatiotemporal patterns of mineral dust in Central and East Asia. Several critical issues need to be addressed in the near future to further advance the regional dust studies.

- Detailed geomorphological mapping of dust sources and land surface properties and development of an advanced dust scheme capable of predicting the threshold friction velocity on the regional level will be required.

- Further improvements in parameterizations of boundary layer processes in a mesoscale model are needed, especially in desert and semi-desert regions.
- Performing an ensemble simulation with several mesoscale models (and/or several PBL schemes) can be useful to bracket the uncertainty in model-predicted dust events.

Bibliography

Alfaro, S. C., and L. Gomes (2001), Modeling mineral aerosol production by wind erosion: Emission intensities and aerosol size distributions in source areas, *J. Geophys. Res.*, *106*(D16), 18,075–18,084.

Bagnold, R. A. (1941), The physics of blown sand and desert dunes, *Methuen & Co., London.*

Barnum, B. H., et al. (2004), Forecasting dust storms using the CARMA-dust model and MM5 weather data., *Environmental Modelling and Software*, *19*(2), 129–140.

Beljaars, A. (1994), The parameterization of surface fluxes in large-scale models under free-convecton, *Q. J. R. Meteorol. Soc.*, *121*, 255–270.

Braun, S. A., and W.-K. Tao (2000), Sensitivity of high-resolution simulations of Hurricane Bob (1991) to planetary boundary layer parameterizations, *Mon. Wea. Rev.*, *128*(12), 3941–3961.

Brennan, J. I., Y. J. Kaufman, I. Koren, and R.-R. Li (2005), Aerosol-cloud interaction – misclassification of modis clouds in heavy aerosol, *IEEE Trans. on Geos. & Rem. Sens.*, *43*(4), 911–915.

Cakmur, R., R. L. Miller, and O. Torres (2004), Incorporating the effect of small-scale circulations upon dust emission in an atmospheric general circulation model, *J. Geophys. Res*, *109*(D07201), doi:10.1029/2003JD004067.

Chen, G. T.-J., and H. J. Chen (1987), Study on large scale features of duststorm system in East Asia, *Papers in Meteorological Research. The Meteorological Society of the Republic of China*, *10*, 57–59.

Chepil, W. S. (1945), Dynamics of wind erosion: I. Nature of movement of soil by wind, *Soil Sci.*, *60*, 305–320.

Chin, M., et al. (2003), A global aerosol model forecast for the ACE-Asia field experiment, *J. Geophys. Res.*, *108*(D23), doi:10.1029/2003JD003642.

Chomette, O., M. Legrand, and B. Marticorena (1999), Determination of wind speed threshold for the emission of desert dust using satellite remote sensing in the thermal infrared, *J. Geophys. Res.*, *104*(D24), 31,207–31,215.

Chun, Y., K. O. Boo, J. Kim, S. U. Park, and M. Lee (2001), Synopsis, transport, and physical characteristics of Asian dust in Korea, *J. Geophys. Res.*, *106*, 18,461 – 18,469.

Chung, Y. S., H. S. Kim, K. H. Park, J. G. Jhun, and S. J. Chen (2003), Atmospheric loadings, concentrations and visibility associated with sandstorms: Satellite and meteorological analysis, *Wat. Air. Soil Poll.*, *3*, 21–40.

Dailey, P. S., and J. L. Keller (2002), Modeling of extreme wind events using MM5: Approach and verification, *Preprints, 12th Annual MM5 Users Workshop, Boulder, CO, 17*.

Darmenov, A., and I. Sokolik (2005), Identifying the regional thermal-IR radiative signature of mineral dust with MODIS, *Geophys. Res. Lett., 32*, L16803, doi:10.1029/2005GL023092.

Darmenova, K., and I. Sokolik (2006), Assessing uncertainties in dust emission in the Aral Sea region caused by meteorological fields predicted with a mesoscale model, *Global Environmental Change, In Press*.

Darmenova, K., I. Sokolik, and A. Darmenov (2005), Characterization of east Asian dust outbreaks in the spring of 2001 using ground-based and satellite data, *J. Geophys. Res., 110*(D02204), doi:10.1029/2004JD004842.

Draxler, R. R., D. Gillette, J. K. Kirkpatrick, and J. Heller (2001), Estimating PM_{10} air concentrations from dust storms in Iraq, Kuwait and Saudi Arabia, *Atmos. Environ., 35*, 4315–4330.

Dudhia, J. (1996), A multi-layer soil temperature model for MM5, *Preprints, 6th Annual MM5 Users Workshop, Boulder, CO*.

Fillmore, D. W., W. D. Collins, and A. J. Conley (2005), Aerosol direct radiative forcing - estimates from a global aerosol climatology constrained by MODIS assimilation, in preparation.

Gao, T., L. Su, Q. Ma, H. Li, X. Li, and X. Yu (2003), Climatic analyses on increasing dust storm frequency in the springs of 2000 and 2001 in Inner Mongolia, *Int. J. Climatol., 23*, 17431755.

Gillete, D., B. Marticorena, and G. Bergametti (1998), Change in the aerodynamic roughness height by saltating grains: Experimental assessment, test of theory, and operational parameterization, *J. Geophys. Res., 103*(D6), 6203–6209.

Gillette, D., and R. Passi (1988), Modeling dust emission caused by wind erosion, *J. Geophys. Res., 93*(D11), 14,233–14,242.

Gillette, D. A., J. Adams, A. Endo, D. Smith, and R. Kihl (1980), Threshold velocities for input of soil particles into the air by desert soils, *J. Geophys. Res., 85*, 5621–5630.

Gillette, D. A., B. Marticorena, and G. Bergametti (1998), Change in the aerodynamic roughness height by saltating grains: Experimental assessment, test of theory, and operational parameterization., *J. Geophys. Res., 103*, 6203–6210, doi:10.1029/98JD00207.

Ginoux, P., M. Chin, I. Tegen, J. M. Prospero, B. Holben, O. Dubovik, and S. Lin (2001), Sources and distributions of dust aerosols simulated with the GOCART model, *J. Geophys. Res., 106*(D17), 20,25520,274.

Ginoux, P., J. Prospero, O. Torres, and M. Chin (2004), Long-term simulation of global dust distribution with the GOCART model: correlation with North Atlantic Oscillation, *Environ. Modelling and Software*, *19*, 113–128.

Golitsyn, G. S., I. G. Granberg, A. V. Andronova, V. M. Ponomarev, S. S. Zilitinkevich, V. V. Smirnov, and M. Y. Yablokov (2002), Investigation of boundary layer fine structure in arid regions: injection of fine dust into the atmosphere, *Water ‚Air and Soil Pollution: Focus*, *3*, 245257.

Gong, S., X. Zhang, T. Zhao, I. McKendry, D. Jaffe, and N. Lu (2003), Characterization of soil dust aerosol in China and its transport/distribution during 2001 ACE-Asia 2. Model simulation and validation, *J. Geophys. Res.*, *108*(D9), 4262, doi:10.1029/2002JD002633.

Gong, S., X. Zhang, T. Zhao, and L. Barrie (2004), Sensitivity of Asian dust storm to natural and anthropogenic factors, *Geophys. Res. Lett.*, *31*(L07210), doi:10.1029/2004GL019502.

Goudie, A., and N. Middleton (1992), The changing frequency of dust storms through time, *Climatic Change*, *20*, 197–225.

Grini, A., and C. S. Zender (2004), Roles of saltation, sandblasting, and wind speed variability on mineral dust aerosol size distribution during the Puerto Rican Dust Experiment (PRIDE), *J. Geophys. Res.*, *109*(D7), D07202.

He, Z., Y. Kim, K. O. Ogunjobi, and C. S. Hong (2003), Characteristics of $PM_{2.5}$ species and long-range transport of air masses at Taean background station, South Korea, *Atmos. Environ.*, *37*, 219–230.

Hong, S., and H.-L. Pan (1996), Nonlocal boundary layer vertical diffusion in a medium-range forecast model, *Mon. Wea. Rev.*, *124*, 2322–2339.

Hong, S., J. Dudhia, and Y. Noh (2003), A new vertical diffusion package with explicit treatment of the entrainment processes, *Extended abstract, International workshop on Numerical Weather Forecast Models, Japan*.

Huebert, B. J., T. Bates, P. B. Russell, G. Shi, Y. J. Kim, K. Kawamura, G. Carmichael, and T. Nakajima (2003), An overview of ACE-Asia: Strategies for quantifying the relationships between Asian aerosols and their climatic impacts, *J. Geophys. Res.*, *108*(D23), 8633, doi:10.1029/2003JD003550.

Husar, R. B. e. a. (2001), The Asian dust events of April 1998, *J. Geophys. Res.*, *106*, 18,317–18,330.

Ichoku, C., L. A. Remer, Y. J. Kaufman, R. Levy, D. A. Chu, D. Tanre, and B. N. Holbeni (2003), MODIS observation of aerosols and estimation of aerosol radiative forcing over southern Africa during SAFARI 2000, *J. Geophys. Res.*, *108*(D13), 8499, doi:10.1029/2002JD002366.

IPCC (2001), Intergovernmental panel on climate change (IPCC), Climate Change 2001: The Scientific Basis, Contribution of Working Group I to the Third Assessment Report of the Intergovernmental Panel on Climate Change, edited by J. T. Houghton et al., *Cambridge Univ. Press, New York*.

Iversen, J., and B. White (1982), Saltation threshold on Earth, Mars and Venus, *Sedimentology, 29*, 111–119.

Iwasaka, Y., et al. (2003), Large depolarization ratio of free tropospheric aerosols over the Taklamakan Desert revealed by lidar measurements: Possible diffusion and transport of dust particles, *J. Geophys. Res.*, *108*(D23), 8652, doi:10.1029/2002JD003267.

Iziomon, M., and U. Lohmann (2003), Characteristics and direct radiative effect of mid-latitude continental aerosols: the ARM case, *Atmos. Chem. Phys., 3*, 1903–1917.

Jaffe, D., I. McKendry, T. Anderson, and H. Price (2003), Six "new" episodes of trans-Pacific transport of air pollutants, *Atmos. Environ., 37*, 391–404.

Jung, E., Y. Shao, and T. Sakai (2005), A study on the effects of convective transport on regional-scale Asian dust storms in 2002, *J. Geophys. Res., 110*, doi:10.1029/2005JD005,858.

Justus, C. G., W. R. Hargraves, A. Mikhail, and D. Graber (1978), Methods for estimating wind speed frequency distributions, *J. App. Meteor.*, *17*(350-353).

Kawamura, R. (1964), Study of sand movement by wind, *In: Hydraulic Eng. Lab. Tech. Rep. Number HEL-2-8, 99-108, Berkley, University of California*.

Kim, B.-G., J.-S. Han, and S.-U. Park (2001), Transport of SO_2 and aerosol over the Yellow Sea, *Atmos. Environ., 35*, 727–737.

Kohfeld, K. E., R. L. Reynolds, J. Pelletier, and B. Nickling (2005), Linking the scales of observation, process, and modeling of dust emissions, *EOS Trans*, *86*(11), 113.

Kurosaki, Y., and M. Mikami (2005), Regional difference in the characteristic of dust event in East Asia: Relationship among dust outbreak, surface wind, and land surface condition, *JMSJ*, *83A*, 1–18.

Laurent, B., B. Marticorena, G. Bergametti, P. Chazette, F. Maignan, and C. Schmechtig (2005), Simulation of the mineral dust emission frequencies from desert areas of China and Mongolia using an aerodynamic roughness length map derived from the POLDER/ADEOS 1 surface products, *J. Geophys. Res.*, *110*(D18S04), 2004JD005013, doi:10.1029.

Liu, M., and D. L. Westphal (2001), A study of the sensitivity of simulated mineral dust production to model resolution, *J. Geophys. Res.*, *106*(D16), 18,09918,112.

Liu, M., D. L. Westphal, S. Wang, A. Shimizu, N. Sugimoto, J. Zhou, and Y. Chen (2003), A high-resolution numerical study of the Asian dust storms of April 2001, *J. Geophys. Res.*, *106*(D23), 8653, doi:doi:10.1029/2002JD003178.

Liu, Y., F. Chen, T. Warner, S. Swerdlin, J. Bowers, and S. Halvorson (2004), Improvements to surface flux computations in a non-local-mixing PBL scheme, and refinements to urban processes in the NOAH land-surface model with the NCAR/ATEC real-time FDDA and forecast system, *Extended abstract, 20th Conference on Weather Analysis and Forecasting/16th Conference on Numerical Weather Prediction, 84th Annual AMS Meeting*.

Lu, H., and Y. Shao (2001), Toward quantitative prediction of dust storms: an integrated wind erosion modeling system and its applications, *Environ. Modeling and Software*, *16*, 233–249.

Mahowald, N., and C. Luo (2003), A less dusty future?, *Geophys. Res. Lett.*, *31*(17), doi: 10.1029/2003GL017880.

Mahowald, N. M., G. D. R. Rivera, and C. Luo (2004), Comment on Relative importance of climate and land use in determining present and futire global soil dust emission, *J. Geophys. Res.*, *31*, L24105, doi:10.1029/2004GL021272.

Mahowald, N. M., A. R. Baker, G. Bergametti, N. Brooks, R. A. Duce, T. D. Jickells, N. Kubilay, J. M. Prospero, and I. Tegen (2005), Atmospheric global dust cycle and iron inputs to the ocean, *Global Biogeochem. Cycles*, *19*, GB4025, doi: 10.1029/2004GB002402.

Marticorena, B., and G. Bergametti (1995), Modeling the atmospheric dust cycle: 1. Design of a soil derived dust emission scheme, *J. Geophys. Res.*, *100*(D8), 15,415–16,420.

Marticorena, B., G. Bergametti, B. Aumont, Y. Callot, C. N'Doume, and M. Legrand (1997), Modeling the atmospheric dust cycle: 2. Simulation of Saharan dust sources, *J. Geophys. Res.*, *102*(D4), 4388–4404.

Matheron, G. (1976), A simple substitute for conditional expectation: the disjunctive kriging., *In: Advanced Geostatistics in the Mining Industry, Reidel Publishing Company*, pp. 221–236.

Merrill, J. T., and J. Kim (2004), Meteorological events and transport patterns in ACE-Asia, *J. Geophys. Res.*, *109*, D19S18, doi:10.1029/2003JD004124.

MM5 (2005), MM5 Modeling System Version 3 User's Guide, `http://www.mmm.ucar.edu/mm5`.

MRF (1988), Medium Range Forecast Model Documentation, `http://www.emc.ncep.noaa.gov/gmb/mrf.html`.

Mukai, M., T. Nakajima, and T. Takemura (2004), A study of long-term trends in mineral dust aerosol distributions in Asia using a general circulation model, *J. Geophys. Res.*, *109*, D19204, doi:10.1029/2003JD004270.

Namikas, S., and D. J. Sherman (1997), Predicting aeolian sand transport: revisiting the White model, *Earth Surf. Proc. Landforms*, *22*, 601–604.

Nickling, W. G., and J. A. Gillies (2004), Dust emission and transport in Mali, West Africa, *J. Geophys. Res.*, *108*(D23), 2003JD004374, doi:10.1029.

Okin, G. S., and D. A. Gillette (2004), Modelling wind erosion and dust emission on vegetated surfaces, *In: Spatial Modeling of the Terrestrial Environment, Edited by R.Kelly, N. Drake, S. Barr*.

Orlovsky, N., and L. Orlovsky (2002), White sandstorms in Central Asia, Global alarm: dust and sandstorms from the world's drylands, *UNCCD United Nations, Bangkok, Youlin Y., Squires V., and Qi L. (Eds.)*, pp. 169–196.

Owen, R. P. (1964), Saltation of uniform grains in air, *J. Fluid Mech.*, *29*, 407–432.

Pankine, A. A., and A. P. Ingersol (2002), Interannual variability of Martian global dust storms: Simulations with a low-order model of the general circulation, *Icarus*, *155*(2), 299–323.

Prigent, C., I. Tegen, F. Aires, B. Marticorena, and M. Zribi (2005), Estimation of the aerodynamic roughness length in arid and semi-arid regions over the globe with the ERS scatterometer, *J. Geophys. Res.*, *104*(D3), 3527–3542.

Prospero, J. M., P. Ginoux, O. Torres, S. E. Nicholson, and T. E. Gill (2002), Environmental characterization of global sources of atmospheric soil dust identified with the NIMBUS 7 Total Ozone Mapping Spectrometer (TOMS) absorbing aerosol product, *Reviews of Geophysics*, *40*, 1–31.

Qian, W., L. Qian, and S. Shi (2002), Variations of the dust storm in China and its climatic control, *J. Climate*, *15*, 1216–1228.

Qian, W., X. Tang, and L. Quan (2004), Regional characteristics of dust storms in China, *Atmos. Environ.*, *38*, 4895–4907.

Raupach, M. R., and H. Lu (2004), Representation of land-surface processes in aeolian transport models, *Environ. Mod. Soft.*, *19*, 93–112.

Rife, D. L., T. T. Warner, F. Chen, and E. Astling (2002), Mechanisms for diurnal boundary layer circulations in the Great Basin desert, *Mon. Wea. Rev.*, *130*, 921–939.

Sarre, R. (1988), Evaluation of aeolian sand transport equations in tertidal zone measurements, Staunton sands, England, *Environ. Modeling and Software*, *35*, 671697.

Sassen, K., P. J. DeMott, J. Prospero, and M. Poellot (2003), Saharan dust storms and indirect aerosol effects on clouds: CRYSTAL-FACE results, *Geophys. Res. Lett.*, *30*(12), 1633.

Shao, Y. (2001), *Physics and modelling of wind erosion*, *Series: Atmospheric and Oceanographic Sciences Library*, vol. 23, Kluwer Academic Publisher.

Shao, Y., and J. Wang (2003), A climatology of Northeast Asian dust events, *Meteorogische Zeitschrift*, *12*, 187–196.

Shao, Y., E. Jung, and L. M. Leslie (2002), Numerical prediction of northeast Asian dust storms using an integrated wind erosion modeling system, *J. Geophys. Res.*, *107*(D24), 2001JD001493, doi:10.1029.

Shao, Y., et al. (2003), Northeast Asian dust storms: Real-time numerical prediction and validation, *J. Geophys. Res.*, *108*(D22), 2003JD003667, doi:10.1029.

Singer, A. B., T. Zobeck, L. Poberezsky, and E. Argaman (2003), The PM_{10} and $PM_{2.5}$ dust generation potential of soils/sediments in the Southern Aral Sea Basin, Uzbekistan, *J. Arid Environ,*, *54*, 705–728.

Small, E., F. Giorgi, L. Sloan, and S. Hostetler (2001), The effects of desiccation and climatic change on the hydrology of the Aral Sea, *J. Climate*, *14*(3), 300–322.

Sokolik, I. N. (1999), Nuts and bolts in the radiative forcing by mineral dust, *IGACtivities Newsletter*, *24*(17).

Sokolik, I. N., and O. B. Toon (1996), Direct radiative forcing by anthropogenic mineral aerosols, *Nature*, *381*, 681–683.

Sokolik, I. N., D. M. Winker, G. Bergametti, D. A. Gillette, G. Carmichael, Y. J. Kaufman, L. Gomes, L. Schuetz, and J. E. Penner (2001), Introduction to special section: Outstanding problems in quantifying the radiative impacts of mineral dust, *J. Geophys. Res.*, *106*(D16), 18,01518,028.

Stull, R. (1988), *Introduction to boundary layer meteorology*, Kluwer Academic Publisher.

Sun, J. (2002), Provenance of loess material and formation of loess deposits on the Chinese Loess Plateau, *Earth Planet. Sci. Lett.*, *203*, 845–859.

Sun, J., M. Zhang, and T. Liu (2001), Spatial and temporal characteristics of dust storms in China and its surrounding regions, 1960-1999: Relations to source area and climate, *J. Geophys. Res.*, *106*(D16), 10,325–10,333.

Takemura, T., I. Uno, T. Nakajima, A. Higurashi, and I. Sano (2002), Modeling study of long-range transport of asian dust and anthropogenic aerosols from East Asia, *Geophys. Res. Lett.*

Tegen, I. (2003), Modeling the mineral dust aerosol cycle in the climate system, *Quat. Sci. Rev.*, doi:10.1016/S0277-3791(03)00163-X.

Tegen, I., and I. Fung (1994), Modeling of mineral dust in the atmosphere: Sources, transport, and optical thickness, *J. Geophys. Res.*, *99*(D11), 22,897–22,914.

Tegen, I., and I. Fung (1995), Contribution to the atmospheric mineral aerosol load from land surface modification, *J. Geophys. Res.*, *100*, 18,707–18,726.

Tegen, I., and R. Miller (1998), A general circulation model study on the interannual variability of soil dust aerosol, *J. Geophys. Res.*, *103*(D20), 25, 975–25, 995.

Tegen, I., M. Werner, S. Harrison, and K. Kohfeld (2004), Relative importance of climate and land use in determining present and future global soil dust emission, *Geophys. Res. Lett.*, *31*, L05105, doi:10.1029/2003GL019216.

UNCCD (2001), Global alarm dust and sandstorms from the World's drylands, *Tech. rep.*, Secretariat of the United Nations Convention to Combat Desertification.

Uno, I., H. Amano, S. Emori, K. Kinoshita, I. Matsui, and N. Sugimoto (2001), Trans-Pacific yellow sand transport observed in April 1998: A numerical simulation, *J. Geophys. Res.*, *106*(D16), 18,331–18,334.

Wang, X., Y. Ma, H. Chen, G. Wen, S. Chen, Z. Tao, and Y.-S. Chung (2003), The relation between sandstorms and strong winds in Xinjiang, China, *Wat. Air Soil Poll.*, *3*, 67–79.

Warner, T. (2004), *Desert meteorology*, Cambridge University Press, 620 pp.

Westphal, D. L., O. Toon, and T. Carlson (1988), A case study of mobilization and transport of Saharan dust, *J. Atmos. Sci.*, *45*(15), 2145–2175.

White, B. (1979), Soil transport by winds on Mars, *J. Geophys. Res.*, *84*, 4643–4651.

Xuan, J., and I. N. Sokolik (2002), Characterization of sources and emission rates of mineral dust in northern China, *Atmos. Environ.*, *36*, 4863–4876.

Zender, C., H. Bian, and D. Newman (2003), Mineral dust entrainment and deposition (DEAD) model: Description and 1990s dust climatology, *J. Geophys. Res.*, *108*(D14), 2002JD002775, doi:10.1029.

Zender, C. S., R. Miller, and I. Tegen (2004), Quantifying mineral dust mass budgets: Terminology, constraints, and current estimates, *Eos Trans. AGU*, *85*(48), 509512.

Zhang, D.-L., and R. Anthes (1982), A high resolution of the planetary boundary layer - sensitivity tests and comparisons with SESAME-79 data, *J. Appl. Meteor.*, *21*, 15941609.

Zhang, D.-L., and W.-Z. Zheng (2003), Diurnal cycles of surface winds and temperatures as simulated by five boundary layer parameterizations, *J. Appl. Meteorology*, *43*(1), 157–169.

Zhang, J., Y. Wu, C. Liu, Z. Shen, Z. Yu, and Y. Zhang (2001), Aerosol characters from the desert region of Northeast China and the Yellow Sea in spring and summer: observations at Minqin, Qingdao, and Qianliyan in 1995-1996, *Atmos. Environ.*, *35*, 5007–5018.

Zhang, X. Y., S. L. Gong, T. L. Zhao, R. Arimoto, Y. Q. Wang, and Z. J. Zhou (2003b), Sources of Asian dust and role of clilate change versus desertification in Asian dust emission, *Geophys. Res. Lett.*, *30*(24), 2272, doi:10.1029/2003GL018206.

Zhang, X. Y., et al. (2003a), Characterization of soil dust aerosol in China and its transport and distribution during 2001 ACE-Asia: 1. Network observations, *J. Geophys. Res.*, *108*(D9), 4261, doi:10.1029/2002JD002632.

Zhao, T. L., S. L. Gong, X. Y. Zhang, A. Abdel-Mawgoud, and Y. P. Shao (2006), An assessment of dust emission schemes in modeling east Asian dust storms, *J. Geophys. Res.*, *111*(D05S90), doi:10.1029/2004JD005746.

Zobeck, T., T. Gill, and T. W. Popham (1999), A two-parameter Weibull function to describe airborne dust particle size distributions, *Earth Surf. Process. Landforms*, *24*, 943–955.

VITA

Kremena Darmenova was born in 1975 in Sliven, Bulgaria, where she finished high school specializing in mathematics and natural sciences in 1993. She attended Sofia University, Bulgaria for her Masters degree. Kremena acquired a M.Sc. in Physics in 1998 with two specializations: Atmospheric physics and Astronomy. She was a research fellow with the World Federation of Scientists between 1998-2000, working at the National Institute of Meteorology and Hydrology, Sofia, Bulgaria. She moved to Columbus, Ohio, USA, in 2000, where she worked as an environmental technician at the Great Lakes Environmental Center. In the fall of 2001, Kremena moved to Boulder, Colorado to pursue her Ph.D. in atmospheric sciences at the University of Colorado. She transferred to the Georgia Institute of Technology in 2003 and she acquired Ph.D. in atmospheric sciences in May 2006. Her research interests include atmospheric aerosol physics with a focus on mineral dust, land-atmosphere interactions and regional modeling.